A SEARCH FOR CHARMED MESONS

PRODUCED IN HADRONIC INTERACTIONS

GEORGE E. GINTHER JR.

Submitted in partial fulfillment of the
requirements for the degree of
Doctor of Philosophy

PHYSICS

CARNEGIE-MELLON UNIVERSITY

Pittsburgh, Pennsylvania

11 April 1985

ABSTRACT

A SEARCH FOR CHARMED MESONS PRODUCED IN HADRONIC INTERACTIONS

The hadronic production of charmed states was studied in a two arm spectrometer using a 205 GeV/c negative pion beam incident upon a beryllium target. One arm, filled with dense absorber, triggered the detectors upon the passage of a muon with moderate transverse momentum and total momentum of at least 4 GeV/c. The other arm was an open geometry magnetic spectrometer containing both neutral and charged particle identification capabilities. This document describes the apparatus, the data, and an invariant mass plot search for evidence of charmed particle production through several charged particle decay modes. The $K\pi$, $K\pi\pi\pi$, and $K\pi\pi$ mass plots fail to reveal significant signals. Based upon the $K\pi$ mass plots, the 95 percent confidence upper limit on the $D\bar{D}$ production cross section is found to be less than 48 microbarns per nucleon for the production models tested. A search for evidence of charged D^* production yields 30 ± 16 combinations above background in association with the expected trigger muon charge. Interpreted as a D^* signal, this excess corresponds to a model dependent inclusive $D\bar{D}$ production cross section of $34\pm18^{+14}_{-9}$ microbarns per nucleon.

ACKNOWLEDGMENTS

The planning and execution of high energy physics experiments of the sort described in this thesis requires the co-operation of numerous individuals. I wish to express my thanks to all who contributed to the experiment. I acknowledge the contributions of the Fermilab staff, the members of the E515 collaboration, and their technical staffs.

In particular, I thank my advisor, Dick Edelstein, for his support and guidance throughout this project. I am also particularly grateful for the many contributions of professors Dave Buchholz, Ron Lipton, Jerry Rosen, Randy Ruchti, and Jim Russ. The research associates Mao Huishun, Lorey Dauwe, and Art Kreymer contributed a great deal to the experiment. The efforts of my colleagues, Lucien Cremaldi, Mike McQuade, Rick Pemper, Willis Sakumoto, Steve Sontz, and Lenny Spiegel were most important in making the experiment possible. Thanks also to Steve Delchamps, Pat Mooney, Miguel Sarmiento, and Chris Winter for their assistance during the course of this experiment.

The members of the technical staff at Carnegie-Mellon, Dean Bennett, Fred Johns, and John Smith, made sacrifices for and enormous contributions to this experiment. Thanks also to Richard Bionta, for his patience and assistance early in my graduate student career.

The support, concern, and interest of collaborators, colleagues, friends, and family throughout the course of this experiment is greatly appreciated.

TABLE OF CONTENTS

1 INTRODUCTION 1

1.1 EARLY THEORETICAL EXPECTATIONS 3
1.2 EARLY EXPERIMENTAL RESULTS 12
1.3 EXPERIMENT 515 13
1.4 HADRONIC PRODUCTION OF HEAVY FLAVORS 19
1.5 RECENT EXPERIMENTAL RESULTS 22

2 APPARATUS 34

2.1 BEAM SYSTEM 37
2.2 TRIGGER ARM 44
2.3 TRIGGER LOGIC 50
2.4 FORWARD ARM 55
2.4.1 40D48 Spectrometer Magnet 55
2.4.2 Forward Arm Proportional Wire Chambers 60
2.4.3 Drift Chambers 65
2.4.4 Cherenkov Counter 66
2.4.5 Liquid Argon Calorimeter 69
2.4.6 Forward Arm Muon Identifier 69
2.5 DATA LOGGING AND ON-LINE MONITORING 69

3 EVENT RECONSTRUCTION 75

3.1 PRELIMINARIES 76
3.2 MUON PASS -- TRIGGER ARM TRACKING 81
3.3 HADRON PASS -- FORWARD ARM TRACKING 85
3.3.1 Downstream Forward Arm XZ Segments 85
3.3.2 Forward Arm YZ Segments and XZ YZ Matchups 88
3.3.3 Hadron Pass Output Tapes 94
3.4 DATA SUMMARY TAPES 94
3.4.1 Interaction Vertex Location 95
3.4.2 Trigger Arm Track Refinements 100
3.4.3 Forward Arm Momentum Analysis 101
3.4.4 Forward Arm Particle Identification Analysis .. 103
3.4.5 DST Output Tapes 106

4 SPECTROMETER SIMULATION 108

4.1 SIMULATION METHOD 109
4.1.1 Particle Generators 110
4.1.2 Trigger Arm Particle Propagator 112
4.1.3 Forward Arm Particle Propagator 113
4.1.4 Monte Carlo Output and Analysis 114
4.1.5 Cherenkov Simulation 116
4.2 MONTE CARLO RESULTS 118

5 THE CHARM SEARCH 133

5.1 SCALERS 134
5.1.1 Processing of the Scalers 134
5.1.2 Scaler Sums and Rates 135
5.1.3 Beam Count 141
5.2 DST CUTS 144
5.2.1 Clean Vertex Cut 145
5.2.2 Forward Arm Track Quality Cut 148
5.3 PARTICLE IDENTIFICATION ALGORITHMS 150
5.4 STANDARD STATES 153
5.5 TRIGGER ARM MUON DEFINITION AND CUTS 157
5.6 CHARM SEARCH INVARIANT MASS PLOTS 162
5.6.1 $K\pi$ Invariant Mass Plots 163
5.6.2 $K\pi\pi\pi$ Invariant Mass Plots 169
5.6.3 $K\pi\pi$ Invariant Mass Plots 171
5.6.4 Charged D^* Search 171

6 RESULTS AND CONCLUSIONS 183

6.1 PRODUCTION CROSS SECTION 183
6.1.1 Upper Limits from the $K\pi$ Mass Plots 188
6.1.2 Upper Limits from the $K\pi\pi\pi$ and $K\pi\pi$ Mass Plots . 196
6.1.3 Cross Sections from the Charged D^* Search 196
6.2 SYSTEMATIC UNCERTAINTIES 201
6.3 CHARM CONTENT OF THE PROMPT MUON TRIGGERED EVENTS 207
6.4 CONCLUSIONS 211
6.5 PROSPECTS 215

REFERENCES 217

LIST OF TABLES

1. Trigger arm detector element positions and dimensions 46
2. Beam system and forward arm detector elements 61
3. Trigger arm acceptance for muons from $D \to K\mu\nu$ 122
4. Trigger arm acceptance for muons from $D \to K^*(890)\mu\nu$ 123
5. Forward arm acceptance for $D \to K\pi$ 126
6. Forward arm acceptance for $D \to K\pi\pi\pi$ and $D \to K\pi\pi$ 127
7. Forward arm acceptance for charged $D^* \to D\pi$ 129
8. Scaler sums and rates 140
9. Constants employed in the cross section calculations 189
10. $D\bar{D}$ production cross section upper limits from $K\pi$ 192
11. $D\bar{D}$ production cross section upper limits from $K\pi$ 193
12. $D\bar{D}$ production cross section upper limits from $K\pi$ 195
13. $D\bar{D}$ production cross section upper limits from $K\pi\pi\pi$ 197
14. $D\bar{D}$ production cross section upper limits from $K\pi\pi$ 198
15. $D\bar{D}$ production cross section from charged D^* search 200
16. Systematic uncertainties 202
17. Event countdown 208
18. Summary of experiments on production of charm by protons 212
19. Summary of experiments on production of charm by pions 213

LIST OF FIGURES

1. SU(4) elementary particle multiplets 6
2. Charm decay mechanisms 9
3. QCD processes for hadronic production of charm 21
4. Spectrometer overview 35
5. Beam system in target vicinity 40
6. Target and upstream absorber 42
7. Trigger arm active elements 45
8. M1 hodoscope 47
9. Logic diagram for M1 signal 52
10. M2 M3 road 53
11. Trigger logic diagram 56
12. Overview of the forward arm 57
13. 40D48 magnetic field 59
14. Cherenkov counter 68
15. Forward arm muon identifier 70
16. Beam and trigger arm PWC efficiency 79
17. Forward arm chamber efficiency 80
18. Track bending in the YZ view 89
19. Beam optics correlation 96
20. Cherenkov counter efficiency 117
21. Track finding program efficiency 120
22. Trigger arm muon acceptance 121
23. Forward arm $D \rightarrow K\pi$ acceptance 125

24. Forward arm $D^{*}\rightarrow D\pi$ acceptance 128
25. Forward arm mass resolution for $D\rightarrow K\pi$ 131
26. Forward arm mass resolution for charged D^{*} 132
27. Average BEAM per spill 136
28. Beam related scaler ratios 137
29. Trigger arm scaler ratios 138
30. Livetime fraction 142
31. Interaction vertex distributions 146
32. Forward arm track distributions 149
33. $K^{+}K^{-}$ invariant mass plots 154
34. $K^{+}\pi^{-}$ and $K^{-}\pi^{+}$ invariant mass plots 156
35. Trigger arm muon distributions 159
36. Reconstructed triggering muons per BEAM 161
37. Right-sign $K\pi$ mass plots with CONCER identification 164
38. Right-sign $K\pi$ mass plots with $\cos(\theta_{CM})$ cut 166
39. Right-sign $K\pi$ mass plots with CER identification 167
40. Wrong-sign $K\pi$ mass plots with CER identification 168
41. Right-sign $K\pi\pi\pi$ mass plots with CER identification 170
42. Wrong-sign $K\pi\pi\pi$ mass plots with CER identification 172
43. Right-sign $K\pi\pi$ mass plots with CER identification 173
44. Wrong-sign $K\pi\pi$ mass plots with CER identification 174
45. Charged D^{*} search 177
46. Wrong-sign "D^{*}" plots 178
47. Right-sign $K\pi\pi$ $K\pi$ mass difference plots 180
48. Right-sign $K\pi$ mass plots with mass difference cut 181

CHAPTER 1

INTRODUCTION

This thesis describes a high energy particle physics experiment which was designed to search for and study the production via hadronic collisions and subsequent decay of particles that have the distinguishing property referred to as charm. It is hoped that information derived from such studies might contribute to an improved understanding of the fundamental interactions of nature.

The experiment, which is designated E515, was performed at the Fermi National Accelerator Laboratory (Fermilab) by researchers from Carnegie-Mellon University, Fermilab, Northwestern University, and the University of Notre Dame. The strategy employed in the design and execution of the experiment was influenced by the available experimental evidence together with theoretical expectations. Therefore, this chapter provides a brief review of the environment in

which the experiment was proposed and performed. The first section of this chapter describes the theoretical anticipation of charm and the properties and signatures expected to indicate its detection. The second section discusses the information gathered about charm by the early experiments. The third section describes the basic strategy adopted for this particular experimental search. Some theoretical models for the production mechanisms of charm in hadronic interactions are described in the fourth section. The final section of this chapter summarizes several recent experimental results on charmed particles.

The remainder of the document describes E515 in general, as well as a particular analysis of the accumulated data. Chapter 2 describes the apparatus employed in this experiment. Chapter 3 discusses the filtering and reduction of the raw data into kinematic quantities of interest. Chapter 4 presents a brief discussion of the simulation of the apparatus. This simulation was necessary to evaluate the sensitivity of the experiment to charm production. Chapter 5 describes the search for evidence of charmed particle production through the construction of invariant mass plots. Chapter 6 presents the results of the charm search in terms of model dependent production cross sections.

1.1 EARLY THEORETICAL EXPECTATIONS

The properties of the strong interactions among the hadrons and the spectroscopy of the observed hadrons suggested an underlying SU(3) symmetry. The quark model [1] employed a triplet of fermions referred to as quarks as the fundamental representation of that symmetry. The triplet is composed of an isospin doublet of quarks called the up (u) and down (d) quark, and an isospin singlet called the strange (s) quark. The quarks are all assigned spin 1/2, and baryon number 1/3. The designations u, d, and s are said to be the flavors of the quarks. The d and s quarks are assigned an electric charge of -1/3 in units of the magnitude of the electron's charge, and the u quark has an electric charge of +2/3. The isospin doublet has zero strangeness while the strange quark has minus one unit of strangeness. The anti-triplet of entities which have additive quantum numbers opposite to the quarks, are referred to as antiquarks. Baryons are viewed as combinations of three valence quarks, while mesons are constructed from valence quark antiquark pairs. Within the quark model, the strong interaction between quarks is mediated by electrically neutral vector fields whose interactions are indifferent to the quark flavor. The electromagnetic and weak interactions are described in terms of current-current interactions. The hadronic part of the electromagnetic current is given by the expression

$$j^{\alpha}_{em} = \tfrac{2}{3}\overline{\Psi}_u\gamma^{\alpha}\Psi_u - \tfrac{1}{3}\overline{\Psi}_d\gamma^{\alpha}\Psi_d - \tfrac{1}{3}\overline{\Psi}_s\gamma^{\alpha}\Psi_s$$

where γ^{α} are the Dirac gamma matrices and $\overline{\Psi}_i$ are the Dirac conjugate

fields to the fields Ψ_i for quarks with flavor i. This expression for the electromagnetic current conserves flavor. The corresponding part of the weak charged current, which does not conserve flavor, is expressed as

$$j^{\alpha}_{w\pm} = \overline{\Psi}_u \gamma^{\alpha}(1-\gamma_5)[\ \Psi_d \cos(\theta_C) + \Psi_s \sin(\theta_C)\ ]$$

where θ_C is the Cabibbo angle [2]. The Cabibbo angle relates the eigenstates of the weak interactions between quarks to the mass eigenstates. A recent determination of θ_C yielded the value $\sin(\theta_C)=0.231\pm0.003$ [3].

The three quark model was successful in classifying the observed particle states in terms of their valence quark content. However, the three quark model resulted in an asymmetry between the leptons and the quarks. There were four known leptons, the electron (e), the muon (μ), and their respective distinguishable neutrinos (ν_e and ν_μ), and only three quarks. During 1964, Bjorken and Glashow investigated a quark model that asserts a more obvious lepton-quark symmetry by introducing a fourth fundamental field which they called charm, and assuming that the four quarks were the fundamental representation of the SU(4) symmetry group [4]. As with strangeness, the new additive quantum number associated with the charm quark (called charm), is conserved in the strong and electromagnetic interactions. The introduction of the charm quark (now assigned electric charge +2/3, baryon number 1/3, zero strangeness, and one unit of charm) resulted in the prediction of numerous additional entries to the particle spectrum. The predicted members of the pseudoscalar meson SU(4)

multiplet which encompasses the standard SU(3) pseudoscalar multiplet are shown in figure 1(a) together with their valence quark content. The members of the spin 1/2 baryon multiplet are shown in figure 1(b). Some decay modes and selection rules for the predicted "charmed particles" (particles with a nonzero charm quantum number) were also discussed when the model was proposed.

During 1967, a unified model of the weak and electromagnetic interactions among leptons was proposed which employed the principle of local gauge invariance in the SU(2)×U(1) gauge group to determine the mediators of the interactions [5]. The mediator of the electromagnetic interaction is the massless photon. The weak interaction is mediated by three massive vector bosons, called the W^+, W^-, and the Z^0. The theory thus predicts the existence of an electrically neutral weak current. (With the extensions of this model to include the quarks, the model has gained wide acceptance, and is now referred to as the Standard Model of the electro-weak interactions.)

During 1970, Glashow, Iliopoulos, and Maiani (GIM) observed that the charm quark provided advantages beyond achieving a "suggestive lepton-quark symmetry" [6]. The charm quark and its associated weak hadronic current were useful in solving problems in higher order weak interactions by cancelling undesired terms in the weak interaction expansions. Furthermore, GIM pointed out that if the weak neutral currents did indeed exist, the four quark model they proposed contained only flavor conserving weak neutral currents whereas the

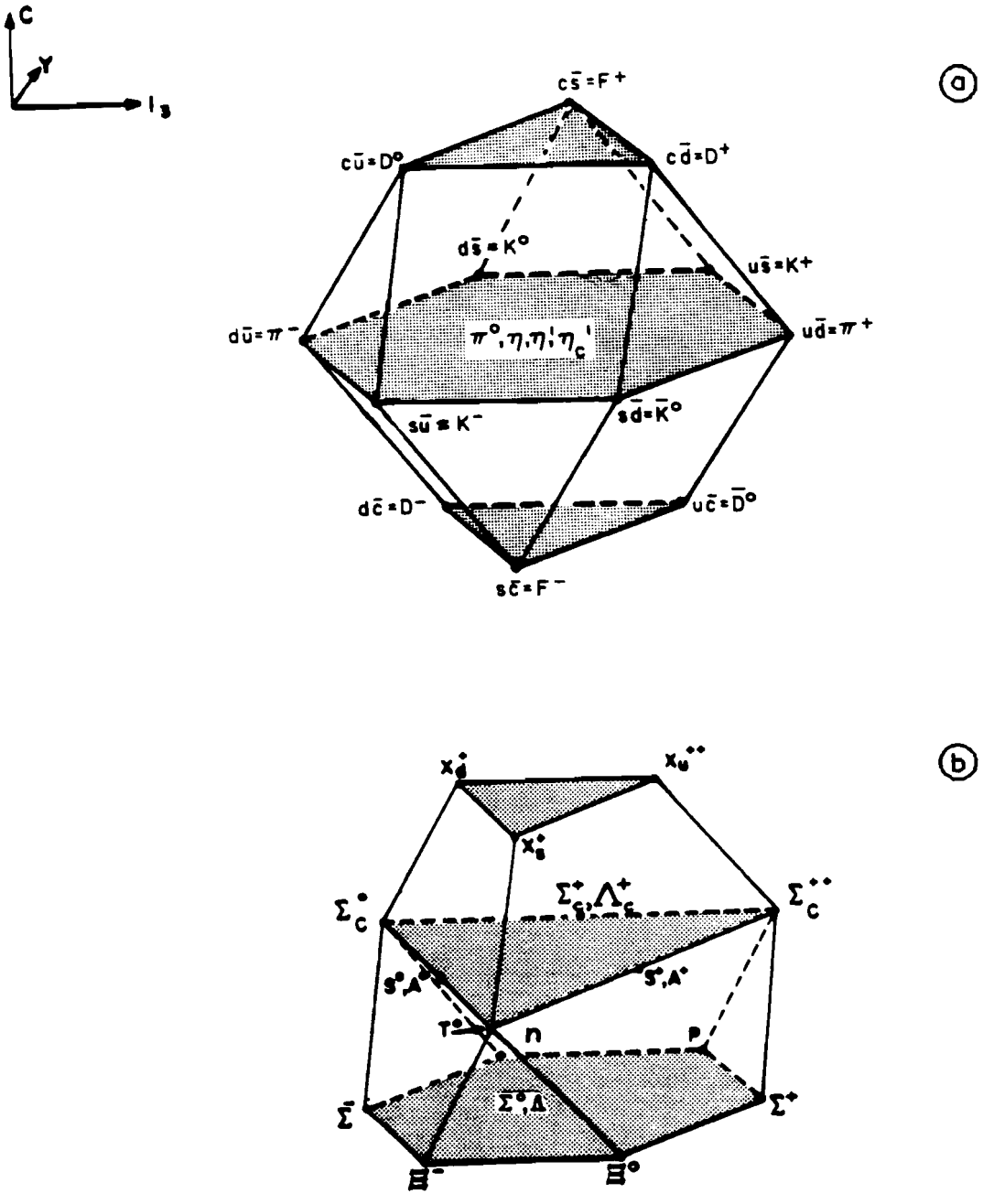

FIGURE 1. SU(4) weight diagram of some elementary particles. (a) The pseudoscalar meson multiplet and the corresponding valence quark content. (b) The spin 1/2 baryon multiplet.

three quark model allowed strangeness changing neutral currents, which were known to be suppressed. The GIM model relegated strangeness changing weak neutral currents to higher order interactions. Additionally, in order for the size of the higher order corrections to be consistent with experiment, the proposed charm quark mass was expected to be no larger than 3 or 4 GeV/c^2. (It should be noted that evidence of weak neutral currents was indeed observed in neutrino interactions during 1973 [7].)

With the introduction of the charm quark, the charged weak hadronic current is expressed as

$$j^{\alpha}_{w\pm} = \overline{\Psi}_u \gamma^{\alpha}(1-\gamma_5)[\ \Psi_d \cos(\theta_C) + \Psi_s \sin(\theta_C)\ ] + \overline{\Psi}_c \gamma^{\alpha}(1-\gamma_5)[\ \Psi_s \cos(\theta_C) - \Psi_d \sin(\theta_C)\ ].$$

The corresponding neutral weak current is

$$j^{\alpha}_{w0} = \overline{\Psi}_u \gamma^{\alpha}(1-\gamma_5)\Psi_u - \overline{\Psi}_d \gamma^{\alpha}(1-\gamma_5)\Psi_d + \overline{\Psi}_c \gamma^{\alpha}(1-\gamma_5)\Psi_c - \overline{\Psi}_s \gamma^{\alpha}(1-\gamma_5)\Psi_s.$$

Since charm is by hypothesis a conserved quantum number in both the strong and electromagnetic interactions, the lowest mass charmed particles can only decay weakly. The lowest mass charmed particles were expected to be the pseudoscalar charmed mesons, called the D mesons. Since the GIM weak neutral current is flavor conserving, only the weak charged current can participate in the decay of charm quarks. The form of the charged weak current implies that the charm quark should decay preferentially into a strange quark. Thus the decay products of charmed particles should frequently contain strangeness.

Several possible decay mechanisms for the D mesons are illustrated in figure 2(a). Estimates of the rates for the leptonic decays corresponding to the annihilation diagram yield results which are a few orders of magnitude below the estimated semileptonic decay rates due to helicity suppression [8]. Thus leptonic decays of charmed particles are expected to be negligible.

The naive spectator model of charmed particle decay assumes that the interactions between the valence charm quark and other constituents in the hadron can be neglected during the weak charm quark decay. Thus, in this model the lifetimes of all weakly decaying charmed particles are equal because they depend only upon the charm quark decay rate. Schematic illustrations of the decay modes of the charm quark along with their relative decay rates are given in figure 2(b). The factor of three in the relative decay rates for the non-leptonic modes arises from a sum over an additional hidden degree of freedom assigned to the quarks, referred to as color. (Color was originally proposed to relieve conflicts between the quark model and the Pauli exclusion principle. Color has since been hypothesized to be the charge of the strong interaction theory known as Quantum Chromodynamics or QCD [9].) The semileptonic decay of the charmed quark proceeds through the processes $c \rightarrow s\ \ell^+\ \nu_\ell$ and $c \rightarrow d\ \ell^+\ \nu_\ell$. The rate for these processes is calculated in the same manner as the rate for muon decay ($\mu^+ \rightarrow e^+\ \nu_e\ \bar{\nu}_\mu$) [10], and yields

$$\Gamma_{SL} = \Gamma(c \rightarrow e^+\ \nu_e\ X) = G_F^2\ m_c^5\ /\ (192\ \pi^3) \approx 10^{-11}\ \text{sec}^{-1}$$

where G_F is the weak coupling constant and $m_c \approx 1.5\ \text{GeV}/c^2$ is the mass

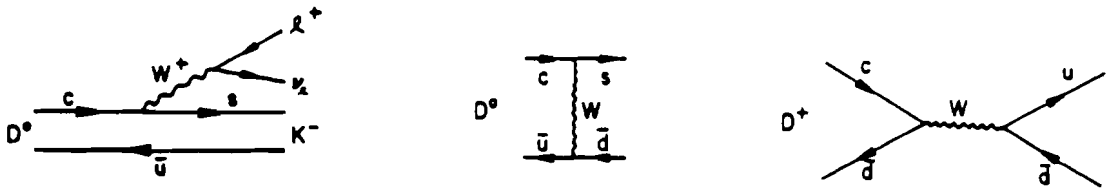

spectator exchange annihilation

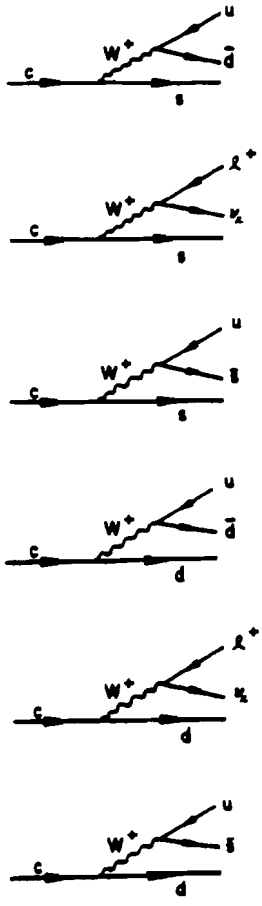

$3\,\Gamma_{SL}\cos^4\theta_C$

$\Gamma_{SL}\cos^2\theta_C$

$3\,\Gamma_{SL}\cos^2\theta_C\sin^2\theta_C$

$3\,\Gamma_{SL}\cos^2\theta_C\sin^2\theta_C$

$\Gamma_{SL}\sin^2\theta_C$

$3\,\Gamma_{SL}\sin^4\theta_C$

FIGURE 2. (a) D meson decay mechanisms. (b) Spectator model decay modes of the charm quark together with relative decay rates (neglecting light quark masses and phase space considerations).

of the charm quark. The semileptonic branching ratio for charmed particles predicted by this naive spectator model is then

$$BR(c \rightarrow e^+ \nu_e X) = BR(c \rightarrow \mu^+ \nu_e X) = \Gamma_{SL} / \Gamma_{TOT} = 0.20$$

where Γ_{TOT} is the sum of all the partial widths shown in figure 2(b) including both the semielectronic and semimuonic modes. The lifetime of weakly decaying charmed particles is

$$\tau = 1 / \Gamma_{TOT} = 0.20/\Gamma_{SL} \approx 8 \times 10^{-13} \text{ sec}$$

in this spectator model. (This model ignores the anticipated non-leptonic enhancements which were expected to increase the non-leptonic decay rates by a factor of five or more [8,11].) This comparatively short weak decay lifetime together with the large anticipated branching ratio of charm into leptons implied that the decay of charmed particles could be an important source of "prompt leptons." Prompt leptons are leptons that arise from sources other than the weak decay of hadrons which have lifetimes greater than 10^{-10} sec. Due to the relatively high mass anticipated for the charmed particles, there were expected to be many individual hadronic decay modes, each with a relatively small branching ratio.

Just as the K^0 and the $\overline{K}^0$ mix, the D^0 and $\overline{D}^0$ should also mix. However, the mixing of the $D^0\overline{D}^0$ system was anticipated to be quite small [12].

The production of charmed particles by incident neutrinos proceeds via the Cabibbo suppressed fundamental process, $\nu_\ell \, d \rightarrow \ell^- \, c$, or via the Cabibbo allowed process, $\nu_\ell \, s \rightarrow \ell^- \, c$, which requires an interaction with a strange quark in the target. Although the target

nucleons in such experiments have no strange valence quarks, hadrons are viewed as consisting of a combination of valence quarks as well as a sea of quark and antiquark pairs and gluons. (The gluons are the mediators of the strong force in QCD.) Above the threshold for charm production, about $\tan^2(\theta_C) \approx 0.056$ of the neutrino interactions were expected to contain charm, if the strange sea is negligible. If the contribution of the strange sea is not negligible, a larger fraction of the neutrino induced interactions should contain charm. Thus a relatively large fraction of all neutrino induced interactions was expected to yield charmed particles, however, the total cross section for neutrino interactions is quite small, making neutrino production a difficult way to study charmed particles. Note that the neutrino induced production of charmed particles followed by their semileptonic decay should result in events with a pair of opposite sign leptons in the final state, which provides a signature for observing neutrino induced production of charm.

The production of charm in electron positron (e^-e^+) annihilation proceeds through the coupling of the virtual photon to a charm anticharm quark pair. Well above the threshold for charm production, this process should yield charmed particles in a large fraction (about 40 percent) of the e^+e^- annihilations because the coupling strength of the virtual photon to the quark antiquark pair depends only upon the electric charge of the quark.

Possible signatures of the production of charmed particles in hadronic interactions include the detection of short lived particles, or the detection of a new source of prompt leptons, but the level of that production was theoretically uncertain.

Many of the anticipated properties of the charmed particles, as well as remarks on expectations for charm production, were presented in the work of Gaillard, Lee, and Rosner [8].

1.2 EARLY EXPERIMENTAL RESULTS

During 1971, an emulsion chamber exposed to cosmic rays detected an interaction which produced a pair of short lived particles, one of which had a mass around 2 GeV/c^2 [13]. In 1974, an upper limit of less than 500 μb was reported for the hadronic production cross section of charmed particles in 400 GeV/c proton proton interactions [14]. This upper limit was based upon a search for evidence of short lived tracks in bubble chamber pictures, and assumed a charm lifetime greater than 4×10^{-13} sec, a mass of less than 2 GeV/c^2 and an average momentum of greater than 160 GeV/c.

The discovery of an extremely narrow neutral resonance at 3.1 GeV/c^2 produced in both proton beryllium interactions [15] and e^+e^- annihilations [16] was announced in the fall of 1974. This particle, named the J/ψ, was interpreted in a wide variety of ways, including the assertion that the J/ψ is a vector meson that carries hidden charm (a charm-anticharm state) [17].

A neutrino induced bubble chamber event reported in 1975 was interpreted as the production and decay of a charmed baryon as follows:

$$\nu_\mu \; p \rightarrow \mu^- \; \Sigma_c^{++}$$
$$\hookrightarrow \Lambda_c^+ \; \pi^+$$
$$\hookrightarrow \Lambda \; \pi^+ \; \pi^+ \; \pi^-$$

because the event violated the selection rules expected to hold in the three quark model [18]. In 1976, the production of a narrow state at 1.865 GeV/c^2 in e^+e^- annihilations was observed through its decay into a charged kaon and one or three charged pions [19]. This narrow state was interpreted as the neutral D meson. The charged D meson was also observed in e^+e^- annihilations through its decay into a charged kaon and two same sign charged pions [20]. Meanwhile, numerous experiments searching for direct evidence of hadronic production of charmed particles were reporting upper limits for the hadronic production cross section [21].

1.3 EXPERIMENT 515

The experiment described in this thesis was proposed in 1976. Its purpose was to search for the hadronic production of charmed particles. If the level of such production was found to be large enough, it was hoped to measure the characteristics of the production and the decay of various charmed particles. Since it was already

suspected that the fraction of hadronic interactions containing charm was relatively low at the energies available from accelerators, some filtering was expected to be necessary in order to observe charmed particles. The information gathered by our detector was recorded only for those interactions which satisfied certain requirements referred to as the "trigger." Those requirements were based upon the expected characteristics of charm. A well chosen trigger could aid considerably in the detection of difficult-to-observe states by enhancing the fraction of recorded interactions which contain a signal of interest.

Charmed particles were expected to be produced in interactions between incident hadrons from the accelerator and the nucleons in the target. Our plan was to trigger on the observation of a prompt muon arising from the decay of a charmed (anticharmed) particle and then observe the decay products of the anticharmed (charmed) particle associated with it. The advantage of a prompt lepton trigger is that leptons are produced relatively infrequently in hadronic interactions, thus allowing the selection of interactions which are more likely to contain charm. Muons were selected rather than electrons because of the relative ease of identification of muons and to avoid the problem of electrons arising from conversion of photons from π^0 decays. Other sources of muons which could trigger the detector included the weak decays of relatively long lived hadrons (such as pions and kaons), the electromagnetic decays of vector mesons, and the continuum of muon pairs [22].

There are, of course, disadvantages associated with the prompt muon trigger. If the semileptonic branching ratio of charm turns out to be smaller than anticipated, the signal to background selected by our trigger is correspondingly smaller than anticipated. Additionally, any results on the production characteristics of charm are biased by the trigger requirements, and the measurements of production rates are dependent upon the dynamics of the charm anticharm production correlations.

The detector constructed to perform this experiment was a two arm spectrometer instrumented with devices to record the location of passage of charged particles so as to measure the signs of the charges and the momenta of those particles. Some charged and neutral particle identification capabilities were also included in the spectrometer.

The trigger arm of the spectrometer was intended to detect the prompt muons. Since muons are the only known long lived deeply penetrating charged particles, the trigger arm contained a large amount of material, referred to as "absorber," to distinguish muons from other charged particles incident upon the trigger arm. To minimize the number of muons from non-prompt sources, the absorber was placed as close as feasible to the interaction location, providing the maximum opportunity for the produced hadrons headed towards the trigger arm to interact before undergoing weak decays. The trigger arm acceptance favored centrally produced charmed states ($x_F \approx 0$) and muons with moderate transverse momentum. (Feynman x or x_F is the ratio of the longitudinal momentum to the maximum available

longitudinal momentum in the center of momentum frame [23].) The accepted muons needed momenta of at least 4 GeV/c in order to pass through the entire absorber and satisfy the trigger requirements.

The forward arm was an open geometry large acceptance spectrometer intended to detect the decay products of the associatively produced partner of the triggering charmed (anticharmed) particle. The forward arm acceptance favored particles which were produced forward in the center of momentum frame of the interaction ($x_F>0$).

Evidence for the hadronic production of charm in our prompt muon triggered data could manifest itself in a variety of ways. This thesis describes an invariant mass plot search for evidence of charmed meson decays into charged particles. The invariant mass of any pair of particles with momentum $\vec{p}_1$ and $\vec{p}_2$, and corresponding energies E_1 and E_2, is given by the expression

$$m = \sqrt{[\ (E_1 + E_2)^2 - (\vec{p}_1 + \vec{p}_2)^2\ ]} = \sqrt{[\ m_1^2 + m_2^2 + 2(E_1E_2 - \vec{p}_1\cdot\vec{p}_2)\ ]}$$

where m_1 and m_2 are the corresponding rest masses of the particles. If a parent state decays into a pair of particles, then the invariant mass of that pair will be the mass of that parent state. This result can be employed to search for evidence of the production and subsequent decay of short lived states such as charmed particles. The invariant mass of all combinations of particles detected in the forward arm that satisfy the constraints upon particle charge and identity can be calculated and entered into an invariant mass plot. Any combination arising from the decay of an individual parent state

will contribute to a specific region of the mass plot around the parent mass (but smeared by the finite resolution of the spectrometer). Particle combinations that do not arise from an individual parent will have masses which are distributed throughout the mass plot within the kinematically accessible range. These combinations form a background which may obscure a signal from the decay of a parent state. If the signal is large enough, it may be observed above the background. In interactions which produce many particles, the number of background combinations can be quite large, and it becomes increasingly difficult to isolate any small signal.

Any property that can be employed to suppress the background relative to the signal will provide an enhanced opportunity to observe the signal. Assuming that $D^0\overline{D}^0$ mixing is negligible, the conservation of charm in strong interactions together with the properties of the charged weak current, which governs the decay of charm, provides a useful technique for reducing the backgrounds in our data. If the trigger muon arises from the weak decay of a charm (anticharm) quark, then the muon will have a positive (negative) charge. Furthermore, the associatively produced partner state must contain an anticharm (charm) quark. So, if the partner state that is being sought in the forward arm is a charged meson, then that meson must have negative (positive) charge, (or else it must be exotic). This correlation between the trigger muon sign and the sign of the associated charged charmed meson allows the particle combinations to be divided between two mass plots, the "right-sign" and "wrong-sign" mass plots. The

invariant mass from a given particle combination is only entered into the right-sign mass plot if the sign correlation between that combination and the trigger muon satisfies the conditions required by the charm hypothesis, whereas the wrong-sign plot contains only entries which violate that correlation. Additionally, since the Cabibbo favored decays of anticharm (charm) quarks result in antistrange (strange) quarks, if the decay mode of the charmed meson under study contains only one meson with nonzero strangeness and that meson is charged, then the charge of the strange meson must be the same as the charge of the trigger muon. This observation allows the construction of right-sign and wrong-sign mass plots for some neutral charmed meson decay modes. Besides reducing the backgrounds by separating particle combinations into two mass plots, the right-sign and wrong-sign mass plots provide a natural test for the hypothesis that charm is the origin of an observed signal, since such a signal should only be observed in the right-sign plots.

This document presents the results of a search for evidence of the decays $D^0 \rightarrow K^- \pi^+$, $D^0 \rightarrow K^- \pi^+ \pi^- \pi^+$, $D^+ \rightarrow K^- \pi^+ \pi^+$, and $D^{*+} \rightarrow D^0 \pi^+$ (and their antiparticles) in the prompt muon triggered data gathered during the spring of 1981 by the E515 spectrometer.

1.4 HADRONIC PRODUCTION OF HEAVY FLAVORS

A promising theory of the strong interactions known as Quantum Chromodynamics (QCD) has been emerging, and the hadronic production of charm may provide a test of the theory's capability. In QCD, quarks are assumed to have a hidden internal degree of freedom called color, which has three values. The strong interactions among the quarks can be made invariant under the local SU(3) color gauge transformations by introducing eight massless vector bosons, called gluons, which mediate the interaction. The strength of the interaction is assumed to be such that no colored object can become free, so hadrons are assumed to be color singlets. As hadrons are probed with increasing momentum transfer, the strength of the coupling between the constituent partons (quarks and gluons) diminishes. This phenomenon is called asymptotic freedom. The application of QCD to specific problems is frequently hindered by the strength of the interaction at small momentum transfers, which makes the use of perturbation theory hazardous. However, due to asymptotic freedom it is expected that perturbation theory can be fruitfully applied to processes involving large masses, such as the production of charm quarks. Using perturbative QCD and elements of the parton model, calculations of the contributions of various subprocesses to the hadronic production of charm quarks have been made [24]. (Color singlet charmed hadrons are assumed to emerge via final state interactions.)

The lowest order flavor creation subprocesses are illustrated in figure 3(a). The relative importance of the quark antiquark fusion contribution is expected to decrease with increasing interaction energy. Any contribution from this subprocess should be dependent upon the valence quark content of the incident particles. As the energy of the interaction increases, the gluon fusion subprocess contributions are expected to increase. Gluon fusion should be independent of the flavor of the valence constituents of the incident particles. Due to the gluon distribution in hadrons, gluon fusion subprocesses yield central production of charm, that is, the produced charmed particles should favor x_F values around zero.

In flavor excitation subprocesses, a charm quark is knocked out of the sea by a hard collision with a gluon or a light quark. The lowest order flavor excitation subprocesses, depicted in figure 3(b), were originally discounted because it was assumed that the charm sea was negligible. Experimental observations at the ISR [25] implied that the charm production cross section was much larger than predicted by the flavor creation subprocesses. Furthermore, there was a significant contribution to the cross section at large x_F, corresponding to the production of leading or forward charmed particles. These results prompted a re-evaluation of the possible contribution of the flavor excitation subprocesses. Leading charmed particle production is thought to arise via recombination of the produced charm quark with the valence quarks of the incident hadrons.

quark antiquark fusion

(a)

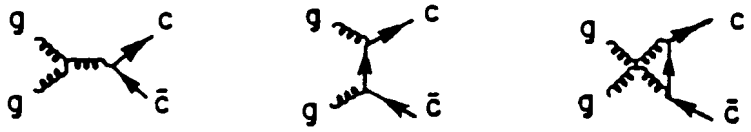

gluon fusion

(b)

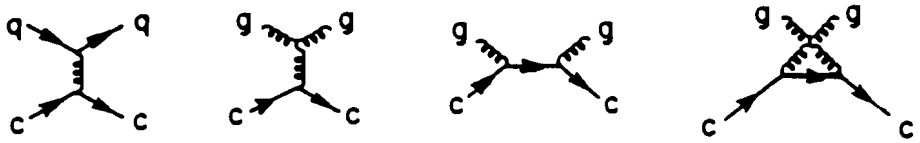

charm excitation

FIGURE 3. Lowest order QCD subprocesses for the hadronic production of charm. (a) Flavor creation subprocesses (quark antiquark fusion and gluon fusion). (b) Charm excitation subprocesses.

1.5 RECENT EXPERIMENTAL RESULTS

A wide variety of production and detection techniques have been employed to study the properties of charm. Many of the observed properties of charmed particles are summarized in a review by Trilling [26].

Much of the available information on D mesons comes from e^+e^- colliders, which have the advantage of large charm signals relative to background. Many decay modes of both the charged and neutral D mesons have now been observed, including Cabibbo suppressed decay modes. The branching ratios for individual decay modes are generally small. The inclusive branching ratio for a charged D meson to decay into a final state that includes an electron is $0.170\pm0.019\pm0.007$, while the inclusive branching ratio for the neutral D meson to decay into a final state that includes an electron is only $0.075\pm0.011\pm0.004$ [27]. Although the inclusive branching ratios for D mesons decaying into muons have not been measured separately for charged and neutral D mesons, the inclusive branching ratio into a state including a muon averaged over a sample of charged and neutral D mesons is found to be comparable to the inclusive electronic branching ratio averaged in a similar manner [28]. Studies of the momentum spectrum of electrons from D meson decays indicate that the spectrum is incompatible with an individual decay mode of $D\rightarrow\pi e\nu$, $D\rightarrow Ke\nu$, or $D\rightarrow K^*(890)e\nu$ [29]. However, the electron momentum spectrum can be adequately fit to a hypothesis of a mixture of these sources, yielding 37 ± 16 percent from the

$K^*(890)e\nu$ mode, and 55±14 percent from the $Ke\nu$ mode. Similar fitting procedures place a 90 percent confidence upper limit on the branching ratio of the purely leptonic decay of the charged D meson, $D\to\mu\nu$, of less than 0.014 [30].

The charged and neutral charmed vector mesons, called the D^* mesons, have been observed. As theoretically anticipated, the mass difference between the D^* and the D mesons is small, so that the electromagnetic decay mode $D^*\to D\gamma$ competes with the strong decay mode $D^*\to D\pi$, and the D^* has a narrow width.

Upper limits on $D^0\overline{D}^0$ mixing have been determined in several experiments including a hadronic production experiment, which quotes a 90 percent confidence upper limit of 4.4 percent for D mesons decaying into wrong-sign muons [31]. A model independent 90 percent confidence upper limit on $D^0\overline{D}^0$ mixing of 8.1 percent was determined from a study of charged D^* decays [32].

The experimental status of the charmed strange meson, the F, is somewhat confused [33]. Evidence for a narrow state of mass 2.03 GeV/c^2 that decayed into an η and a charged pion was observed and interpreted as the F meson [34]. Several other decay modes have since been reported, with F masses around 2.02 GeV/c^2. More recent experiments have observed evidence for the F meson at 1.97 GeV/c^2 through its decay into a phi and a charged pion [35]. The electromagnetic decay $F^*\to F\gamma$, which was expected to be the F^* meson's dominant decay mode, has been observed [34,35].

Evidence for charmed baryon production comes primarily from photoproduction, neutrino production, and hadronic production experiments. A narrow state whose mass has been reported at values between 2.25 and 2.28 GeV/c^2 has been observed in several decay modes, and is interpreted as the Λ_c^+. The inclusive electronic branching ratio of this lowest mass charmed baryon state is 0.045±0.017 as determined in an e^+e^- experiment [36]. A few interactions interpreted as including Σ_c^{++} and $\bar{\Sigma}_c^0$ decays have been reported [37]. One hyperon beam experiment detected a narrow state in a $\Lambda K^-\pi^+\pi^+$ mass plot, and interpreted it as a decay mode of the charmed strange baryon, the A^+ [38]. The same experiment failed to observe the A^0, which is the neutral partner to the A^+ [39].

Most measurements of the lifetimes of charmed particles come from fixed target experiments which employed either emulsions, high resolution bubble chambers, or silicon strip detectors to observe the decay vertices [40]. A recent survey of charmed particle lifetime measurements yielded the following results [33]:

$$\tau(D^+) = 9.3^{+1.3}_{-1.0} \times 10^{-13} \text{ sec}$$

$$\tau(D^0) = 4.0^{+0.4}_{-0.3} \times 10^{-13} \text{ sec}$$

$$\tau(\Lambda_c^+) = 2.2^{+0.8}_{-0.5} \times 10^{-13} \text{ sec}$$

$$\tau(F) = 2 \times 10^{-13} \text{ sec}$$

The charged D lifetime is a factor of 2.3±0.3 larger than the neutral D lifetime. This result is consistent with the ratio of the semileptonic branching ratios of the D mesons, and implies that the naive spectator model is not the entire explanation of charm decay.

The additional decay processes illustrated in the annihilation and exchange diagrams provide possible explanations for the lifetime differences [41].

Although many details remain to be explored, there is substantial overlap between the theoretically anticipated and the experimentally observed properties of charmed particles.

Due to the variety of incident energies, triggers, experimental techniques, target materials, and detector acceptances employed in hadronic production experiments, comparison of results from different experiments is complicated by the assumptions necessary to interpret the gathered data. The techniques employed in the study of the hadronic production of charm are of three basic types: prompt lepton studies, bump hunting, and vertex detection. Recent reviews of the experimental techniques employed, and the reported results are available [33,42]. A few of the results of selected experiments are summarized below (and also in tables 18 and 19 of chapter 6).

Many of the prompt lepton studies were experiments that searched for evidence of prompt leptons by determining the number of leptons detected as a function of the density of the target, and then extrapolating to a target of infinite density. The results on charm production from such experiments are rather indirect. The FMOW collaboration performed an experiment at Fermilab, called E613, which dumped a 400 GeV/c proton beam into two different density tungsten targets, and measured the resulting prompt neutrino fluxes. They

reported a total $D\bar{D}$ production cross section of 27±4±5 μb per nucleon based upon the detected prompt muon neutrino flux and assuming linear mass number dependence [43]. In contrast to earlier prompt neutrino experiments which had smaller acceptances, E613 observed the prompt electron neutrino production rate to be approximately equal to the prompt muon neutrino production rate [44]. E613 also performed a prompt lepton study using beryllium targets. A comparison of the results from the tungsten targets and the beryllium targets suggested that the dependence of the charm cross section on the mass number of the target (A), is given by $A^{0.72}$ [45].

The CCFRS collaboration performed a prompt lepton experiment at Fermilab, called E595. E595 detected prompt muons resulting from a 350 GeV/c proton beam incident upon a variable density iron target [46]. CCFRS reported that the prompt μ^- to μ^+ ratio is consistent with unity. Parametrizing the differential cross section in the form

$$\frac{d\sigma}{dx_F\, dp_T^2} \propto (1 - |x_F|)^n \exp(-b\, p_T^2)$$

the best fit to the background subtracted muon momentum spectrum yielded a value of 0.75±0.2 $(GeV/c)^{-2}$ for b, while the exponent n was determined to be 6.0±0.8 [47]. This x_F distribution is consistent with a central production mechanism. The total $D\bar{D}$ production cross section was reported to be 8.2±0.8±1.4 μb per nucleon for x_F greater than zero.

E595 also employed the same detector to study prompt muon production with an incident 278 GeV/c π^- beam [47]. The π^- beam data yielded a ratio of prompt μ^- to prompt μ^+ production of 1.78±0.20 in their detector. CCFRS interpreted this excess as evidence for the leading particle effect. A fit of the prompt muon momentum spectrum to the same differential cross section form used for the proton data yielded a value of 0.70±0.15 $(GeV/c)^{-2}$ for b. The x_F dependence of the μ^- and the μ^+ spectra were separately consistent with the same parent x_F distribution. To allow for the leading particle effect, the x_F dependence was fit to a combination of forward and central D production components. CCFRS reported that 24±16 percent of the total was forward with $n=0.9^{+0.9}_{-0.6}$, while the remainder was central with $n=5.9^{+3.2}_{-3.7}$, yielding a $D\bar{D}$ production cross section of $20.2^{+4.4}_{-3.7}$ μb per nucleon for x_F greater than zero. (In calculating the above results, the CCFRS collaboration assumed that 40 percent of the D meson decays which yield muons proceed through the mode $D\rightarrow K^*(890)\mu\nu$, while the remainder decay via the mode $D\rightarrow K\mu\nu$. Linear A dependence was also assumed.)

E567, a D^* search performed by Fitch et al. using a 200 GeV/c π^- beam incident upon a beryllium target, is an example of the bump hunting technique [48]. They employed the kinematic properties of the charged D^* decay mode $D^*\rightarrow D^0\pi$ to trigger upon and observe the D^*. A model dependent D^* production cross section of 4.2±1.4 μb was reported, and the ratio of D^{*+} to D^{*-} was observed to be 0.4±0.2. The same apparatus and technique were employed in E650 with a 250 GeV/c π^-

beam and slightly smaller integrated luminosity. E650 yielded an essentially null result of 0.8±2.9 μb for the D^* production cross section [49].

The prompt electron triggered experiment NA11 performed at CERN by the ACCMOR collaboration is another example of a bump hunting experiment. The strategy of NA11 was very similar to E515, but NA11 triggered on prompt electrons. Furthermore, their spectrometer had a larger prompt lepton acceptance, as well as more powerful particle identification and tracking capabilities. The NA11 trigger acceptance is centered about x_F of zero, while the reconstructed partner states must be forward in order to be detected. Some data was accumulated with a 150 GeV/c proton beam incident on a beryllium target [50]. By searching right-sign $K\pi$ and $K\pi\pi$ mass plots, NA11 reported 90 percent confidence upper limits on the inclusive production cross sections as follows:

$$\sigma(D^0) \leq 64 \text{ μb per nucleon}$$
$$\sigma(\bar{D}^0) \leq 37 \text{ μb per nucleon}$$
$$\sigma(D^+) \leq 51 \text{ μb per nucleon}$$
$$\sigma(D^-) \leq 49 \text{ μb per nucleon}$$

These results depend upon a variety of assumptions that were necessary to interpret the prompt lepton triggered data. ACCMOR observed small enhancements consistent with a total $D\bar{D}$ production cross section of 15 μb per nucleon. (To calculate the acceptance of the trigger arm, NA11 assumed that the kinematic variables of the charmed and anticharmed states are independent, and the electrons from D decays were assumed to arise from the decays $D \to K^*(890)e\nu$ and $D \to Ke\nu$ with equal probability.)

NA11 also recorded data with 175 and 200 GeV/c π^- beams incident upon a beryllium target. Based upon that data, the ACCMOR collaboration reported the observation of neutral D production with x_F greater than 0.2, (including 115±34 D→Kπ decays), and charged D production with x_F greater than 0.4 (89±31 D→Kππ decays) [51]. Using the previously described form for the differential cross section parametrization, the ACCMOR collaboration fit the background subtracted momentum spectrum of the D mesons observed in the Kπ and Kππ decay modes, and reported b=1.1±0.5 $(GeV/c)^{-2}$ and n=0.8±0.4. A value of six for n was excluded at the 95 percent confidence level. The resulting $D\bar{D}$ production cross section was reported to be 48±15±24 μb.

The data generated by the 175 and 200 GeV/c π^- beam also contained evidence for charged D^* production as observed through its decay into a neutral D meson and a charged pion. A fit to the x_F distribution of the D^* mesons yielded n=3.2±1.5. ACCMOR observed 15±5 D^{*+} and 13±5 D^{*-}, so the D^* production showed no leading particle effect. However, the number of observed D^- and D^0 relative to the number of D^+ and $\bar{D}^0$ was 2.0±1.0. ACCMOR also reported a neutral D to charged D production ratio of 1.4±0.8, and a D^* to D production ratio of $0.9^{+3.1}_{-0.6}$.

NA11 also measured charm production by a 120 GeV/c incident π^- beam in the same spectrometer, and reported that the ratio of $D\bar{D}$ production cross sections at 120 GeV/c to 175/200 GeV/c was 0.62±0.34.

With the installation of silicon microstrip detectors (MSD) surrounding their beryllium target, NA11 began using the vertex detection technique to identify charmed events. The MSD provided a substantial improvement in the vertex resolution and a corresponding suppression of backgrounds. Based upon data collected with a 200 GeV/c π^- beam, the prompt electron trigger, and the MSD, ACCMOR reported preliminary results on the observation of 25 neutral D decays including an estimated background of 1.1 decays, and 20 charged D meson decays including an estimated background of 2.1 decays [52]. The neutral D mesons were almost evenly divided between the D^0 and the $\overline{D}^0$ states. There were almost four times as many D^- mesons as D^+ mesons detected, and since the acceptance favored forward particles, this may be evidence of a leading particle effect. Note, however, that the neutral D mesons showed no such effect. Fitting the D momentum spectrum for the parameters of the differential cross section yielded $b=1.0^{+0.2}_{-0.1}$ $(GeV/c)^{-2}$ and $n=2.0\pm0.5$. Individual channels of leading and non-leading states were also fit independently, but no statistically significant difference in the x_F distributions were observed. The $D\overline{D}$ production cross section resulting from this data was $55\pm9\pm25$ μb per nucleon. Correcting for acceptance, the production ratios of the neutral D to charged D mesons was 1.8 ± 0.7. Four of the neutral D mesons were observed to arise from the decay of charged D^* mesons via the mode $D^*\rightarrow D\pi$.

Experiment NA18 used the freon filled bubble chamber BIBC as the target and vertex detector, and exposed it to a 340 GeV/c π^- beam. Employing an interaction trigger, they observed 9 neutral D mesons with an estimated background contribution of 1.4 decays, 7 charged D mesons (of which 6 were D^-) with an estimated background of 2.2 decays, and 5 F candidates with an estimated background of 2.4 decays. NA18 reported a $D\bar{D}$ production cross section of 28±11 μb per nucleon [53]. The x_F distribution of the observed D mesons was characteristic of leading particle production.

In experiment NA16, the high resolution bubble chamber LEBC was coupled with the European Hybrid Spectrometer (EHS) to detect the hadronic production of charm through the observation of the charmed decay vertices. The "minimum bias" trigger required the detection of three charged particles emerging from the bubble chamber for an event to be recorded. A 360 GeV/c proton beam incident upon the hydrogen filled LEBC yielded 29 D mesons and 3 F mesons [54]. The $D\bar{D}$ production cross section was estimated to be 19^{+13}_{-5} μb. The $\Lambda_c\bar{D}$ production cross section was 18^{+15}_{-10} μb. Fitting for the parameters of the differential cross section yielded $b=1.1\pm0.3$ $(GeV/c)^{-2}$ and $n=1.8\pm0.8$.

NA16 also accumulated data with a 360 GeV/c π^- beam [55]. The π^- data yielded evidence of eight D^0 mesons, five $\bar{D}^0$ mesons, two D^+ mesons, nine D^- mesons, and one F^+ meson. Correcting for the observed charged D^* mesons, NA16 reports 18 leading and 6 non-leading states detected, which is suggestive of a leading particle effect. A fit for

the parameters of the differential cross section for D production yielded $b=1.1\pm0.3$ $(GeV/c)^{-2}$ and $n=2.8\pm0.8$. When the π^- data was treated as composed of a central and a forward component, 70±30 percent of the D mesons were central with $n=6\pm3$, while the remainder were forward with $n=1\pm1$. The inclusive single D or $\overline{D}$ production cross section for x_F greater than zero was 40^{+15}_{-8} μb. Fourteen of the observed D mesons were members of fully reconstructed $D\overline{D}$ pairs, and thus a lower limit of 0.5 on the mean rapidity gap between the members of the pair was established.

Experiment NA27 employed a new LEBC and an improved EHS to detect 360 GeV/c π^- hydrogen interactions [56]. Using the minimum bias trigger, they observed 22 four prong neutral D decays. The associated charmed partner vertex was located in 19 of the 22 events containing a four prong neutral D decay. NA27 reported a single inclusive D or $\overline{D}$ production cross section of 10.3±3.5 μb for x_F greater than zero. Four of the fifteen D mesons which yielded a well defined final state were consistent with the decay of charged D^* mesons into neutral D mesons and charged pions.

As is apparent from the size of the uncertainties in the results summarized here, the current understanding of the hadronic production of charm is still far from complete. More research on the subject is planned [57]. Nevertheless, the hadronic production of charm has been observed in numerous experiments, and seems to have a cross section on the order of tens of microbarns at Fermilab energies and perhaps hundreds of microbarns at ISR energies.

Prior to the discovery of charm, Kobayashi and Maskawa proposed a generalization of Cabibbo mixing, which introduced two additional flavors beyond charm [58]. After the discovery of charm, evidence was reported for an additional heavy lepton, called the τ [59]. The observation of a 9.5 GeV/c^2 neutral state that decayed into a muon pair was the first direct evidence of another quark flavor, called bottom [60]. Mesons containing naked bottom have since been observed in e^+e^- annihilations [61]. The new CERN proton antiproton collider ($Sp\bar{p}S$) opened another energy domain for experimental particle physicists. As a result, direct evidence has been observed for the gauge bosons of the weak interaction, the $W^{\pm}$ [62] and the Z^0 [63]. The UA1 collaboration has observed charged D^* production at the $Sp\bar{p}S$ [64]. They have also recently presented evidence which they believe is consistent with the production of the sixth quark flavor, called top [65]. The study of the properties of heavy flavor production and decay continues to be of interest to the high energy physics community.

CHAPTER 2

APPARATUS

The spectrometer that was employed in this experiment is illustrated in figure 4. It was divided into two relatively independent detector systems referred to as the trigger arm and the forward arm. The trigger arm was composed of those detectors positioned above the plane which was inclined at about 42 mrad above the horizontal and passed through the target. The angular acceptance of the trigger arm extended from about -150 mrad to +150 mrad in the plan view, and from +42 mrad to +170 mrad in the elevation view. (For the 205 GeV/c π nucleon interactions studied in this experiment, 90° in the center of momentum frame corresponded to 95 mrad in the laboratory for massless particles.) The trigger arm consisted of absorber (mostly steel), scintillation counters, the yoke of the spectrometer magnet, and proportional wire chambers (PWC's). The

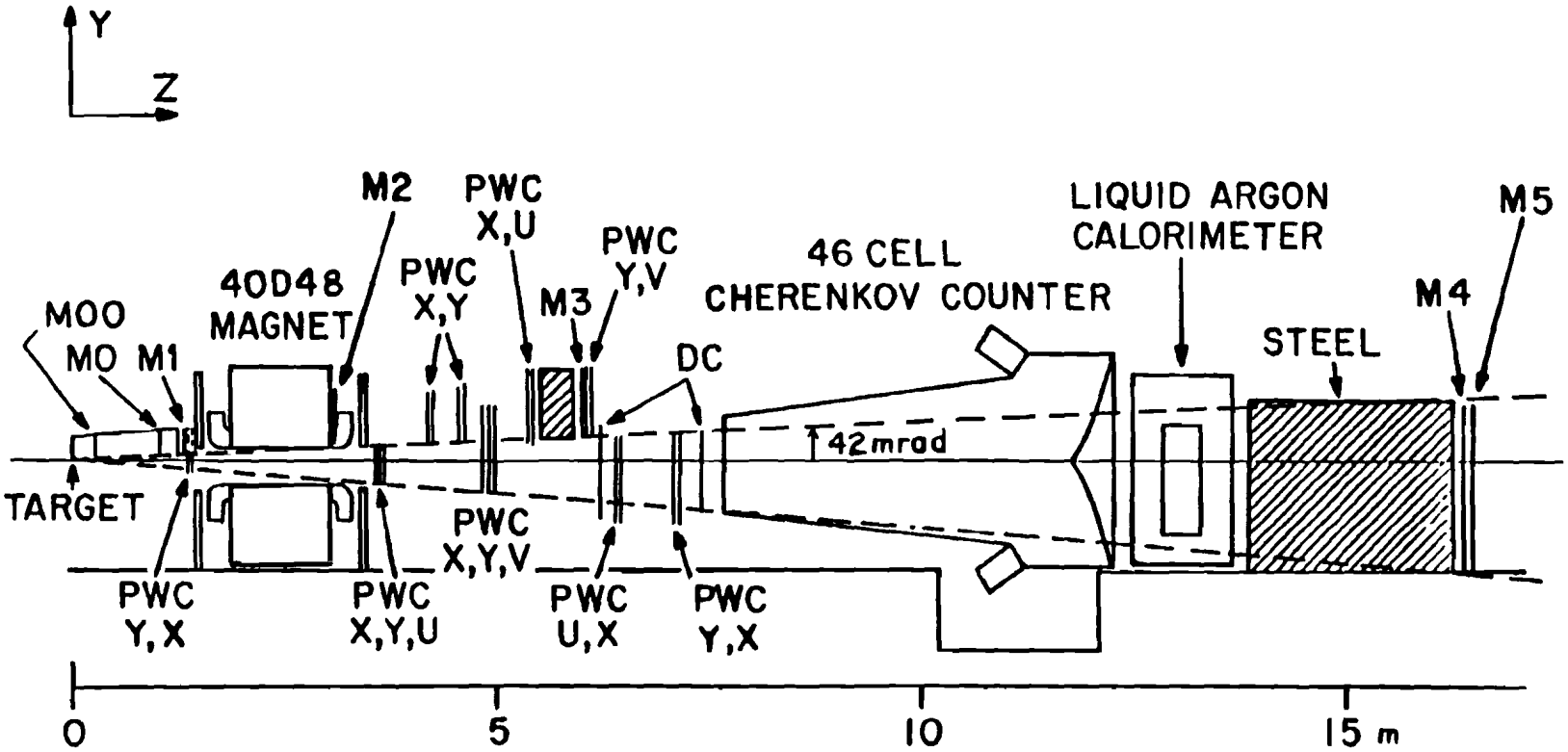

FIGURE 4. View of the E515 spectrometer, showing both the trigger and forward arms. The trigger arm was composed of those elements above the plane inclined at 42 mrad with respect to the horizontal. MOO, MO, M1, M2, and M3 were scintillation counters employed in the prompt muon trigger.

absorber filtered out showering and strongly interacting charged particles and thus distinguished muons from all other charged particles. The scintillators yielded fast information on the passage of charged particles. The PWC's supplied a higher resolution record of the path of charged particles in the trigger arm. The magnetized yoke provided the opportunity to measure the charge and the momentum of the triggering charged particle.

The forward arm was composed of those elements that were below the 42 mrad plane. The angular acceptance of the forward arm extended from about -200 mrad to +200 mrad in the plan view, and from -80 mrad to +42 mrad in the elevation view. The forward arm contained a large aperture dipole magnet, PWC's, drift chambers (DC's), a Cherenkov counter, a liquid argon calorimeter (LAC), and a forward muon identifier. The PWC's and DC's recorded the paths of the charged particles, and together with the magnet measured their charges and momenta. The Cherenkov counter aided in the identification of the charged particles. The LAC was primarily sensitive to electromagnetic showers and thus provided information on electrons and photons.

The coordinate system employed in the description of this spectrometer has its origin at the target center with the Z axis along the nominal direction of the incident beam, while the Y axis points up, and the X axis is parallel to the floor, providing a right handed coordinate system. The terms upstream and downstream are frequently employed in this document, and unless otherwise specified, upstream refers to locations with Z position less than the spectrometer magnet

midplane, while downstream refers to locations with Z positions greater than the spectrometer magnet midplane.

The first section of this chapter briefly describes the elements of the system which provided the particle beam to the experiment. The second section describes the hardware associated with the trigger arm of the spectrometer. The requirements made upon the event topology during the real time event selection are described in the third section. The forward arm hardware is described in the fourth section. The last section of this chapter discusses the recording of the data selected by the trigger logic, and the on-line monitoring of the collected data.

2.1 BEAM SYSTEM

The particle beam employed in this experiment was supplied by the Fermilab accelerator [66]. Negative hydrogen ions were initially accelerated in a Cockcroft Walton to an energy of 750 keV and then transferred to a linear accelerator (Linac) which raised the beam energy to 200 MeV. The hydrogen ions were then stripped of their electrons, and the protons were injected into the booster ring which is a proton synchrotron. The booster accelerated the protons to an energy of 8 GeV. The proton beam was then transferred to the Main Ring which is a separated function proton synchrotron capable of accelerating the protons to 500 GeV. The acceleration of the protons

in the Main Ring was performed by a series of radio frequency cavities excited at 53 megahertz. As a result, the proton beam was forced into bunches that were separated in time by 19 nsec. When the protons achieved the desired energy, the beam was extracted from the Main Ring, and split in the switchyard to provide beam simultaneously to several experimental halls. The beam employed in this experiment was extracted from the Main Ring via the slow extraction process, which resulted in a "steady" stream of protons, referred to as the "spill," whose duration was roughly one second. The Main Ring beam contained about 2×10^{13} protons per accelerator cycle, and cycles occurred approximately every ten seconds. The Main Ring control room also provided an electronic signal, referred to as the BEAMGATE signal, which coincided with the duration of the spill.

While E515 was accumulating data, about 3×10^{12} 400 GeV protons per spill were directed onto the Meson Center target located in the Meson Lab Target Hall. The interactions in the Meson Center target produced a secondary beam of particles which was transported in the M1 West beamline about 500 m to the E515 target. The beamline consisted of dipole and quadrupole electromagnets as well as collimators, profile monitors, and a beam stop [67]. The elements of the M1 West beamline were under the control of the experimenters through a computer terminal in the experiment control room. The beamline element currents were adjusted to transport a negatively charged beam with a nominal momentum of 200 GeV/c. An analysis of the tracks of beam particles observed in the E515 spectrometer indicated

that the mean beam momentum was 205 GeV/c. The beam delivered to the E515 target contained approximately 5×10^6 particles per spill. The vast majority of the particles in this secondary beam were expected to be pions [68]. Although the particle types of the individual beam particles were not identified in this experiment, a ring imaging Cherenkov test cell was positioned in the non-interacting beam which passed through our spectrometer. Based upon the data collected by that test cell, the beam composition during our data run was 96 percent negative pions, 3.5 percent negative kaons, and 0.5 percent antiprotons [69].

The elements of the beam system in the vicinity of the E515 target are shown in figure 5. The 4Q120 quadrupole magnets were employed in series to focus the secondary beam so that it was about 1 mm wide in Y at the E515 target. This narrow beam was employed to minimize the distance between the interaction point in the target and the absorber in the trigger arm. The vernier dipole magnet provided a trimming adjustment to steer the narrow beam onto the target. The profile of the beam in the X direction covered several centimeters at the target.

Three PWC's labeled BMX0, BMX1, and BMX2 were employed in the beamline to record the X position of the beam particles at the target. The beam chambers were located at Z positions of -6.3 m, -3.4 m, and -1.2 m. The PWC's had a sense wire spacing of 1 mm and aluminum foil cathodes. The active area covered by the beam PWC's was 0.14 m wide by 0.076 m high. The beam PWC's were instrumented with the fast amp

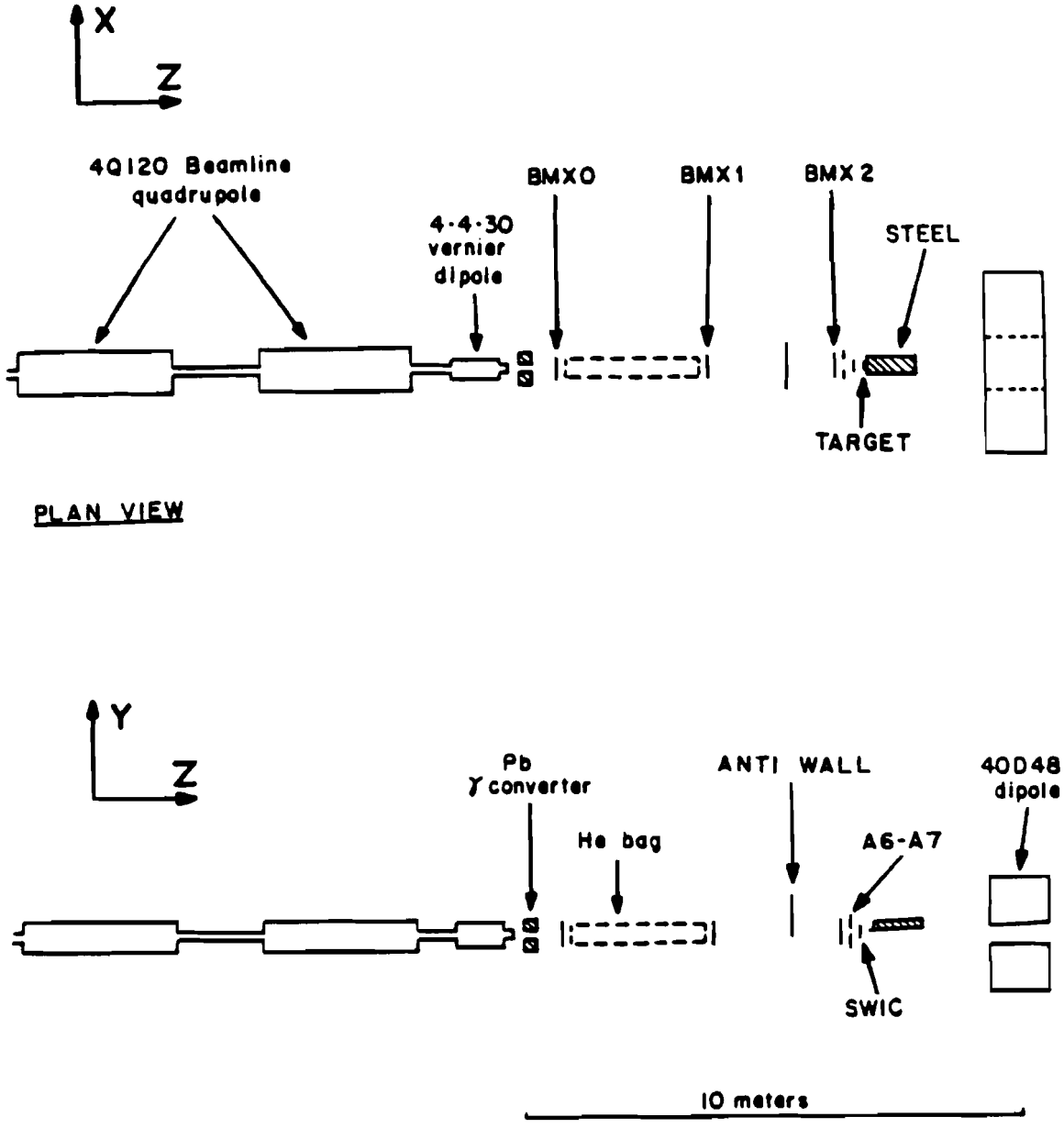

FIGURE 5. Elements in the M1 West beamline in the vicinity of the E515 target. BMX0, BMX1, and BMX2 were PWC's.

readout system in order to record the location of passage of charged particles through the PWC's. (The fast amp readout system is described in the subsection on the forward arm PWC's.)

The beam system also contained a wall of scintillation counters, called the "anti-wall," consisting of counters A1 through A5, as well as A8 and A9. The anti-wall was positioned to detect beam associated particles, referred to as beam halo, which were incident upon the trigger arm. The wall was about 1 m wide by 0.5 m high, and completely shadowed the trigger arm scintillation counters M0 and M1 while only partially shadowing M2 and M3. Upstream of the target were two additional scintillation counters, labeled A6 and A7, which provided protection against upstream interactions by forming a beam hole counter whose output was employed in veto. A segmented wire ionization chamber (SWIC) in front of the target provided a view of the beam profile on a spill by spill basis.

Immediately upstream of the target were two 11 cm wide (X) by 1 cm high (Y) by 0.16 cm long (Z) scintillation counters called B1 and B2. These counters were overlapped by 1.5 mm in Y, and centered directly in front of the target as illustrated in figure 6. The E515 target was a piece of beryllium, 12.5 cm wide by 0.2 cm high by 3 cm long. The top of the target was positioned 1 mm below the lowest edge of the trigger arm absorber. Beryllium has the advantageous property that it is a non-volatile solid with a large radiation length. The large radiation length is beneficial in the suppression of photon conversions in the target. The 3 cm long beryllium target corresponds

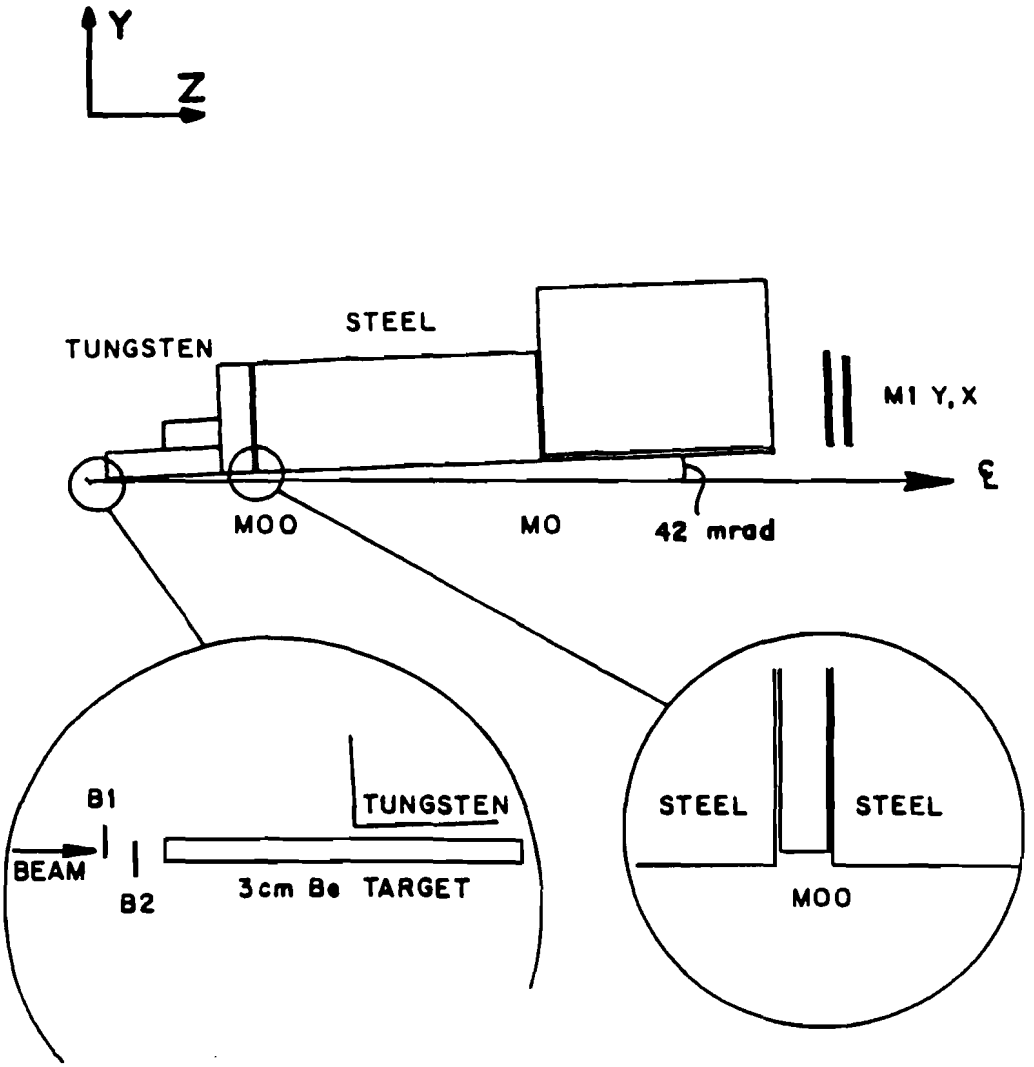

FIGURE 6. The beryllium target and upstream trigger arm absorber geometry.

to 0.085 radiation lengths [70] and 0.0514 nuclear absorption lengths [71].

Electronic signals from photomultiplier tubes attached to the various beam system scintillation counters were discriminated at minimum ionizing levels by fast NIM electronics [72]. The outputs of the discriminators were generally set to produce ten to twenty nanosecond wide NIM pulses which were inputs to various digital electronics modules, including coincidence units. The signal called A was generated whenever there was a signal from any of the veto counters in the beam system, that is,

$$A = A1 + A2 + A3 + A4 + A5 + A6 + A7 + A8 + A9$$

where the symbol + signifies the logical operation OR. A signal called BEAM was generated whenever signals from counters B1 and B2 arrived in coincidence and no signals from any of the veto counters were observed in time, that is,

$$BEAM = B1 * B2 * \overline{A}$$

where * signifies the logical operation AND, and the overline or bar represents the logical operation NOT. The occurrence of this signal implied that at least one valid beam particle had intercepted the target. Visual scalers attached to various scintillation counters provided a monitor of the beam conditions.

2.2 TRIGGER ARM

The active elements of the trigger arm are illustrated in figure 7. Information on the sizes and locations of the various active elements in the trigger arm is provided in table 1. Since the trigger for this experiment was intended to select prompt muons, absorber was placed as close as feasible to the target so as to increase the probability that long lived hadrons (such as pions and kaons) that have decay modes which include muons were absorbed before they decayed. Figure 6 illustrates the location of the trigger arm elements in the target vicinity. The first 0.15 m of absorber was tungsten (Hevimet). The remaining 0.76 m of absorber upstream of the spectrometer magnet was steel. Two scintillation counters, called M00 and M0, were sandwiched in the steel. M00, which was a 20 cm wide by 6 cm high by 0.3 cm long counter, was located 0.20 m downstream of target center. M0, which was a 42 cm wide by 10 cm high by 0.3 cm long counter, was located 0.58 m downstream of target center.

The next element in the trigger arm was the scintillation counter hodoscope M1, which was 0.98 m downstream of target center. The M1 hodoscope was composed of 26 individual scintillation counters arranged as illustrated in figure 8. M1 was divided into left and right halves. Each half contained seven X counters and six Y counters. The counters in each view (X and Y) were overlapped with their neighbors to achieve an effective cell size of 1 cm in low rate situations. This provided an angular resolution of about 10 mrad for

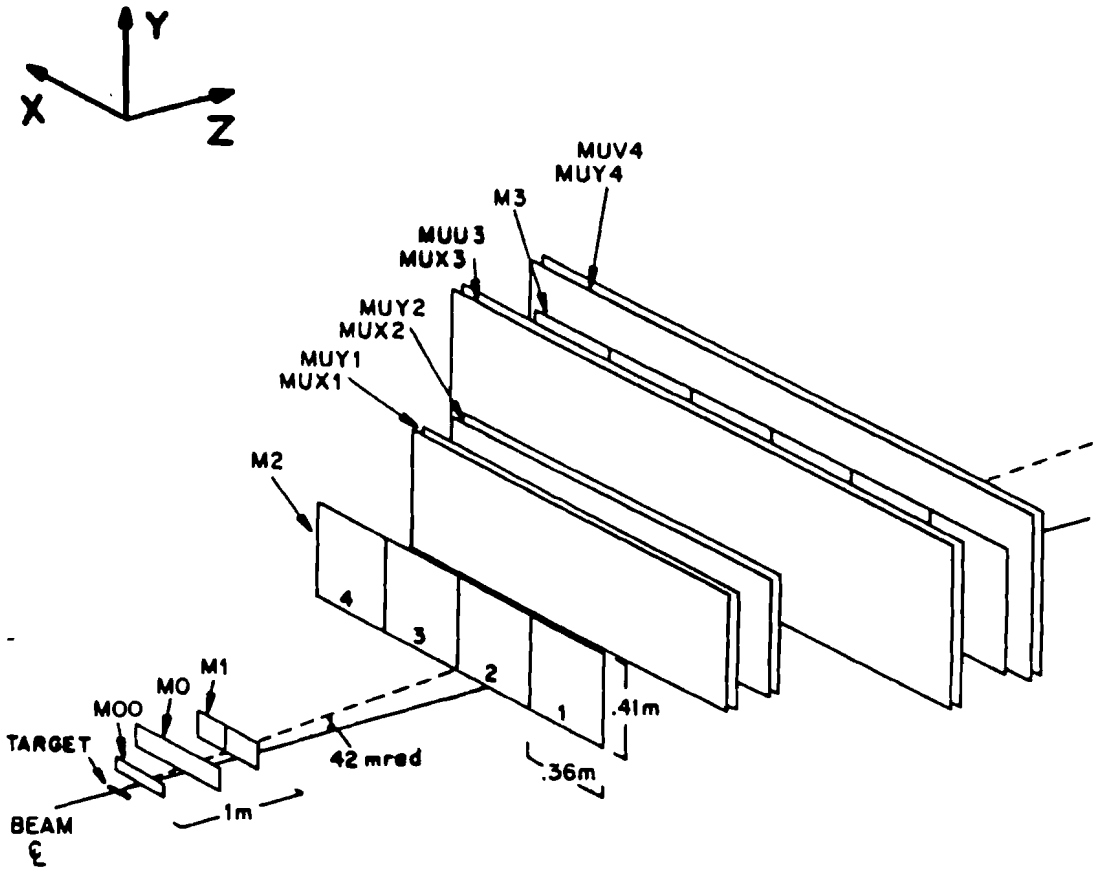

FIGURE 7. View of the active elements of the trigger arm. MOO, MO, M1, M2, and M3 were scintillation counter hodoscopes employed in generating the trigger. MUX1, MUX2, and MUX3 were X view PWC's. MUY1, MUY2, and MUY4 were Y view PWC's. MUU3 and MUV4 were rotated view PWC's. The PWC's were not involved in generating the trigger signal.

TABLE 1. Trigger arm detector element positions and dimensions.

Element	View	Z Position (m)	Cell Size (m)	Number of Cells	Active Area (m × m)	Average Number of Hits
TARGET		0.00				
M00	Y	0.20	0.20	1	0.20 × 0.06	
M0	Y	0.58	0.42	1	0.42 × 0.10	
M1 Y	Y	0.97	0.030	12	0.30 × 0.11	2.3
M1 X	X	1.00	0.030	14	0.30 × 0.13	2.5
M2	X	3.10	0.356	4	1.42 × 0.41	1.2
MUX1	X	4.12	0.006	256	1.54 × 0.48	2.2
MUY1	Y	4.20	0.006	80	1.54 × 0.48	2.0
MUX2	X	4.47	0.006	256	1.54 × 0.48	2.0
MUY2	Y	4.56	0.006	80	1.56 × 0.48	2.0
MUX3	X	5.30	0.006	400	2.40 × 0.70	2.3
MUU3	W	5.39	0.006	352	2.11 × 0.69	2.2
M3	X	5.98	0.358	6	2.15 × 0.51	1.1
MUY4	Y	6.06	0.006	112	2.42 × 0.67	2.0
MUV4	W	6.14	0.006	352	2.11 × 0.70	2.1

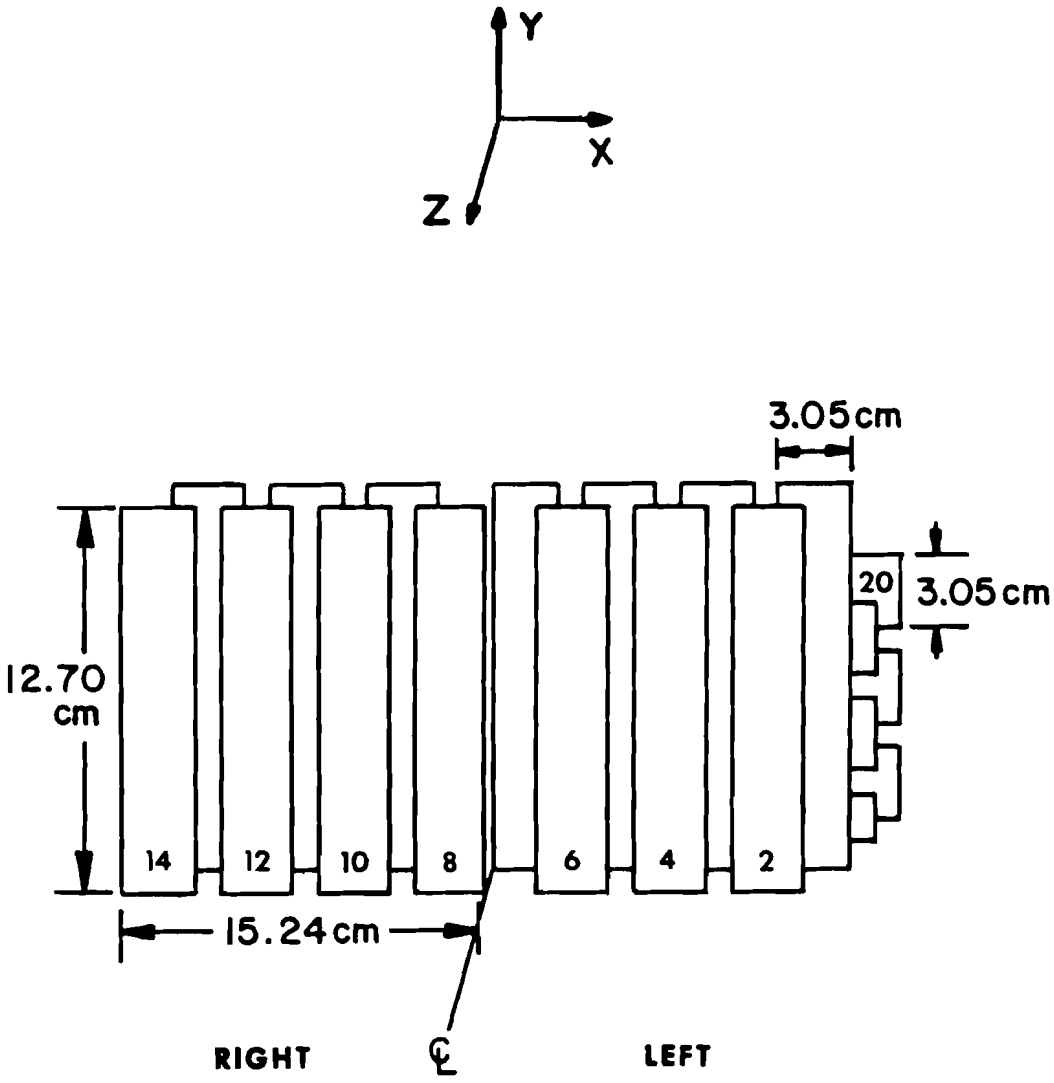

FIGURE 8. View of the M1 hodoscope showing the arrangement of the individual scintillation counters.

particles coming from the target.

Signals from the photomultiplier tubes attached to each scintillator element of M1, as well as M2 and M3, were individually discriminated at minimum ionizing level. The discriminated outputs were employed in the trigger logic and also sent to latches (LeCroy Model 2341A 16 channel coincidence registers), which recorded the state of the individual hodoscope elements at the time of the trigger.

The next element in the trigger arm was the spectrometer magnet. The return yoke of the magnet, which was 1.22 m long, served as additional absorber as well as a charge and momentum analyzer for particles passing through the trigger arm. Further details on the spectrometer magnet are included in the section on the forward arm. Placed between the downstream end of the magnet yoke and the magnet's saddle coil was a scintillation counter hodoscope called M2. The M2 hodoscope consisted of four 36 cm wide by 41 cm high by 0.3 cm long counters positioned side by side.

The next six elements of the trigger arm were PWC's. The proportional wire chambers MUX1, MUX2, and MUX3 measured the X coordinates of charged particles at the Z location of the chambers. Similarly MUY1 and MUY2 recorded the Y coordinates. MUU3 has its sense wire plane inclined at 16 degrees with respect to vertical and measured what is referred to as "rotated" coordinates. Following the PWC's was an additional 0.4 m of steel, referred to as the downstream trigger arm absorber, which provided additional hadron rejection. The M3 hodoscope, which consisted of six scintillation counters mounted

side by side, was located just beyond the absorber. The individual elements of M3 were 36 cm wide by 51 cm high by 0.3 cm long. Beyond M3 were two more PWC's which recorded Y coordinates (MUY4) and rotated coordinates (MUV4) for tracks passing through their active areas.

All eight trigger arm PWC's employed the same basic design. The anode or sense plane of each PWC was composed of 1 mil gold plated tungsten wires with a wire spacing of 3 mm. Pairs of adjacent wires were soldered together, resulting in an effective 6 mm sense wire spacing. The two cathode planes were constructed from 3 mil gold plated tungsten wires. The PWC's were filled with a gas mixture which was 70 percent argon and 30 percent isobutane. The operating voltages for the PWC's were generally between 3.0 and 3.5 kV.

The passage of a charged particle through the PWC ionized the gas and generated an electrical signal on the sense wire nearest the trajectory of the charged particle. Each soldered pair of sense wires was connected to a TTL amplifier and discriminator. Any signal on the sense wire which was above the threshold of the discriminator fired a 450 nsec one-shot, which served as a temporary memory, allowing time for the trigger logic decision to be made. If a trigger was generated, latches for each trigger arm PWC sense wire pair were cleared and then gated. If a sense wire had a "hit," that is, a signal above threshold in time with the trigger, and no other hit was generated on that wire during the 450 nsec delay, then the hit was latched. The amplifier, discriminator and latch channels for each effective sense wire cell are grouped into sets of sixteen. An OR of

the state of all sixteen channels in each set was generated, and is referred to as the MOR. A CAMAC [73] interface module received the trigger and initiated a scan through all the sets of sixteen channels. Each time a set was found which had a MOR on, it indicated that at least one channel in that set had a hit. A 16 bit data word, which encoded the location of the hit, was recorded for every latched hit in the PWC system. The hits were written into a CAMAC 1024 word buffer memory. Additional details on the trigger arm PWC construction and electronics are available in reference [74].

2.3 TRIGGER LOGIC

The trigger selects the interactions to be recorded for further analysis. E515 intended to trigger upon prompt muons generated by interactions in the target in order to study the hadronic production of charm. The two primary elements of the E515 prompt muon trigger, referred to as BEAM and M, were electronic signals derived from coincidences of scintillation counter signals. The signal BEAM indicated the presence of a beam particle in the target unaccompanied by beam halo, while M implied a coincidence consistent with the passage of a muon through the trigger arm. (The beam, target and absorber geometry were designed to discriminate in favor of muons of prompt origin.)

The signal M was composed of several elements. Figure 9 shows a schematic logic diagram for the signal M1, which was generated by signals from the hodoscope M1. The discriminated outputs from all the left half X elements of M1 were OR'ed to form the output signal M1XL. Similarly discriminated outputs from the left half Y elements were OR'ed together to form M1YL. The right half M1 elements were processed similarly to produce the signals M1XR and M1YR. The output signal M1 was generated by a coincidence between signals from at least one X and one Y element in the same half of the M1 hodoscope, which can be expressed as follows:

$$M1 = (M1XL * M1YL) + (M1XR * M1YR).$$

Outputs from the M2 and M3 hodoscopes were combined to form a signal referred to as MX. Figure 10(a) illustrates which combinations of individual M2 and M3 hodoscope elements generated a signal MX, and figure 10(b) shows the associated schematic logic diagram explicitly. Any combination of M2 and M3 hodoscope elements which generated an MX signal is referred to as an "M2 M3 road." An MX signal implied a coincidence between M2 and M3 hodoscope element signals consistent with the passage of a particle whose XZ slope was not greater than 250 mrad in magnitude. This road requirement lowered the trigger rate by rejecting large angle coincidences, but it also reduced the acceptance of the spectrometer. The signal M was generated by the coincidence

$$M = M00 * M0 * M1 * MX$$

where M00 and M0 were the discriminated signals from the scintillation

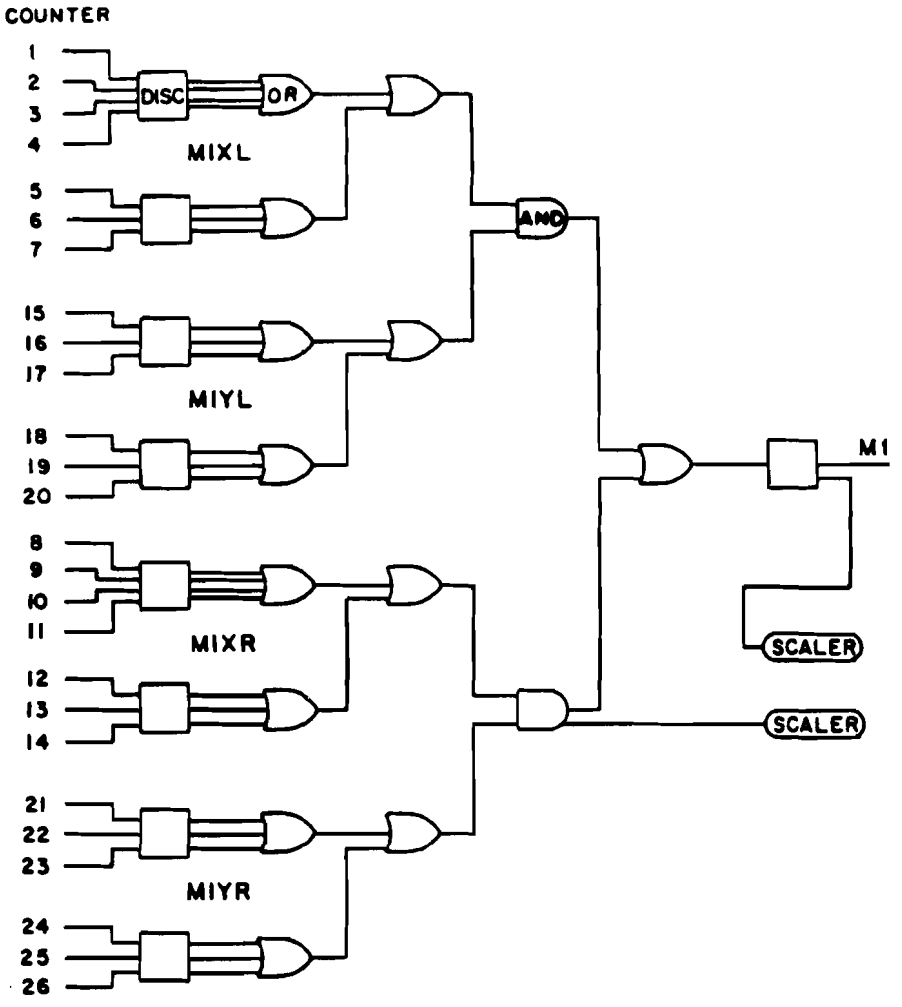

M1 HODOSCOPE LOGIC

FIGURE 9. Schematic logic diagram for the processing of signals from the M1 hodoscope to generate the logic signal M1.

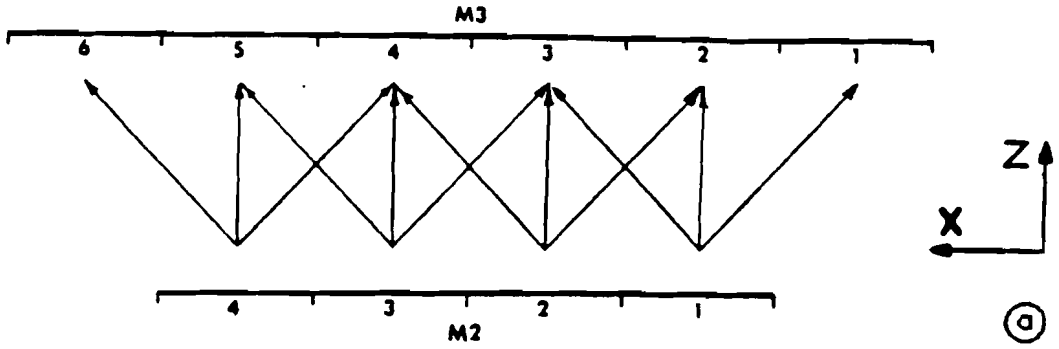

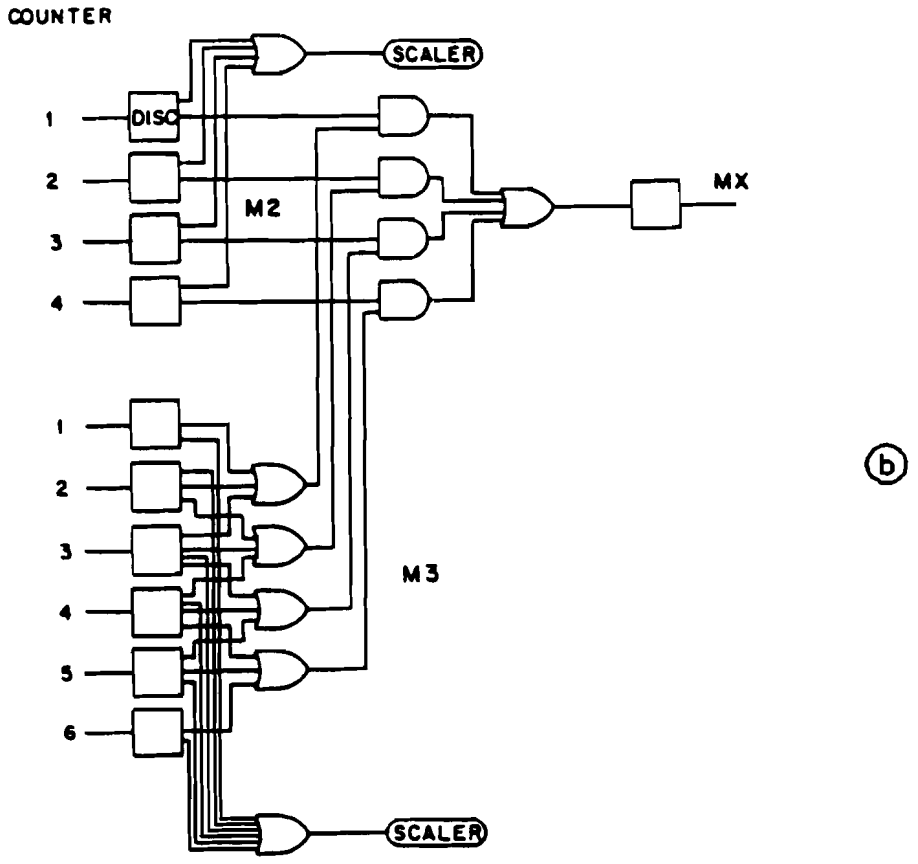

FIGURE 10. The M2 M3 road. (a) Illustration of the combinations of M2 and M3 hodoscope elements that formed pairs which generated the signal MX. (b) The associated schematic logic diagram.

counters M00 and M0 respectively. The signal M is interpreted as evidence of the passage of a muon through the trigger arm, since a single particle generating the necessary signals must have traversed at least 2.4 m of steel, which corresponds to 14 nuclear absorption lengths [70].

The signal BEAM*M was the signature of interest in this experiment. In order to avoid re-triggering the spectrometer after a valid trigger was detected but before the processing of that first trigger was complete, the spectrometer was only triggered in the absence of a signal called DT (deadtime). The signal DT indicated that the data acquisition system was busy. The signal DT was generated by the OR of two signals,

$$DT = FDT + SDT.$$

The output of the coincidence unit which generated the trigger was connected directly to a discriminator which generated the signal FDT (fast deadtime). The FDT signal duration was long enough to allow the trigger signal to travel to the experimental control room, where the signal SDT (slow deadtime) was generated and sent back to the fast trigger logic before the FDT signal expired. SDT was maintained until the computer completed the readout of all the information associated with this trigger.

The coincidence BEAM*M*$\overline{DT}$*BEAMGATE is referred to as a "prompt muon trigger." (Recall that BEAMGATE was the signal sent by the accelerator which represented a spill in progress.) Whenever a prompt muon trigger occurred, a signal was issued that latched the

information gathered by various components of the spectrometer. This trigger signal also indirectly initiated the recording of the latched information onto magnetic tape. A schematic diagram of the trigger logic is shown in figure 11.

Concurrent with the prompt muon trigger, a diagnostic trigger defined by BEAM*$\overline{DT}$*BEAMGATE was recorded once every 10^7 times such a signal was generated. These "pre-scaled beam triggers" provided a monitor on the overall alignment and performance of the chamber system.

At various times during the experiment, small amounts of diagnostic data were accumulated with a variety of other special triggers and spectrometer conditions for purposes of spectrometer alignment, calibration, and trigger studies.

2.4 FORWARD ARM

The various elements that constituted the forward arm are shown in figure 12 and described in the following subsections.

2.4.1 4OD48 Spectrometer Magnet

The spectrometer magnet was a steel dipole electromagnet. The yoke of the magnet was 2.5 m wide by 2.1 m high and 1.2 m long. The aperture was 1.0 m wide and 0.4 m high. A brass shim was installed on

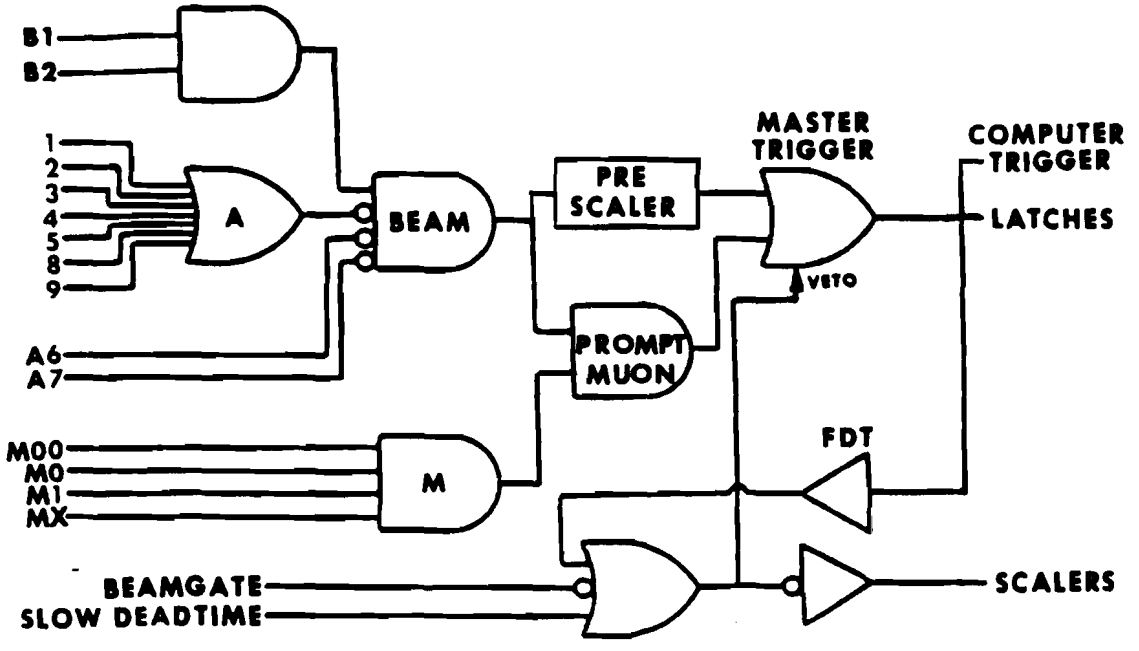

FIGURE 11. Schematic diagram of the trigger logic for both the prompt muon and pre-scaled beam triggers.

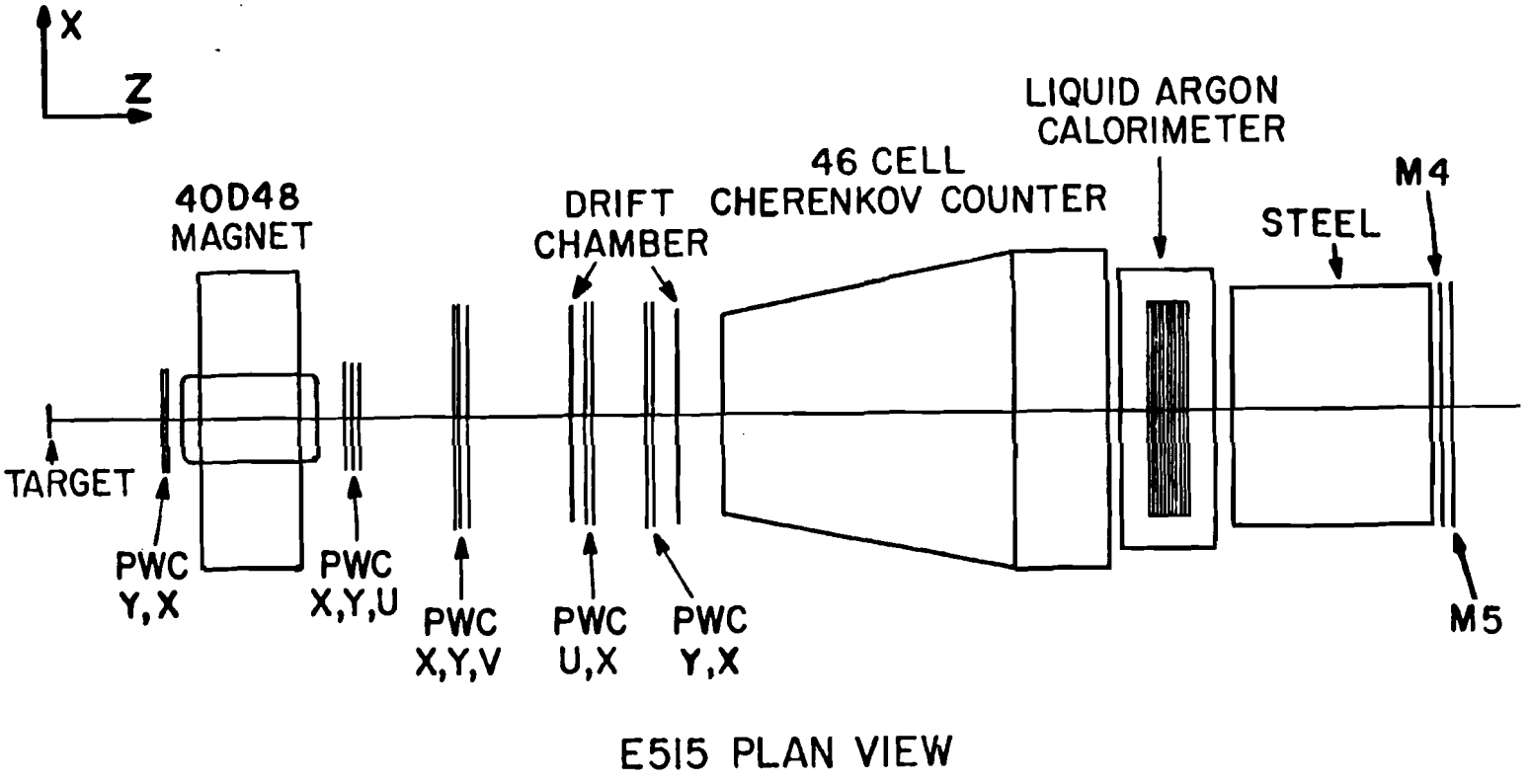

FIGURE 12. Layout of the forward arm detector elements.

the upper pole face to provide absorber above the 42 mrad plane separating the forward arm from the trigger arm. The 40D48 also had 5.4 cm thick mirror plates installed on both ends of the magnet. The distance between the mirror plates was 2.1 m, and the downstream mirror plate aperture was 1.0 m wide by 0.4 m high. The saddle coils for the magnet were water cooled. A polyethylene bag, whose ends were 0.15 mm thick, was installed in the magnet aperture and inflated with helium to minimize multiple Coulomb scattering in the large gap.

The X coordinate of the magnet center was at 0.0 m, while the Y coordinate was -0.076 m, and the Z coordinate was 2.43 m. The 40D48 magnet's symmetry axes were slightly rotated with respect to the E515 coordinate system, with the largest rotation being 4 mrad about the Y axis.

The magnetic field was measured with a search coil probe [75] and the measurements were calibrated with the nuclear magnetic resonance technique. The absolute value of the field integral is believed to be within one percent of the measured value. Figure 13 illustrates some of the results of the magnetic field measurements. Details on the mapping of the magnetic field are described elsewhere [76].

During data acquisition, the 40D48 current was monitored and controlled with the same system that controlled the elements of the M1 West beamline. The magnet current was set at 2400 amps and was generally maintained within ±2 amps of that value. A one amp shift in the excitation current corresponded to a fractional change of 0.0002 in the measured particle momenta, which is negligible compared to the

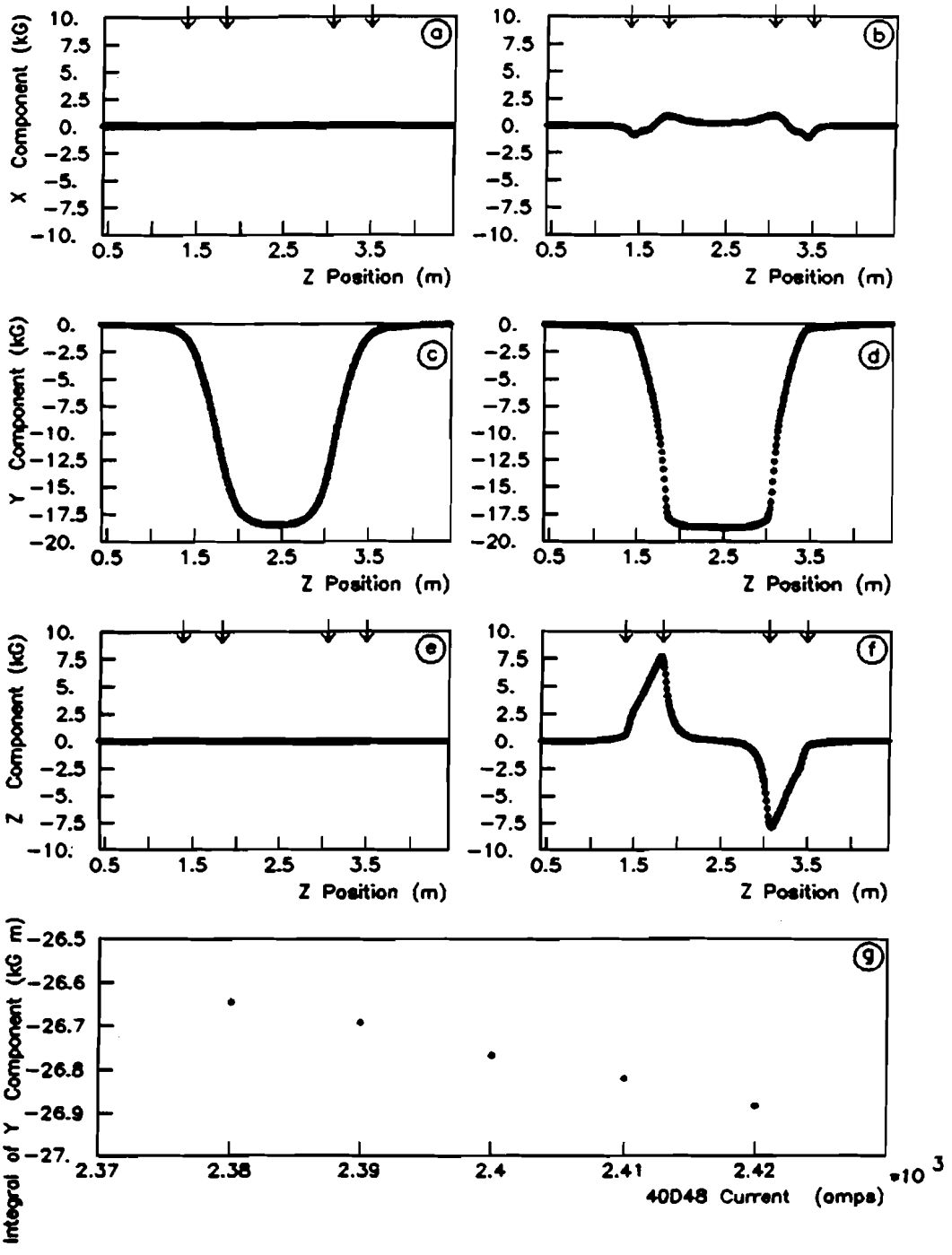

FIGURE 13. 40D48 magnetic field. (a) B_X as a function of Z along a line through magnet center. (b) B_X as a function of Z along a line near the edge of the magnet aperture. (c) B_Y along the magnet center line. (d) B_Y along the magnet aperture edge. (e) B_Z along the magnet center line. (f) B_Z along the magnet aperture edge. (g) Integral of magnetic field as a function of excitation current.

uncertainties in momenta caused by multiple scattering. The current generated a central field of 18.6 kilogauss in the negative Y direction, making the XZ plane the bend plane of the magnet. The field provided a 0.80 GeV/c transverse momentum impulse.

2.4.2 Forward Arm Proportional Wire Chambers

The twelve PWC's in the forward arm were naturally divided into two sets by their physical dimensions. The five smaller chambers deployed around the 40D48 mirror plates are referred to as "magnet chambers," while the larger chambers are called "downstream chambers." Table 2 lists some details on the positions and dimensions of the forward arm chambers. There were only two forward arm PWC's upstream of the magnet, one measuring X coordinates (UPMX), and the other measuring Y coordinates (UPMY). Downstream of the magnet there were four X PWC's, three Y PWC's, and three rotated PWC's (also referred to as W chambers) whose sense planes were rotated by ±14 degrees from the vertical.

The cathodes planes of the beam and magnet chambers were made of 1.5 mil thick aluminum foil which was epoxied under tension to the printed circuit boards mounted on the aluminum frames of the chambers. The cathodes of the downstream chambers were composed of 2.5 mil gold plated tungsten wires that were glued under a tension of 2 newtons to the printed circuit boards mounted on the chamber frame. There were

TABLE 2. Beam system and forward arm detector element positions and dimensions.

Element	View	Z Position (m)	Cell Size (m)	Number of Cells	Active Area (m × m)	Average Number of Hits
BMX0	X	-6.25	0.001	128	0.14 × 0.08	1.3
BMX1	X	-3.37	0.001	128	0.14 × 0.07	1.5
BMX2	X	-1.23	0.001	128	0.14 × 0.07	1.4
TARGET		0.00				
UPMY	Y	1.23	0.001	416	1.16 × 0.44	32.1
UPMX	X	1.28	0.001	576	0.61 × 0.37	37.5
DNMX	X	3.63	0.002	520	1.10 × 0.45	15.0
DNMY	Y	3.69	0.001	416	1.16 × 0.44	15.4
DNMW	W	3.74	0.002	466	0.99 × 0.46	14.0
DNX1	X	4.69	0.002	1160	2.46 × 1.09	12.6
DNY1	Y	4.88	0.002	379	2.66 × 0.80	12.2
DNW1	W	5.04	0.002	1065	2.25 × 1.09	14.3
DCX1	X	6.37	0.02	96	1.92 × 1.03	20.8
DNW2	W	6.70	0.002	1070	2.26 × 1.09	6.6
DNX2	X	6.83	0.002	1056	2.24 × 1.09	12.7
DNY2	Y	7.28	0.002	502	2.63 × 1.06	13.2
DNX3	X	7.37	0.002	1056	2.24 × 1.09	11.0
DCX2	X	7.69	0.02	96	1.92 × 1.02	19.4
M4	Y	17.70	0.025	128	3.09 × 1.65	
M5	X	18.01	0.146	18	2.62 × 1.40	

24 cathode wires to the inch. Due to the long free length of the cathode wires, support wires were installed around the wire cathode plane to insure stability.

The anode or sense planes of the forward arm PWC's were made of 0.8 mil gold plated tungsten wires with a wire spacing of either 12 or 24 wires per inch. Chambers with 12 wires per inch anode planes were referred to as "2 mm chambers" and those with 24 wires per inch were referred to as "1 mm chambers." The anode wires were glued at a tension of 0.5 newtons to the printed circuit boards mounted on the aluminum frame. Individual anode wires of the PWC's were soldered to printed circuit board traces that led to connectors for the PWC readout electronics. The beam and magnet chambers had an anode to cathode gap of 0.192 inch, while the downstream chambers had a gap of 0.250-inch. Mylar windows were glued to the outside of the chamber frames.

The 1 mm chambers employed a gas mix of 80 percent argon, 19 percent isobutane, 1 percent freon. This gas mix was bubbled through liquid dimethoxymethane. The 1 mm chambers operated at approximately 5 kV. The 2 mm chambers used a gas mix composed of 80 percent argon, 20 percent carbon dioxide, and 0.3 percent freon. The 2 mm magnet chambers operated at approximately 3 kV and the 2 mm downstream chambers operated at about 3.6 kV.

Each individual sense wire required an amplifier, discriminator, and memory system to temporarily store its information until a trigger decision was made. In an attempt to limit the costs of instrumenting

the 9000 sense wires of the PWC's, three different types of readout systems were employed. The "fast amp system" was capable of handling the highest hit rate, but was the most expensive, and was thus deployed only in the central regions of all the forward arm PWC's. The outer portions of most of the PWC's were instrumented with a lower rate readout system referred to as the "slow amp system." A third type of readout, called the "shift register system," was employed in regions of chambers DNX1 and DNY2.

Each channel of the fast amp system consisted of an AC coupled four stage amplifier followed by a Schmitt trigger, and differential line driver. The threshold of the Schmitt trigger was adjustable, and was set using a test pulse scheme. The output width of the line driver was also adjustable, and it was set to approximately 50 nsec. Output signals were directed onto 200 feet of Ansley flat cable, which had a propagation delay of 300 nsec. The far end of the Ansley cables were attached to differential line receivers and latches. The trigger served as the latch signal, and the latches recorded any hits observed in time with the trigger. Every latched hit was encoded into a 16 bit data word and written into a CAMAC 1024 word buffer memory. The fast amp electronics were employed to read out 2383 sense wires in this spectrometer, and the mean number of fast amp hits was 69 per event.

Each channel of the slow amp system consisted of an AC coupled three stage amplifier followed by a discriminator that provided a standard charge to a one-shot. The standard charge was achieved by adjusting a potentiometer on each individual amplifier channel using a

test pulse as input. The one-shot duration was adjusted to 400 nsec via a control voltage. A flip-flop circuit directed alternating signals on the same channel to one of two parallel one-shots, thus allowing two hits on the same sense wire within the one-shot duration without loss of information. The output of the one-shot was presented to a Schmitt trigger whose output was differentiated and sent to a latch. If a hit was in time with a trigger, it was latched. Every latched hit was encoded into a 16 bit word and stored into a 1024 word CAMAC buffer memory. The slow amp system was used to instrument 5267 sense wires in the spectrometer, and there were on average 116 slow amp hits per event. Both the fast and the slow amp systems employed ECL logic on the amplifier cards. The entire fast and slow systems are described in detail elsewhere [77].

Each channel of the shift register system consisted of an amplifier, an adjustable one-shot, and an element of a shift register chain. The trigger latched the state of each sense wire into its register. This system was capable of handling only one hit per sense wire within the delay time of the one-shot. The shift register chain connected all channels of the shift register system. The hits were encoded by shifting the contents of the chain towards the controller at the head of the chain. Each time a hit was found, it was encoded into a 16 bit data word which indicated the original location of the hit within the chain. The hits were stored into a 1024 word CAMAC buffer memory. The clocking of the chain continued until all elements of the chain had advanced to the controller. A problem was

encountered with the connection in the shift register chain between DNY2 and DNX1, resulting in the frequent loss of the shift register hits from DNX1. The shift register system was used to instrument 1390 anode wires in the spectrometer. The average number of shift register hits was 18 per event.

2.4.3 Drift Chambers

Drift chambers provided the possibility of better coordinate resolution than PWC's because the DC's measured not only the location of the wire nearest the passing charged particle, but also the transit time for the generated signal to drift to the nearest sense wire. Since the DC provided no information regarding which side of the sense wire the charged particle passed, a twofold ambiguity was generated.

The two DC's in this experiment were positioned downstream of the 40D48 at Z locations of 6.4 m and 7.7 m. Both chambers measured X coordinates. Each chamber had 96 sense wires with 2 cm between sense wires, and an active area that was 1.9 m wide by 1.0 m high. The DC's employed a gas composed of equal parts argon and ethane. The drift speed of the electrons in the gas was approximately 0.05 mm per nsec.

Signals from each sense wire were directed to LeCroy DC201A amplifier, discriminator, and line driver circuits. Output signals traveled 200 feet over 100 ohm twisted pair cable to the LeCroy 2770A DC readout system, which included time to digital converters (TDC's).

A signal above threshold on an individual channel started the timer for that channel. Receipt of an appropriately delayed trigger stopped the timer on all channels, and initiated the digitization of the recorded times for all channels. This system was continuously updatable, but capable of encoding at most one signal for each sense wire. If more than one signal occurred on an individual channel, only that signal which corresponded to the longest drift time was recorded. Thus the DC had a hit rate limitation of about 4 MHz on any individual wire, so the DC's were positioned relatively far downstream where lower rates per sense wire were anticipated. The region of the DC through which the non-interacting beam passed was not intentionally deadened. The 2770A drift chamber digitizer generated one 16 bit word for each wire which had a signal. Eight bits were employed to encode the time information, and seven bits to encode the wire number.

2.4.4 Cherenkov Counter

A large atmospheric nitrogen threshold Cherenkov counter was located downstream of the last DC. The threshold momentum for the generation of Cherenkov radiation in atmospheric nitrogen by various particles is:

electrons	0.02 GeV/c
muons	4.3 GeV/c
pions	5.7 GeV/c
kaons	20.2 GeV/c
protons	38.3 GeV/c

Thus the Cherenkov counter can be employed to distinguish pions and less massive charged particles from kaons and more massive charged particles in the momentum range of 6 to 20 GeV/c.

The Cherenkov counter contained 4.3 m of radiator. The counter was highly segmented to minimize the confusion caused by the multitude of particles produced in a single high energy interaction. As shown in figure 14, the counter had 24 cells above and 22 cells below the beam centerline. Each cell consisted of a five inch diameter RCA 4522 photomultiplier tube mounted in a 15 cm wide aluminized cone which was facing one of twelve cylindrical mirrors. The aluminized mirrors had a two meter radius and were mounted on foam supports to minimize the material in front of the LAC. The mirrors were positioned so as to leave a 10 cm wide slot between the upper and lower banks of photomultiplier tubes in an attempt to decouple the upper and lower halves of the counter. A larger hole was cut into the center mirrors to avoid collecting Cherenkov light from the non-interacting beam particles.

Signals from the photomultiplier tubes were amplified in LeCroy amplifiers and then digitized in LeCroy CAMAC model 2249A analog to digital converters (ADC's) in the experiment control room. The ADC's integrated over a 100 nsec gate initiated by a trigger.

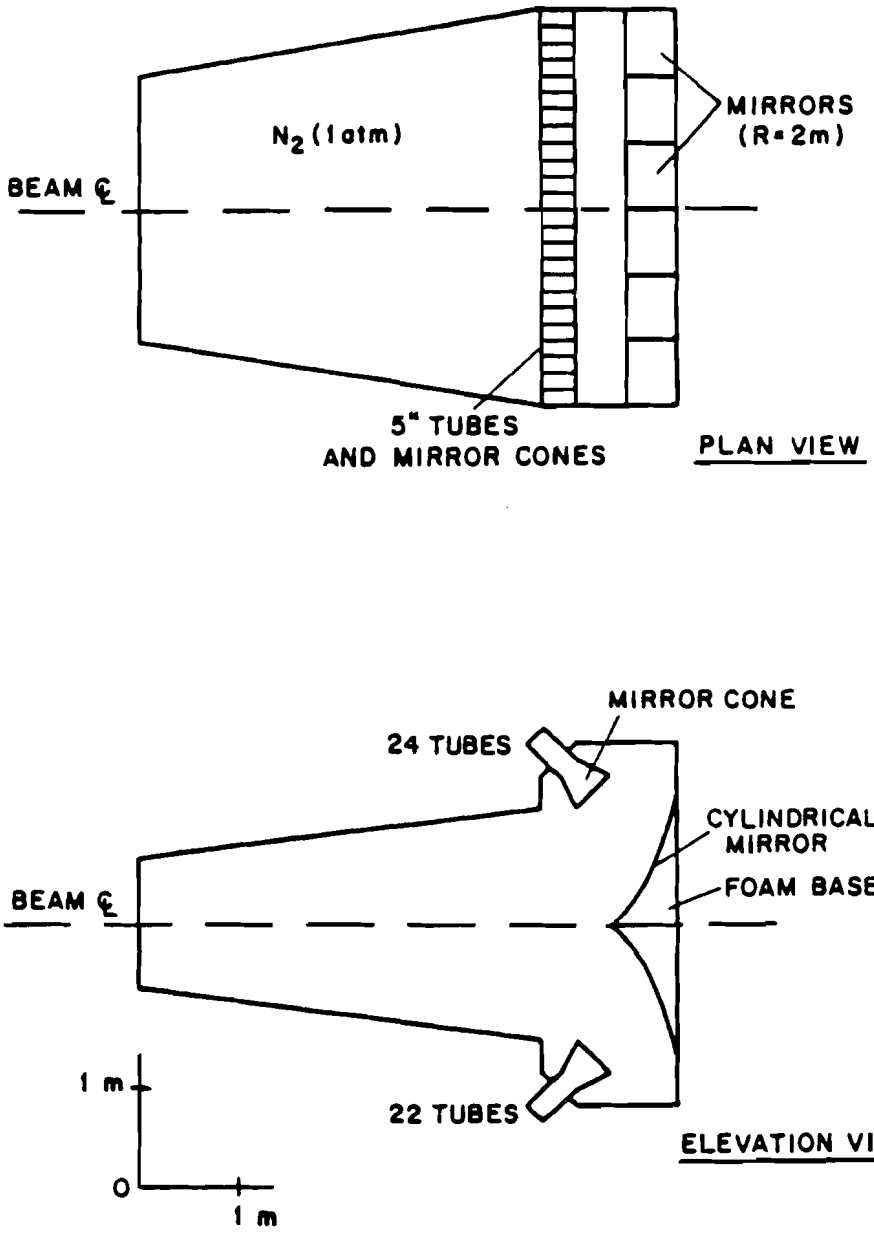

FIGURE 14. Nitrogen gas threshold Cherenkov counter.

2.4.5 Liquid Argon Calorimeter

The liquid argon calorimeter was designed to be sensitive to electromagnetic energy and thus useful for detecting gamma rays and electrons. Details on the construction and performance of the LAC are available elsewhere [78].

2.4.6 Forward Arm Muon Identifier

The forward arm muon identifier is illustrated in figure 15. It was composed of 2.9 m of steel followed by the M4 and M5 hodoscopes. The M4 hodoscope was an array of proportional tubes arranged to measure the Y coordinates of charged particles. The M5 hodoscope was a set of 18 scintillation counters which measured the X coordinates of charged particles. There was a 20 cm by 20 cm hole in the steel, positioned to allow the non-interacting beam to pass through the spectrometer.

2.5 DATA LOGGING AND ON-LINE MONITORING

The data logging and on-line monitoring employed a PDP11/45 minicomputer [79]. The computer was executing a modified version of the Fermilab data acquisition and analysis program RTMULTI [80], under the single user RT-11SJ operating system [81]. Peripherals attached

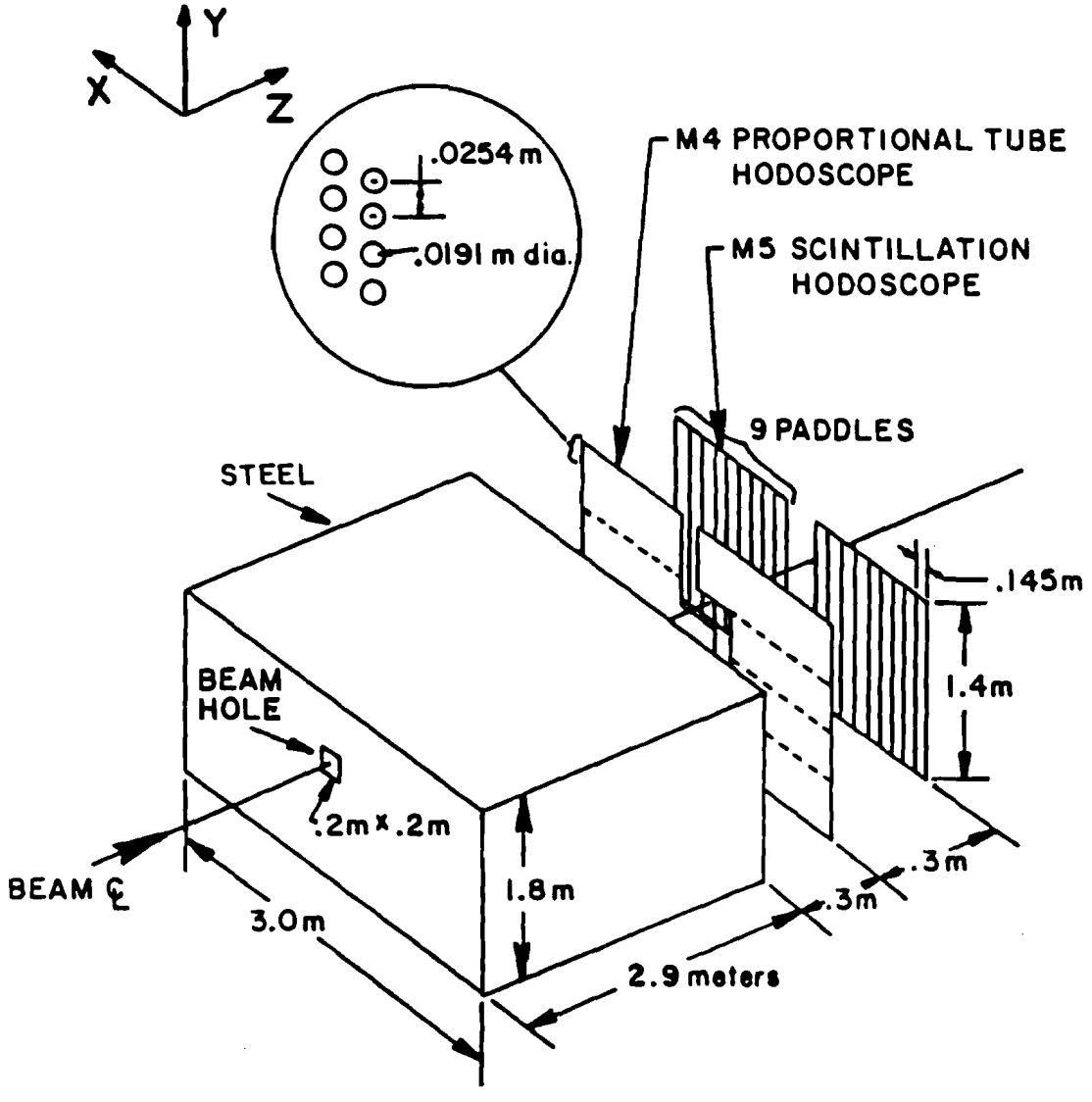

FIGURE 15. The forward arm muon identifier.

to the PDP11 included several hard disks, a 6250 bpi magnetic tape drive, DECTAPE drives, an ADM terminal, a Tektronics 613 display scope, and a Jorway JY411 CAMAC branch driver [82].

Receipt of a trigger from the fast logic of the experiment initiated a readout cycle. The eventual result of the readout cycle was the recording of an "event" on magnetic tape. An event is the information gathered by the spectrometer in coincidence with the trigger. If the various detector elements have the proper relative timing, the event will generally be a record of an individual interaction between an incident beam particle and a target nucleon. Each event was assigned an ordinal event number which was also recorded on magnetic tape with the event. In order to aid in the bookkeeping, the events were accumulated in logical units, referred to as "runs," and each run was assigned an individual run number which was also recorded on magnetic tape for each event.

As previously described, all the detector elements in the spectrometer eventually transferred the information they gathered about the triggered event into CAMAC modules which served as temporary memory. The various CAMAC modules were distributed among five CAMAC crates. Each CAMAC crate was controlled by a Type A-1 crate controller, and the five crates were connected via a parallel branch highway to the JY411. When a trigger signal generated by the fast logic arrived in the experiment control room, it was sent to the Bison Box [83], which generated a computer interrupt, referred to as an "A interrupt." The Bison Box also issued the SDT (slow deadtime)

signal and maintained it until the PDP11 completed readout of the event. When the computer acknowledged the interrupt, it initiated the readout of the information stored in the CAMAC modules associated with the individual detector elements. The information from the various detectors was transferred into the PDP11 memory via DMA (direct memory access) transfers in a fixed order. (The order was selected based upon the time order in which various detector elements were anticipated to be finished filling their individual CAMAC modules.) For those detector elements which required variable amounts of time to encode their data, the computer waited until it received a ready signal indicating the CAMAC module filling was complete, and then it read out the module. Upon completion of the readout of the last detector element, the deadtime signal was lifted and the spectrometer was prepared to handle another trigger. The readout of an individual prompt muon triggered event required between five and ten milliseconds. The event was later transferred from a PDP11 buffer to a 6250 bpi magnetic tape.

Many of the discriminated signals from various scintillation counters were connected to scalers. The scalers, which were installed in one of the five CAMAC crates in the experiment control room, were divided into two sets. One set, referred to as the "livetime scalers," was inhibited from counting by the signal DT+$\overline{\text{BEAMGATE}}$. The other set, referred to as the "beamgated scalers," was inhibited by $\overline{\text{BEAMGATE}}$. At the end of each beam spill, a computer interrupt was issued by the Bison Box. This interrupt, referred to as a

"B interrupt," caused the contents of the scalers to be transferred through the PDP11 to the magnetic tape. This scaler information is referred to as an end-of-spill scaler record. The scalers provide a permanent record of the number of incident beam particles per spill, as well as other monitors. Various additional test pulse interrupts were occasionally generated between spills, and the resultant information was transferred to magnetic tape.

When RTMULTI was not occupied handling the real time data acquisition duties described above, the program monitored the quality of the data being accumulated. After being written to tape, some events were selected for analysis. Due to the severe memory limitations of the PDP11/45, the data monitoring was limited. Nevertheless, the monitoring was extremely useful. RTMULTI allowed the experimenters to display representations of the events on the Tektronics display scope, as well as accumulate the position distribution of hits in the various detectors. Since the hodoscope elements were latched, the recorded latch signals were also checked to verify that they were consistent with the fast logic requirements of the event trigger. The integrity of the data was also monitored by checking the order of the individual hits recorded by the fast and slow amp PWC electronics, to see that it was consistent with expectations based upon the hardware. This check was quite useful in isolating problems in the PWC readout, the CAMAC dataway, and the CAMAC highway. The contents of the end-of-spill scaler records were also checked for internal consistency, such as a verification that the

livetime scalers were less than or equal to the corresponding beamgated scalers. If any of these checks detected an inconsistency, a message was directed to the ADM terminal in the experiment control room in order to alert the experimenters to potential problems.

The E515 spectrometer was employed to collect data during 1980, 1981, and 1982. The vast majority of the prompt muon triggered data was accumulated during the 1981 data run. Including diagnostic and other special triggers, a total of 2.3×10^6 events were recorded on magnetic tape during the 1981 data run. An average of 930 PDP11 words were written to tape for each individual event. The collected data was recorded on about 110 magnetic tapes.

CHAPTER 3

EVENT RECONSTRUCTION

For each event, the data accumulated on magnetic tape by the apparatus described in the previous chapter contains the encoded information gathered by the various detectors in the spectrometer. This information includes data words indicating which sense wires in the PWC's and DC's had hits, as well as which hodoscope elements were latched. The quantities of more direct interest in the charm search are the kinematic variables that describe the paths of the particles through the spectrometer, such as the slopes and intercepts of particle trajectories and their associated momenta. This chapter describes the process of identifying patterns among the signals from the various detectors, thus finding the tracks left in the spectrometer by the passage of charged particles, so as to measure their kinematic variables.

The data processing described in this chapter occurred in distinct stages. After some preliminaries, such as alignment and calibration of elements of the spectrometer, the trigger arm data was processed in a search for tracks which marked the passage of muons through the trigger arm. Those events that had at least one trigger arm track were then subjected to a search for forward arm tracks. The final stage of data reduction was the generation of a set of data summary tapes (DST's), which contained a summary of the trigger arm and forward arm tracks and their associated kinematic variables for the selected events.

This data reduction and the analysis was performed off-line, primarily on the Fermilab Computing Department's CYBER 175 computer system, using Fortran IV computer code written explicitly for the analysis of this data, as well as some library routines such as HBOOK, HPLOT, and MINUIT [84].

3.1 PRELIMINARIES

In order to employ the spectrometer data recorded on magnetic tape to reconstruct the interactions in the individual events, computer code was written to interpret the raw data and convert its encoded information into coordinates or other appropriate quantities. The output of devices such as the LAC and the Cherenkov counter required calibration studies in order to be interpreted. The relative

locations of all the detector elements in the spectrometer also needed to be established in order to employ the recorded data effectively.

Prior to the data run, the chambers (PWC's and DC's) in the spectrometer were carefully measured and positioned by Fermilab alignment crews in an attempt to set the chambers perpendicular to the Z axis of the spectrometer, and to get the X and Y chambers properly oriented. At the end of the data run, the locations of all elements in the spectrometer were surveyed.

The results of the end-run survey were employed to generate an initial specification file for the conversion of hit wire numbers into spatial coordinates. Using the initial specification file, a track finding program, and the recorded data, the locations of the chambers were adjusted to minimize the difference between the predictions for the locations of hits in a given chamber based upon tracks found using all other chambers versus the hit locations observed in that given chamber. This iterative procedure was employed to adjust the X and Y positions of the X and Y chambers. The Z locations of the chambers determined from the end-run survey were found to be adequate. The X and Y PWC's were treated throughout this analysis as if they had perfect XY angle alignment. (The forward arm PWC's were all within 1.4 mrad of the proper orientation in the XY plane.) The rotation angles and the positions of the rotated chambers were adjusted in a similar manner. As a result of this alignment process, most of the chambers were shifted by less than one half of a wire spacing from the values determined from the end-run survey. The alignment was checked

for several runs.

Once the alignment of the chambers was established, their efficiency was estimated by employing all chambers except the one whose efficiency was being measured to find tracks in the data, and then using those tracks to predict the location of hits in the chamber of interest. The frequency with which a hit was found within an appropriate search window in the chamber of interest is a measure of the efficiency of that chamber. The efficiencies of the various chambers as a function of position are shown in figures 16 and 17. Due to the relatively small number of chambers available in the upstream system, the beam chamber efficiency measurements may not be exceptionally reliable. The forward arm PWC efficiencies dip down in the central region where the fast amps were deployed. The DC's exhibit a dip in efficiency in the vicinity of the non-interacting beam.

For each run, the data from the chambers was studied to determine which wires had hits in an unusually large fraction of the events. A list of such wires, referred to as "hot-wires," was tabulated for each run. These wires were excluded from contributing entries to the list of coordinates presented to the track finding programs. There were typically 15 hot-wires detected in an individual run, and many of the same channels remained hot throughout most of the 1981 data run. The removal of the hot-wires from the beam chambers was significant as it reduced the confusion in the determination of the interaction vertex location.

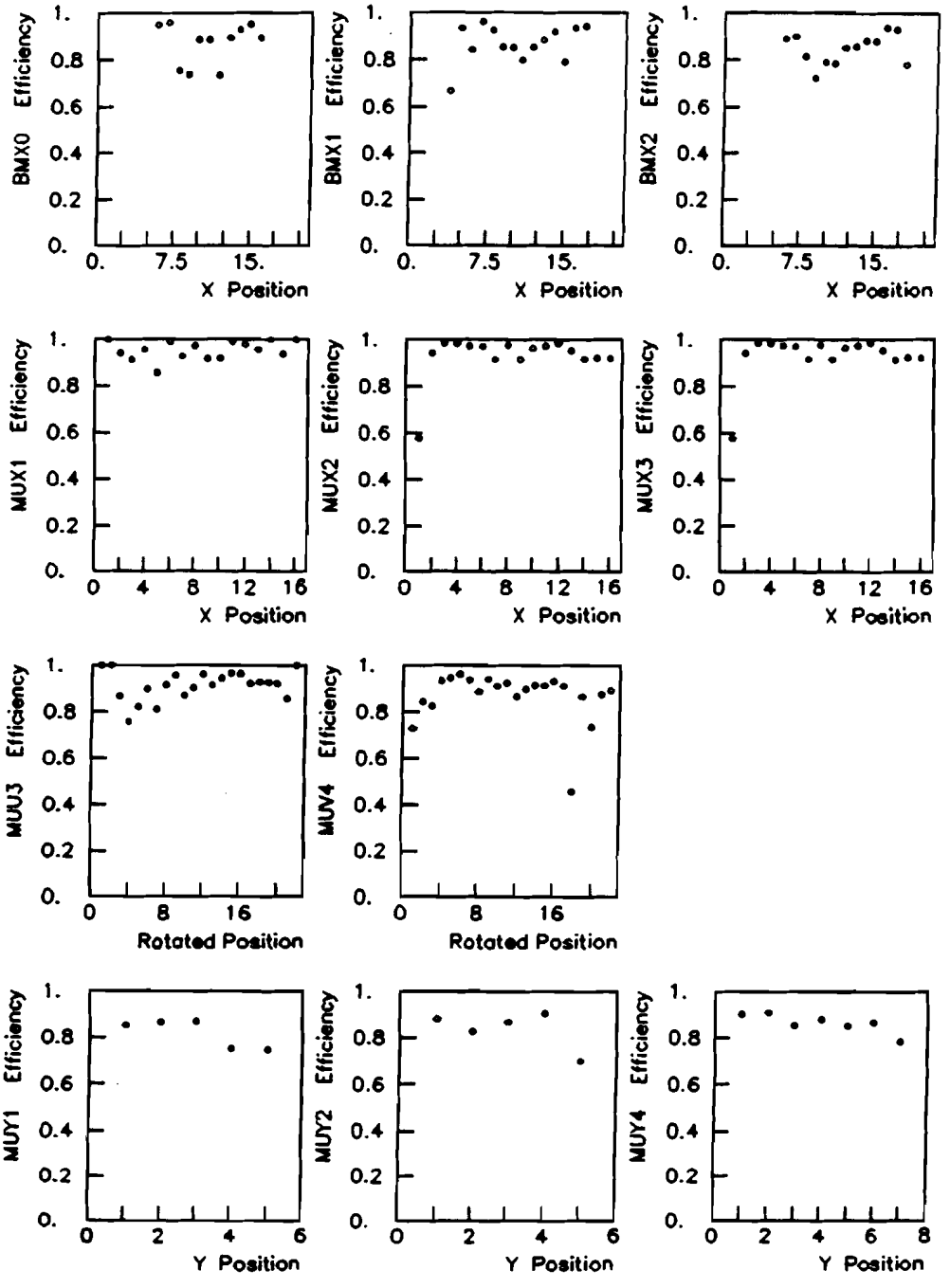

FIGURE 16. Efficiency of the beam system PWC's and the trigger arm PWC's as a function of position. (The active area of each PWC is divided into slices, and the efficiency is presented for each slice. Slice 1 corresponds to the most negative coordinates measured by the chamber.)

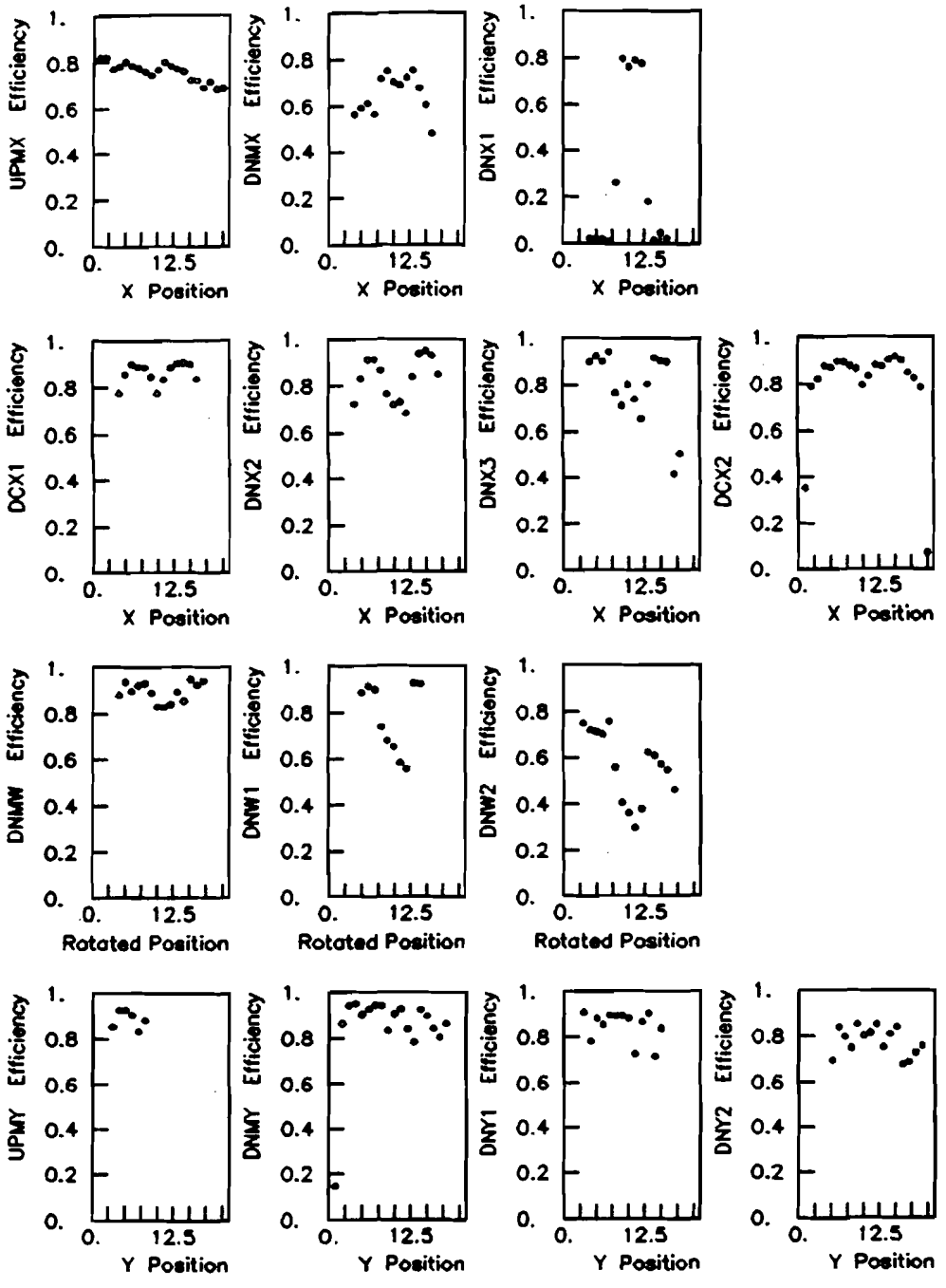

FIGURE 17. Efficiency of the forward arm chambers as a function of position. (The active area of each chamber is divided into slices, and the efficiency is presented for each slice. Slice 1 corresponds to the most negative coordinates measured by the chamber.)

3.2 MUON PASS -- TRIGGER ARM TRACKING

The encoded data from the trigger arm PWC's was decoded and its integrity was verified [85]. The data was then converted into coordinates. If hits occurred on adjacent channels in a trigger arm PWC, only one coordinate was generated for each adjacent pair. The mean number of trigger arm PWC hits was 16.7 per clean vertex DST event. (A clean vertex DST event is an event written on the DST that satisfied the clean vertex requirements described in the fifth chapter.)

Particle trajectories downstream of the magnet were assumed to be straight lines. Tracks were found by searching for straight line segments in the XZ and YZ views. Downstream straight line XZ track segments determined by the hits in the three trigger arm X PWC's were searched for as follows. Every combination of a hit in MUX1 and a hit in MUX3 formed a candidate segment. If the XZ slope and intercept determined by those two hits was consonant with a trajectory coming from the upstream end of the spectrometer, it was considered a segment. This segment was employed to predict the location of a hit in the intervening X chamber, MUX2. If a hit was found in MUX2 within ±1.2 cm of the predicted location, that hit was considered to be a member of the segment, and the three hits were employed in a least squares fit to determine the best slope and intercept for that segment. All three hits contributed equally to the fit. A very loose chi-squared (χ^2) cut was imposed, and if the three hit segment failed

this cut, the hit that was most distant from the fit track was rejected, and the tracks parameters were determined again. In addition, every combination of a hit from MUX1 and a hit from MUX2 that was not a subset of a track segment already found was considered a candidate segment. If the candidate segment was consonant with a trajectory coming from the upstream end of the spectrometer, it was a segment. Similar combinations in MUX2 and MUX3 were formed. The result of the downstream trigger arm XZ segment finding was a list of all segments defined by two or three hits from among the three X PWC's which satisfied the straight line hypothesis within errors and which were consistent with trajectories originating at the upstream end of the spectrometer. This loose definition of an XZ segment resulted in an average of 4.9 XZ segments per clean vertex DST event.

The same straight line segment finding procedure was employed in the YZ view using the three Y trigger arm PWC's. However, since MUY4 was separated from MUY1 and MUY2 by 0.4 m of steel, the search window for a third hit on a YZ segment was set at ±1.5 cm. The mean number of YZ segments was 3.4 per clean vertex DST event.

Three dimensional tracks downstream of the magnet were formed by employing every pair of XZ and YZ segments to predict the location of hits in the two rotated view PWC's. If a hit was found in either or both of the rotated PWC's within a search window of ±4.0 cm, then the XZ and YZ segments formed a downstream trigger arm track. The mean number of downstream trigger arm tracks was 2.4 per clean vertex DST event.

The M1 hodoscope latches were also unpacked and converted into X and Y coordinates. Since M1 was divided into left and right halves, only pairs of X and Y hits from the same half of M1 formed "valid M1 points." (Note that the prompt muon trigger logic effectively required that every event have at least one valid M1 point.) The mean number of valid M1 points was 2.5 per clean vertex DST event. Upstream tracks were defined as straight lines from target center through valid M1 points.

Every upstream track was extrapolated to the 40D48 magnet midplane, as was every downstream track, and the upstream and downstream track combination that had the smallest position deviation at the magnet midplane was interpreted as the proper upstream downstream pair. This matchup technique allowed the same upstream track to be matched with more than one downstream track. The charge of the particle associated with this trajectory was determined from the sign of the trajectory's bend in the XZ view. The momentum of the particle was determined from the magnitude of the bend incurred in traversing the magnetic field, using a simple bend approximation followed by an energy loss correction.

The trigger arm tracking was only performed on those events that had a latch bit set which indicated that those events were associated with prompt muon triggers. For each such event, the hodoscope latches were checked to verify that the latched hodoscope element configuration was consistent with the fast electronics requirements of the prompt muon trigger. The event was written to a so called "muon

pass" output tape and considered a candidate for further processing if its hodoscope latches were proper and it satisfied any of the following additional requirements:

1. The event contained at least one downstream trigger arm track.

2. The event contained at least one downstream XZ segment that extrapolated through M2 and M3 hodoscope elements which detected signals, and the event also had at least one hit in any of the rotated PWC's.

3. The event contained at least one downstream XZ segment that extrapolated through M2 and M3 hodoscope elements which detected signals, and the event also had at least one downstream YZ segment.

About 28 percent of the prompt muon triggered events had no reconstructed downstream trigger arm segments in either view. Approximately 15 percent of the events had at least one downstream XZ segment, but failed to meet the M2 M3 extrapolation requirements, and had no downstream YZ segment. Another 5 percent had at least one downstream YZ segment and no XZ segment. Approximately 51 percent of the prompt muon triggered events were written to the muon pass output tapes. About 42 percent of the prompt muon triggered events had at least one downstream trigger arm track.

3.3 HADRON PASS -- FORWARD ARM TRACKING

In order to perform the track finding in the forward arm, the PWC and DC encoded data was decoded into coordinates. For the PWC's, this process was complicated due to the presence of the three different types of electronics and because the 1 mm PWC's had electronic readouts on two sides of the PWC's. The order in which individual hits should appear in the raw data was determined by the hardware, and the unpacking software was written so as to verify consistency between hardware expectations and the data recorded on magnetic tape. About 0.15 percent of the prompt muon triggered events contained data that was inconsistent with the hardware expectations, and those events were rejected. Recall that the DC reported both a wire hit and an associated time, and this resulted in two coordinates for each DC hit, one on either side of the reported sense wire.

3.3.1 Downstream Forward Arm XZ Segments

Particle trajectories downstream of the 40D48 magnet were assumed to be straight lines. The straight line XZ segment finding in the forward arm employed all six downstream forward arm X chambers. As a compromise between the desire to limit the number of accidental tracks due to the large number of hits in the forward arm, and the desire to reconstruct as many of the real trajectories as possible in spite of

chamber inefficiencies, a minimum of four hits out of the six chambers were required to define an XZ segment.

The straight line XZ segment finding in the forward arm proceeded as follows. All combinations of a hit from one of the first three chambers, and a hit from one of the last three chambers were investigated as endpoints of a candidate segment (starting from the outermost chambers, DNMX and DCX2, and working inward). There had to be at least two X chambers between the chambers containing the endpoints, or the candidate segment could not satisfy the minimum hit requirement, and was thus immediately rejected. The candidate segment was rejected if both its endpoints were already a subset of another segment, or if the segment was not consonant with a trajectory passing through the magnet aperture. Assuming the endpoints were not rejected, a straight line connecting those two endpoints was interpolated to the intervening chambers. Hits in every intervening X chamber were checked to see whether any were within ±3 mm of the interpolated location at that chamber. If a hit was within that search window, it was added to the list of hits associated with this candidate segment. After all the intervening X chambers had been searched, if the candidate segment had less than four hits, it was rejected and the next set of endpoints was investigated. However, if the candidate segment had four or more hits, and this combination of hits was not a subset of another segment already found, then the hits were fit to a straight line via a least squares fit. (The weights employed in the fit for the various PWC's were each within 50 percent

of the values anticipated from the wire spacing alone. The drift chamber hits were assigned relatively small weights, corresponding to an RMS resolution of 0.75 mm because the final calibrations and offsets for the TDC's were not available at the time the tracking was performed.) If the least squares fit of the hits from the candidate segment had a chi-squared per degree of freedom (χ^2/DOF) greater than 10.0, the segment was rejected. If the χ^2/DOF was between 2.5 and 10.0, and the candidate segment had more than the minimum number of hits, then the hit that was most distant from the straight line was deleted and the segment was refit with the χ^2/DOF tests repeated. If the χ^2/DOF was between 2.5 and 10.0, and the candidate segment had the minimum number of hits, it was rejected. The remaining candidate segment, which had a χ^2/DOF of less than 2.5, was then compared to the segments already found, and if the candidate had more than one hit in common with a segment already found, then whichever of the two segments had fewer hits was rejected. If both had the same number of hits, the segment with the larger χ^2 was rejected, while the other was retained. This whole process was repeated using the next set of endpoints, until all possibilities were checked.

After all the XZ segments were found by the above process, they were passed through a filter that made additional checks for segments that had too many hits in common, or depended upon both partners of a DC coordinate doublet, and eliminated the segments that were considered indistinct. The mean number of forward arm XZ segments found was 6.7 per clean vertex DST event.

3.3.2 Forward Arm YZ Segments and XZ YZ Segment Matchups

It would have been convenient to perform straight line YZ segment finding downstream of the magnet. However, due to chamber inefficiencies it was undesirable to require two or more hits in the three Y chambers downstream of the spectrometer magnet. As a result, a scheme was devised which searched for tracks in the YZ view using the Y chambers upstream and downstream of the magnet simultaneously.

Since the 40D48's field was primarily in the -Y direction, the XZ view was the primary bend plane. Thus, the trajectory of a charged particle in the XZ view was approximately a straight line upstream of the magnetic field, followed by an arc of a circle inside the magnet field, and then another straight line downstream of the field. The XZ view trajectory was therefore specified by the downstream XZ segment and a single XZ point upstream. Meanwhile, the trajectory in the YZ view was approximately a straight line, and the validity of that approximation improved as the particle's momentum increased. (Figure 18 shows a scatterplot of the difference in the upstream and downstream YZ angles of simulated tracks versus the momenta of those tracks.) The deviation of the trajectory from a straight line in the YZ view is attributed to two sources. The first source of deviation will be referred to as "geometric bending." Note that the tangent of the YZ view angle is given by the ratio of the particle's Y component of momentum (p_Y) to its Z component (p_Z). In a square magnetic field with the the field along the Y direction, p_Y is a constant of the

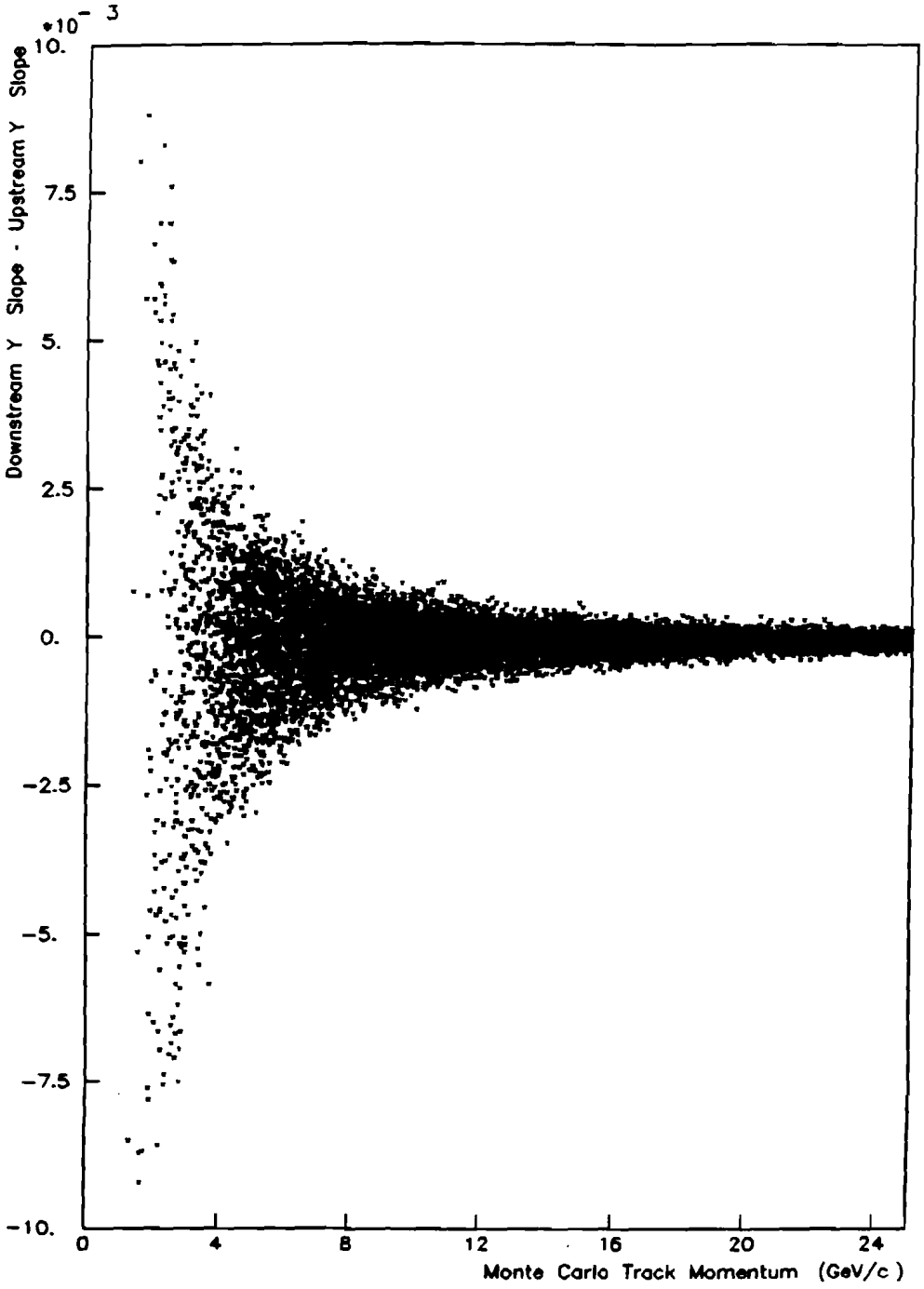

FIGURE 18. The difference between the upstream and downstream YZ slopes of simulated tracks accepted by the spectrometer as a function of the track momentum.

motion, however, p_Z varies as the charged particle moves along the helical path. Therefore, even in a square field, the YZ angle of a charged particle's trajectory changes, resulting in geometric bending. The second source of change in the YZ angle of a charged particle passing through the magnetic field is the Lorentz force exerted upon the particle by the fringe fields of the magnet. This effect is referred to as "vertical focusing."

A simple two parameter representation of the effects of geometric bending and vertical focusing was made based upon the following idealization of the magnetic field. The magnet was assumed to be symmetric with respect to the XY, XZ, and YZ planes passing through the magnet center. Furthermore, it was assumed that the X component of the magnetic field (B_X) was negligible, as was the X dependence of the magnetic field. The major component of the magnetic field, B_Y was represented by a square field of magnitude $|B_0|$ out to a transition region, where B_Y was assumed to fall rapidly and linearly to zero. The Z component of the magnetic field, B_Z, was zero everywhere except for the transition regions, where its value was determined by the requirement that the curl of the magnetic field be zero. Since the transition regions were assumed to have small extent, their effects were modeled as two thin lenses.

Using the above model of the magnetic field, the change in p_Y experienced by a particle passing through the upstream transition region was given by the expression

$$\Delta p_Y = -q\, B_0\, y\, p_X / p_Z$$

where q was the charge of the particle, and y was the elevation of the particle above magnet center at the transition region. Upon exiting the magnetic field, p_Y experienced another impulse whose magnitude was given by the same expression, but the sign of that impulse was switched. The effects of the fringe fields upon p_X and p_Z were assumed to be negligible. The effect of geometric bending in the YZ view was straightforward to express in the terms of the upstream and downstream XZ angles and the component of momentum in the XZ plane. This simple model allowed an algebraic connection between the upstream and the downstream YZ segments which included a first order correction for the effects of geometric bending and vertical focusing, and employed two parameters, the magnitude of the square field, $|B_0|$, and the distance between the transition regions.

Using the above approximations, the downstream YZ slope (m_D) and the downstream YZ intercept (b_D) of any trajectory was expressed as a linear function of the upstream YZ slope (m_U) and YZ intercept (b_U)

$$m_D = K\, m_U + L\, b_U$$

$$b_D = M\, m_U + N\, b_U$$

where the "constants," K, L, M, and N, depended only upon the XZ trajectory of the particle, the particle's XZ momentum, and upon the magnitude and length of the magnetic field. If the interaction vertex location was known, and had Y location given by Y_{VTX} and Z location given by Z_{VTX}, then using the above model, a hit in any of the downstream Y chambers with Y coordinate given by y_i at Z location z_j could be employed to predict an upstream YZ slope from the following

relation

$$m_U = \frac{y_i - Y_{VTX} (L z_j + N)}{K z_j + M - Z_{VTX} (L z_j + N)}$$

as long as the denominator was nonzero. As it turns out, the target was not near the focus of this thin lens system, so the denominator was indeed nonzero. Thus, for every XZ segment, all the Y chamber hits were mapped into predictions for upstream YZ slopes originating at the interaction vertex. A cluster of hits predicting approximately the same upstream YZ slope was then interpreted as evidence of a charged particle trajectory.

In order to find the YZ segments emanating from the interaction vertex, the model described above was employed as follows. After the downstream XZ segments were found, an interaction vertex position was selected based upon beam chamber information. (Further details on the vertex selection are included in the section of this chapter on the generation of the DST.) The momentum of each forward arm "track" was estimated from the vertex location and the downstream XZ segment parameters assuming the YZ trajectories had zero slope and that the segments passed through the target. The momentum was estimated with a polynomial called PTRAK, which was generated by fitting the parameters of a set of simulated tracks that had been propagated through an early version of the magnetic field map [86]. When combined with the interaction vertex location, each hit in UPMY was mapped to an upstream YZ slope. For each downstream XZ segment, all downstream Y

chamber hits were mapped to upstream YZ slopes using the model sketched above. When the difference in the upstream YZ slopes predicted by hits in any two Y chambers was less than ±0.005, that pair of hits was considered a candidate cluster. After all chambers were searched for additional members of this cluster, a least squares fit to the model was performed to determine the best values for the parameters of the candidate YZ segment. The candidate downstream YZ segment and the downstream XZ segment were combined to predict the expected location of the hits in the rotated chambers. A hit in a rotated chamber was considered to participate in the track if it was within ±3.5 cm of the predicted location. To qualify as a valid XZ and YZ segment matchup, the pair was required to have at least one participating rotated hit, and the weighted mean deviation between the predicted rotated hit locations and the participating hits had to satisfy stricter requirements.

For each XZ segment, all possible YZ clusters were generated by the above technique, and the YZ segment that had the largest number of participating rotated hits was considered the best matchup for that XZ segment. If more than one YZ segment yielded the same number of participating rotated hits when combined with a given XZ segment, then the YZ segment that had the most Y hits was selected as the partner for that XZ segment, yielding a three dimensional forward arm track. Since this scheme assumed all tracks originated at the interaction vertex, it tended to lose or poorly reconstruct tracks which originated elsewhere, such as tracks from neutral kaon or lambda

decays. The mean number of forward arm tracks found by the above procedure was 6.2 per clean vertex DST event.

3.3.3 Hadron Pass Output Tapes

The muon pass output tapes served as the input tapes for the forward arm tracking stage of data reduction. The output of this "hadron pass" was a series of magnetic tapes which contained the raw data for each selected event, as well as the results of both the trigger arm and forward arm tracking. Only those events that had at least one downstream trigger arm track were processed by this forward arm tracking pass. This requirement rejected about nine percent of the prompt muon triggered events, and thus the hadron pass output tapes contain about 42 percent of the prompt muon triggered events.

3.4 DATA SUMMARY TAPES

The generation of the data summary tapes (DST's) was performed by computer code which redetermined the interaction vertex location, performed additional trigger arm analysis, recalculated the forward arm track momenta, and processed the Cherenkov and forward arm muon identifier data. The input tapes for the generation of the DST's were the output tapes of the hadron pass.

3.4.1 Interaction Vertex Location

This subsection describes how the location of the interaction in the target was determined. The momentum resolution of the forward arm is critically dependent upon the proper determination of the interaction vertex location.

The Y location of the interaction vertex, Y_{VTX}, was assumed to be the center of the target. (Recall that the Y location of the recorded interacting beam particles at the Z position of the target was constrained by the 1.5 mm overlap of the counters B1 and B2.) The Z location of the interaction (Z_{VTX}) was assumed to be the center of the 3 cm long target. The X location of the interaction vertex was determined from the hits in the various PWC's. A strong correlation between the X position of a beam particle at Z_{VTX} (X_C) and the incident slope of that beam particle (s) was anticipated due to the beamline optics. This correlation is illustrated in the scatterplot shown in figure 19, which was extracted from pre-scaled beam triggered data. (Straight line tracks were found in the four X PWC's upstream of the magnet by employing the straight line segment finding program described previously.) The correlation was parametrized as

$$s = a\, X_C + b$$

and a least squares fit yielded the values $a=0.0469\ m^{-1}$ and $b=-0.00014$. This correlation was employed to map every hit in each beam chamber into a prediction for X_C. Let x_i be the X location of a hit in the beam chamber at Z location z_j, then since

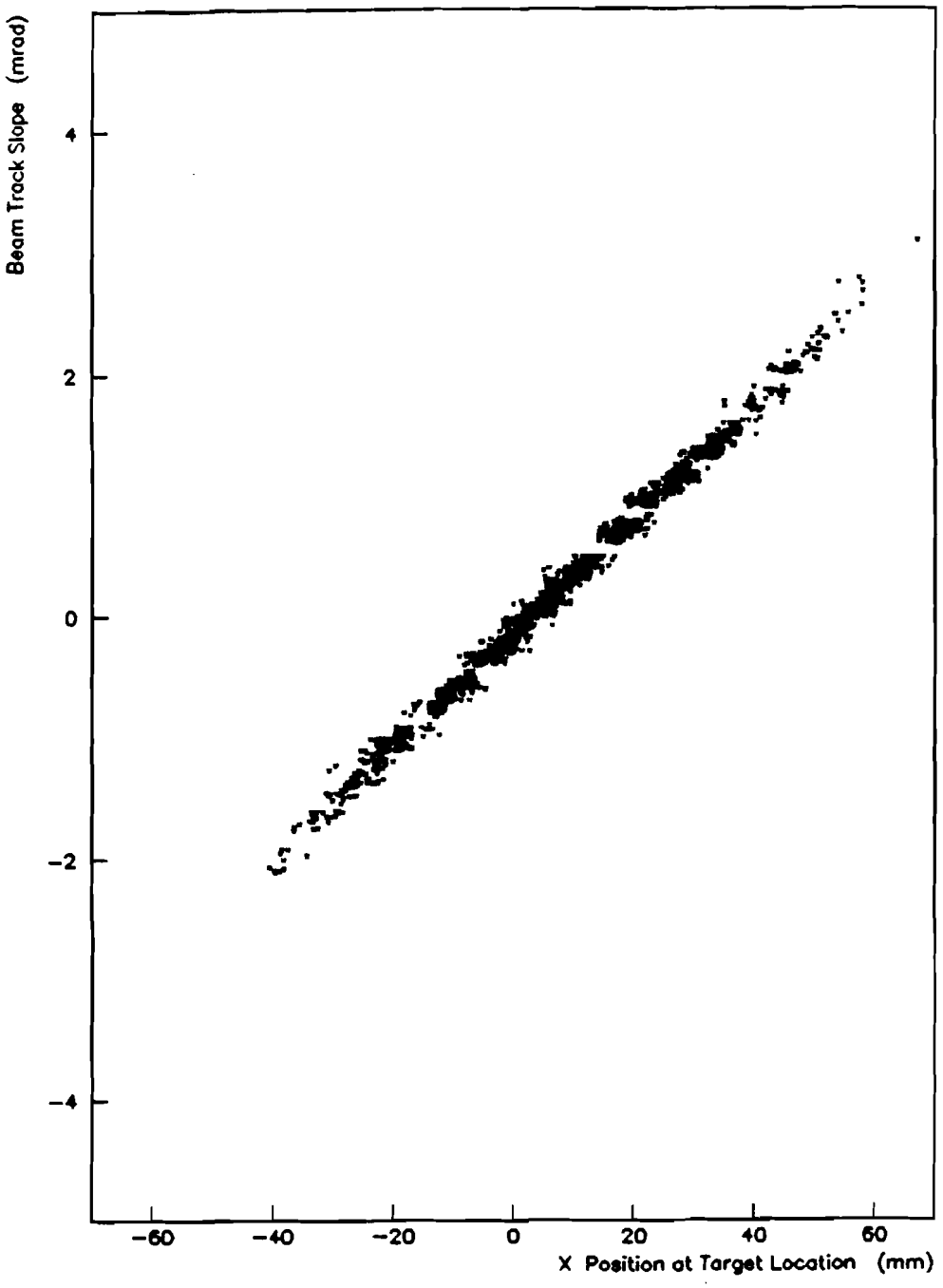

FIGURE 19. Upstream slope of incident non-interacting beam tracks versus the X position of the non-interacting beam at the Z position of the target. The data presented in this plot were gathered with the pre-scaled beam trigger.

$$s = a\,X_C + b = (X_C - x_i) / (Z_{VTX} - z_j)$$

the corresponding prediction for X_C is given by the expression

$$X_C = [\, x_i + b\,(Z_{VTX} - z_j)\,] / [\, 1 - a\,(Z_{VTX} - z_j)\,].$$

Taking into account the uncertainty in the projection, all clusters of X_C predictions that were within an appropriate search window were found. The weighted mean of the X_C values of the members of the cluster was considered as a candidate location for the X position of the interaction vertex.

Because there was frequently more than one such cluster per event, a technique was devised to select the "best" cluster and use it to determine the X location of the interaction vertex, X_{VTX}. If a cluster corresponded to a mean X_C outside B1 and B2, the cluster was immediately rejected. If a cluster could have been generated by electronic cross talk, and there was an associated stronger cluster, the cross talk cluster with fewer hits was rejected. Since a cluster could also arise from a non-interacting beam track in time with a triggering interaction, all clusters were projected downstream into the X PWC's taking into account the 3.9 mrad bend anticipated for a 205 GeV/c beam particle traversing the magnetic field. The number of X PWC's with a hit within an appropriate search window was counted. If a cluster had four or five out of a possible five of these "beam tags," then the cluster was rejected. The DC's were not employed as non-interacting beam tagging chambers because no evidence of the non-interacting beam could be found in the DC's, probably as a result of the rate limitations of their electronics. About

3.2 percent of the clusters were rejected by this non-interacting beam tag test. The vertex clusters rejected by the B1 B2 check, the cross talk check, or the non-interacting beam check, are referred to as "blemished vertex clusters," and the surviving clusters are said to be "unblemished."

The chamber UPMX was employed to distinguish between the unblemished vertex cluster as follows. Since an upstream point and a downstream track determine a trajectory through the magnetic field, they can be combined to predict the location at which that trajectory would pass through the chamber UPMX. (This prediction was made for each cluster via a polynomial which is described in the subsection on the forward arm momentum analysis.) A "UPMX matchup" occurred if a hit was found in UPMX within ±1.6 mm of the predicted location. Every downstream forward arm track in the event was employed in this manner, and the total number of UPMX matchups associated with each vertex cluster was calculated. The vertex cluster associated with the largest number of UPMX matchups is believed to be the cluster most likely to be due to the beam track responsible for the interaction. This assertion is supported by studies in which simulated cluster locations selected at random were injected into events that had a single vertex cluster. That data vertex cluster had a different number of UPMX matchups than the simulated cluster in 82 percent of the cases tested. When the difference in the number of UPMX matchups was one, the data cluster had more UPMX matchups in 81 percent of the cases. When the difference was two, the data cluster had more UPMX

matchups in 95 percent of the cases, and when the difference was three or more, the data cluster had more UPMX matchups in 99 percent of the cases.

The unblemished vertex clusters were split into two classes. One class contained those vertex clusters that employed hits from two or three beam chambers while the other class contained those vertex clusters that only employed hits from a single beam chamber. The best cluster from each class was defined to be the cluster with the largest number of UPMX matchups. Whenever that criterion failed to be decisive, the best cluster within that class was the one with the fewest number of non-interacting beam tags (among the group with the maximum number of UPMX matchups). If that criterion also failed to be decisive, other less reliable tests based upon the relative importance of beam tags from various chambers, and the proximity of the cluster to the center of the vertex position distribution were invoked. The best vertex cluster from each class were compared, and the cluster with the largest number of UPMX matchups was selected as the cluster employed to determine the X position of the interaction vertex, X_{VTX}. If the best cluster of each class had the same number of UPMX matchups, then the entry from the multi-chamber class was selected.

It should be pointed out that whenever there was more than one unblemished vertex cluster in an event, this vertex selection technique clearly depended upon the forward arm tracks, but the forward arm tracks were weakly dependent upon the vertex location due to the model employed in the YZ tracking. This situation presents a

problem which is not readily resolved. Due to minor errors in the vertex code employed in the hadron pass, and some later improvements in the selection criteria, the vertex selected prior to the YZ tracking was nearly the same as that selected by the final DST analysis in only 68 percent of the events that survived the clean vertex cut described in the fifth chapter. (The hadron pass vertex code employed the same clustering technique just described but different cluster selection criteria and it assumed zero slope YZ tracks.)

3.4.2 Trigger Arm Track Refinements

Once the interaction vertex location X_{VTX} was determined, the choice of the upstream trigger arm track associated with each downstream trigger arm track was re-evaluated using the magnet midplane deviation technique described previously, but this time employing the proper X_{VTX} rather than target center. The charge of the trigger arm track was re-determined, and a square field estimate of the track's momentum was made. The momentum was then refined by an iterative fit which propagated the downstream track through the magnet yoke, adding energy and taking into account multiple scattering, and minimizing the deviations between the track's position and the selected M1 point and interaction vertex locations. The quality of the trigger arm tracks were also tagged for later selection.

3.4.3 Forward Arm Momentum Analysis

The charge and momentum of the forward arm tracks were re-evaluated using the vertex location selected for the DST. Polynomials were employed in the evaluation of the charge and momentum of the vast majority of the tracks.

One polynomial employed was a Tchebycheff expansion of the inverse of the magnitude of the momentum times the charge, in terms of four variables that determined the particle trajectories, assuming Y_{VTX} and Z_{VTX} were constants for all interactions. The four variables selected were X_{VTX}, the downstream XZ slope and XZ intercept of the track, and the Y position of the track at DNY1. To determine the coefficients of the polynomial expansion, simulated tracks whose parameters corresponded to the orthogonal set of Tchebycheff points in the selected variables were found by an iterative procedure of propagating tracks through the 40D48 magnetic field map. The propagation of the tracks was performed by integrating the Lorentz equations of motion of a charged particle in the measured magnetic field. The numerical integration was performed by a fourth order Runge-Kutta integrator [87]. The coefficients of the Tchebycheff expansion were then easily determined due to the orthogonality of the Tchebycheff polynomials over the selected tracks. Many terms were required in the polynomial expansion in order to achieve the desired accuracy, but the polynomial was easy to generate. Due to the correlation between the domains of the variables and the number of

terms required in the polynomial expansion to maintain the desired accuracy, limits on the domains were selected which excluded about two percent of the tracks. (This polynomial technique is a variation on an idea described by Lechanoine, Martin, and Wind [88].)

In the same manner, an additional Tchebycheff polynomial expansion was generated to parametrize the upstream XZ slope as a function of the same four variables. This second polynomial provided XZ opening angles and facilitated the prediction of hit locations in UPMX.

For those forward arm tracks outside the domain of the Tchebycheff polynomials, the charges were determined by the bend angles, the momenta and upstream XZ angles were determined by iterative propagation of the downstream tracks through the magnetic field to the vertex with the magnitude of the momentum as the only free parameter in the iteration. The iteration was discontinued when the propagated track passed within ±0.04 mm of the X vertex location, or when convergence was not achieved after five iterations. The simpler but less accurate polynomial PTRAK was used to estimate the momenta of those tracks for which the iterative approach failed to converge.

3.4.4 Forward Arm Particle Identification Analysis

The particle identification analysis performed while generating the DST made use of the forward arm muon identifier and the Cherenkov counter. The information gathered by the LAC was not retained on this DST.

The forward arm tracks were extrapolated to the M4 and M5 hodoscopes, and a search was made for matchups between M4 and M5 hits and the extrapolated track, allowing for multiple scattering. Those tracks that had a matchup were tagged as potential forward arm muons.

The data from the threshold Cherenkov counter was employed together with the charged tracks to calculate the value of a variable called PROBK for each track. (In spite of its unfortunate name, PROBK is not a probability.) For each track, PROBK represents how well the Cherenkov information associated with this event matched the hypothesis that the track was generated by a kaon relative to how well it matched either the kaon or the pion hypothesis for that track's identity. The range of PROBK values is from zero to one with higher PROBK values implying a greater likelihood that the track was indeed generated by a kaon.

The calculation of PROBK is described below (more details may be found elsewhere [89]). First, the pedestals were subtracted from the pulse heights recorded by each Cherenkov ADC. Then if the corrected pulse height was above a threshold, called CLEVEL, the pulse height was converted into the appropriate number of photoelectrons. If the

pulse height was below this CLEVEL, the signal from that photomultiplier tube was assigned zero photoelectrons. All charged tracks were extrapolated to their intersection with the Cherenkov counter mirror surface and reflected to the photomultiplier tube mirror cone faces. The expected fractions of light deposited in the various photomultiplier tubes were calculated based upon both the pion and kaon hypotheses for each track's particle identity. A track was judged to be capable of producing detectable light in a photomultiplier tube if more than CLEVEL ADC counts were expected in that photomultiplier tube under the pion hypothesis.

Using the pion hypothesis for each track's identity, the tracks were sorted into "groups." For any track, if the predicted light distribution populated photomultiplier tubes that were not populated by any other track in the event, then that track was said to be isolated, or a member of a group of one. If the Cherenkov light cone of one other track in the event intersected a photomultiplier tube in common with the first track, then those two tracks formed a group of two. Larger groups were formed in a similar manner. Any member of a group was only required to share one photomultiplier tube in common with some other member of the group. Of the forward arm tracks with momenta between 7 and 20 GeV/c that intersected the active area of the Cherenkov counter, 70 percent were isolated, while 22 percent were members of groups of two, and the remaining 8 percent were members of groups that contained three or more tracks. (About 96.6 percent of all forward arm tracks whose momenta were between 7 and 20 GeV/c

intersected the Cherenkov counter within its active area.)

The variable PROBK was set to zero for all tracks whose momenta were below the pion threshold for generating Cherenkov radiation. Those tracks that did not properly intersect the active area of the Cherenkov counter were also assigned a PROBK of zero. For each of the remaining tracks, the sum of the likelihoods of all pion and kaon hypotheses for the particle identities for the members of the group which included that track and which identified that track as a kaon was calculated. Additionally, the sum of the likelihoods of all possible kaon and pion hypotheses for the identity of that track based upon all particle identifications for the members of the group was calculated. The PROBK of that track was given by the ratio of the kaon likelihood sum over the sum of all likelihoods. About 0.03 percent of the tracks were members of groups that included five or more tracks, and all such tracks were assigned a PROBK value of zero.

The Cherenkov identification calculations described above were actually performed twice per track using two different values of CLEVEL. The lower CLEVEL was set at a value that corresponded to a signal of about 0.4 photoelectrons and resulted in a value called PROBK1. The higher CLEVEL was set at about 1.0 photoelectron and resulted in a value called PROBK2. The advantage of PROBK1 over PROBK2 is that due to the lower signal threshold employed in calculating PROBK1, PROBK1 identified pions with higher efficiency than PROBK2. The disadvantage of PROBK1 is that it also misidentified

kaons more frequently because it was more susceptible to noise.

3.4.5 DST Output Tapes

During the 1981 data run of this experiment, about 1 936 000 prompt muon triggers were recorded on magnetic tape. Approximately 129 000 prompt muon triggers were taken during the shakedown of the spectrometer, and were not processed during the muon pass. Several raw data tapes were found to be unreadable due to a problem with the magnetic tape drive. As a result, 25 000 prompt muon triggered events were forever lost. Additionally, 12 078 events had CAMAC error conditions, and were rejected. (The majority of the CAMAC errors occurred prior to run 1122, and were most likely due to an attempt to perform a DMA transfer beyond the allocated buffer limit due to large amounts of data in the LAC. This problem was relieved by altering the LAC DMA transfer instructions to allow the DMA transfer to be truncated when necessary.) About 1000 prompt muon triggers were never processed because they were spread among several small runs.

The first run that contributed to the DST was run number 1089, which was recorded on 1 May 1981. The last run employed was run 1292, recorded on 31 May 1981. Most of the runs between those dates contributed events to the DST. A few runs were omitted from the DST for various reasons. The block of runs from 1267 through 1281 involved a test of a different configuration of the spectrometer which

included a NaI(Tl) scintillating active target [90]. The active target data, as well as other special test and calibration runs were not represented on the DST. The runs that contributed to the DST were by no means flawless. During several of the runs, various detectors were briefly inoperative due to high voltage trips. Furthermore, in a few cases, the 40D48 magnet tripped off during a run. The forward arm PWC, DNY1, was inoperative during runs 1099 through 1125 due to a broken anode wire.

The output of the DST generation was a series of six magnetic tapes containing information on 748 529 prompt muon triggered events, from which invariant mass plots were constructed. The tapes included information on the trigger arm tracks, the forward arm tracks, the vertex location and quality, the Cherenkov identification, the hodoscope latches, and general information on the quality of the events and the individual tracks.

CHAPTER 4

SPECTROMETER SIMULATION

In an invariant mass plot search, the mass resolution of the spectrometer is of interest because the mass resolution combined with the natural width of a particle state determines the observed width of that state. The mass resolution of the spectrometer depends upon the geometry of the spectrometer, the position resolution of the individual detectors, the amount of scattering material in the spectrometer, and the magnetic field integral. Another important characteristic of the spectrometer employed in an invariant mass plot particle search is the acceptance, that is, the probability that a produced state was detected and reconstructed in the spectrometer. Combined with a knowledge of the incident beam flux, the target material, and the size of the observed signals, the acceptance allows one to report the production cross section of observed particle

states.

Both the resolution and the acceptance of the spectrometer for a given state can be estimated by the Monte Carlo method. The first section of this chapter describes the simulation techniques employed to generate simulated data and the analysis performed upon that simulated data. The second section summarizes the results of the Monte Carlo studies.

4.1 SIMULATION METHOD

A standard technique employed in the estimation of the acceptance of a spectrometer for a given state is to generate a large number of simulated states selected from a production distribution of interest, and then to determine the fraction of those states that would be detected by the spectrometer and reconstructed by the associated data analysis. The resolution of the spectrometer for a particular parameter can be estimated by comparing the generated value of that parameter to the value which results from the reconstruction of the simulated data. This section describes the production models employed in selecting the kinematic variables of the simulated states, followed by a description of the propagation of the simulated state through the spectrometer, so as to construct the simulated spectrometer data. Brief comments upon the analysis of this simulated data are also included.

4.1.1 Particle Generators

The generators simulated the production of charmed particles in the spectrometer. First an interaction vertex location was selected. The X location of the production vertex, X_{VTX}, was chosen from a distribution based upon a parametrization of the X distribution of the vertices observed in the data. The Y location of the production vertex was selected from a uniform distribution within ±0.75 mm of the target center location. The Z location of the production vertex was selected with a uniform distribution over the target length. In the XZ view, the direction of the incident beam particle was determined by the choice of X_{VTX} and the beam optics relation. In the YZ view, the incident beam particle direction was selected from a uniform distribution within ±2 mrad of zero slope. (This YZ beam slope distribution was selected based upon a study of the incident beam slopes observed in the pre-scaled beam triggered events.) The incident pion momentum was assumed to be 205 GeV/c. Next the charmed state was generated. Due to the extremely narrow width of the charmed particles that decay weakly, the intrinsic width of the charmed particles was neglected in this simulation for all models tested. Three different types of models were employed in the generation of charmed states.

One uncorrelated production model, referred to as model I, generated an individual charmed particle with a Feynman x (x_F) and transverse component of momentum (p_T) selected from the distribution

$$\frac{d\sigma}{dx_F\, dp_T^2} \propto (1 - |x_F|)^n \exp(-b\, p_T^2). \qquad \text{(Model I)}$$

Several values of the parameter n were tested. (Most of the recent fixed target experiments on the hadronic production of charm have employed this production model.)

Another uncorrelated production model, called model II, generated an individual charmed particle with x_F and p_T selected from the distribution

$$E\,\frac{d\sigma}{dx_F\, dp_T^2} \propto (1 - |x_F|)^n \exp(-b\, p_T^2) \qquad \text{(Model II)}$$

where E was the energy of the simulated charmed particle. (Since the "random numbers" employed in generating this distribution were selected via the rejection method, the p_T spectrum has a cutoff imposed at 3 GeV/c.)

The correlated production model, referred to as model III, generated a charmed anticharmed meson pair by selecting a mass for the pair (M), as well as an x_F and p_T according to the distribution

$$\frac{d\sigma}{dM\, dx_F\, dp_T^2} \propto \exp(-5M)\ (1 - |x_F|)^n \exp(-b\, p_T) \qquad \text{(Model III)}$$

and then the parent state decayed isotropically, at the production vertex location, into the charmed anticharmed meson pair. Note that this model yields a significantly softer x_F distribution for the individual charmed particles than the other models for the same value of n. (The "random numbers" employed in this model were also selected via the rejection method, so the p_T spectrum has a cutoff imposed at 5 GeV/c.)

With the kinematic properties of the simulated charmed state selected, the distance to the decay vertex for each charmed particle was randomly selected from an exponential distribution reflecting the measured lifetime of the state. The charmed state was linearly translated along the direction of its momentum vector to the decay vertex location. The location of the decay vertex was recorded, and the charmed state decayed isotropically via the mode under study in this simulation, generating simulated daughter particles at the decay vertex.

4.1.2 Trigger Arm Particle Propagator

Potential trigger muons from the simulated charmed particle decays were propagated in steps through the trigger arm until they exited. Most of the steps involved a straight line motion in both the XZ and YZ views, followed by a correction to both the XZ and YZ positions and angles to simulate the effects of multiple Coulomb scattering in the intervening material. The mean multiple scattering angles were determined via the Highland formula [91], and the correlation between the scattering angle and the displacement was taken into account [92]. An energy loss correction to account for the passage of the simulated particle through dense materials was also generally made, and was based upon a parametrization of muon energy loss data [93]. Propagation through the yoke of the 40D48 magnet was

performed via a fourth order Runge-Kutta integration of the Lorentz equations using a representation of the magnetic field in the yoke. The representation of the yoke's field was generated from magnetic field measurements taken inside the magnet aperture. This field map was only non-zero within the yoke. As a result, the calculated field within the yoke was scaled up by 1.22 to correct for the non-zero fringe field effects. The propagation through the magnet was performed in ten steps, and corrections for energy loss and multiple scattering were performed during each step.

The simulated muon had to intercept the active area of the trigger arm scintillation counters for the propagation to continue. The location at which each counter was intercepted was recorded. If the muon intercepted a PWC within its active area, the appropriate exact coordinate was recorded.

4.1.3 Forward Arm Particle Propagator

Simulated charged particles incident upon the forward arm were generally propagated in steps of straight lines, followed by multiple scattering corrections of the form described for the trigger arm particle propagator. Excluding the target, the forward arm spectrometer elements from the end of the target to the last DC represented about 0.05 radiation lengths. No energy loss corrections were made to the forward arm simulated tracks due to the relatively

small amount of material encountered by particles passing through the forward arm. In the regions where the 40D48 magnetic field was non-negligible, the particles were propagated through the field with a fourth order Runge-Kutta integrator for which the step size was 2.54 cm. When the tracks intercepted chambers within their active area, the appropriate exact coordinates were recorded. Charged pions and kaons were allowed to decay based upon their measured lifetimes and decay modes, and all charged decay products were propagated through the end of the chamber system.

4.1.4 Monte Carlo Output and Analysis

After all the daughter particles resulting from the decay of the simulated state were propagated through the spectrometer, the accumulated information on the simulated state and the exact coordinates of the intersection of the simulated daughter particles in the various detector elements were written to an output file. This output file served as input to an analysis program that employed much of the same analysis computer code described in the previous chapter. Note, however, that no raw data unpacking occurred because the simulated data already contained the exact hit location in coordinate form. To include the effects of chamber resolution, all hits from the PWC's could be shifted to the nearest sense wire. Additionally, each DC hit was converted into two hits, one on each side of the

appropriate sense wire, and the DC coordinate could be shifted randomly by a distance selected from a Gaussian distribution that had an appropriate width. The efficiency of the chambers could also be imposed by eliminating hits based upon the chamber efficiency maps determined from the data. The hodoscope hits were converted into latch coordinates. Hits were also generated in the beam chambers, and the beam chamber efficiency and resolution could be imposed.

The resulting simulated data was processed by the tracking programs that are described in the previous chapter. The data analysis cuts (described in the next chapter) were also enforced. The fraction of the reconstructed parent states, as well as the resolution in both mass and momentum were thus measured. No Cherenkov ADC simulation was performed in the Monte Carlo simulation, so the Cherenkov analysis code only tested whether the tracks intersected the active area of the Cherenkov counter. Corrections for the efficiency of the Cherenkov particle identification algorithms were performed separately. Secondary interactions of particles in the target were represented by selectively deleting tracks.

A shortcoming of this spectrometer simulation, (neglecting the fact that the appropriate model for charm production is unknown) is that no background tracks were included in the simulation. Chamber noise was also not included in the simulation. Additionally, the target nuclear motion and beam momentum spread were neglected. Any deviation from a phase space distribution of the decay products was also overlooked. The possibility that the produced charmed state

interacted before decaying was also ignored.

4.1.5 Cherenkov Simulation

The Cherenkov particle identification efficiency was estimated by randomly selecting a track from one data event and embedding it in another data event while also generating additional ADC counts in the appropriate photomultiplier tube channels according to a Poisson distribution. Then the resulting "event" was processed by the Cherenkov analysis code, and the PROBK of the embedded track, whose particle identity was known by construction, was recorded. For those simulated kaon tracks that intersected the active area of the Cherenkov counter and had momenta in the range of 7 to 20 GeV/c, figure 20 shows the probability of the Cherenkov counter and analysis code to properly identify kaons as a function of the PROBK level employed to distinguish kaons from less massive particles. For those simulated pions that had momenta between 7 and 20 GeV/c and intersected the Cherenkov counter within its active area, figure 20 also shows the probability to misidentify those simulated pions as kaons as a function of the PROBK level used to distinguish kaons from pions.

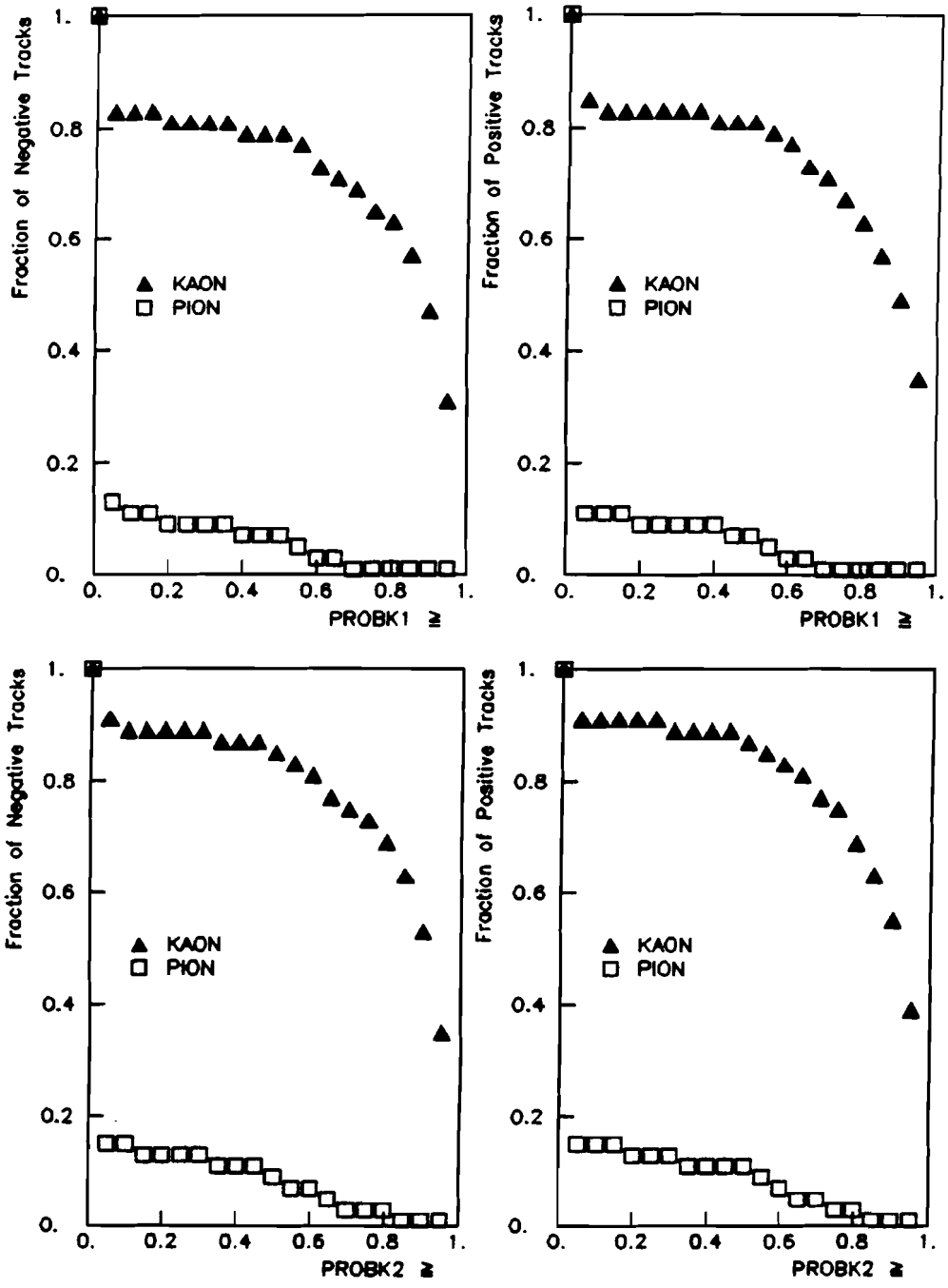

FIGURE 20. Probability for the Cherenkov counter and analysis to properly identify simulated kaons as a function of the PROBK level selected to discriminate kaons from less massive particles. The probability to misidentify a simulated pion as a kaon is also shown. All simulated tracks were required to be in the momentum range of 7 to 20 GeV/c. Results are presented separately for PROBK1 and PROBK2, as well as positive and negative tracks.

4.2 MONTE CARLO RESULTS

The X position of the vertex in the simulated events is always reconstructed within ±0.9 mm of the generated X position. The full width at half maximum of the deviation between the generated and the reconstructed X vertex position for the three-chamber clusters is 0.5 mm.

The momentum resolution of the trigger arm was estimated by comparing the generated momenta from a sample of simulated muon tracks to the reconstructed momenta. The resulting momentum magnitude resolution is

$$(\delta p / p)_T^2 \approx (0.15)^2 + (0.013\ p)^2.$$

More relevant to this particular charm search is the fact that the sign of the reconstructed simulated muon was virtually always the same as the sign of the generated muon.

The forward arm momentum resolution was measured in the same manner as the trigger arm momentum resolution. Including the effects of multiple scattering, chamber resolution, and efficiency, the forward arm momentum resolution is

$$(\delta p / p)_F^2 \approx (0.0060)^2 + (0.00066\ p)^2.$$

The track finding efficiency of the analysis programs can also be estimated with a Monte Carlo simulation. The trigger arm tracking program exhibited essentially no inefficiency in reconstructing tracks that had enough hits to meet the minimum requirements for the track to be found. The forward arm track finding program was about 97 percent

efficient for all tracks with momenta above 7 GeV/c, but the efficiency fell off at lower momenta, due to the simple lens model employed in the YZ tracking. The forward arm track finding program efficiency as a function of the track's momentum is shown in figure 21(a). A more careful treatment of the bending in the YZ view should allow the efficiency of the reconstruction program to be improved. The track reconstruction efficiency as a function of momentum with the chamber inefficiencies imposed is shown in figure 21(b).

The acceptance of the spectrometer for charmed particles was calculated for each of the three production models presented in the subsection on particle generators. For the uncorrelated models, several values of the parameter controlling the x_F dependence of the produced states are presented.

Figure 22 illustrates the trigger arm acceptance for muons from the semileptonic decay of D mesons as a function of the x_F and p_T of the parent D meson. The trigger arm acceptances for muons from the D meson decay mode $D \rightarrow K\mu\nu$ are presented in table 3. Table 4 presents the trigger arm muon acceptance for muons from the D decay mode $D \rightarrow K^*(890)\mu\nu$. (The natural width of the $K^*(890)$ meson was neglected in this simulation since studies indicated that the trigger arm acceptance is insensitive to the natural width of the $K^*(890)$.) The quoted uncertainties are purely statistical. These acceptance values include the effects of chamber inefficiencies and various software

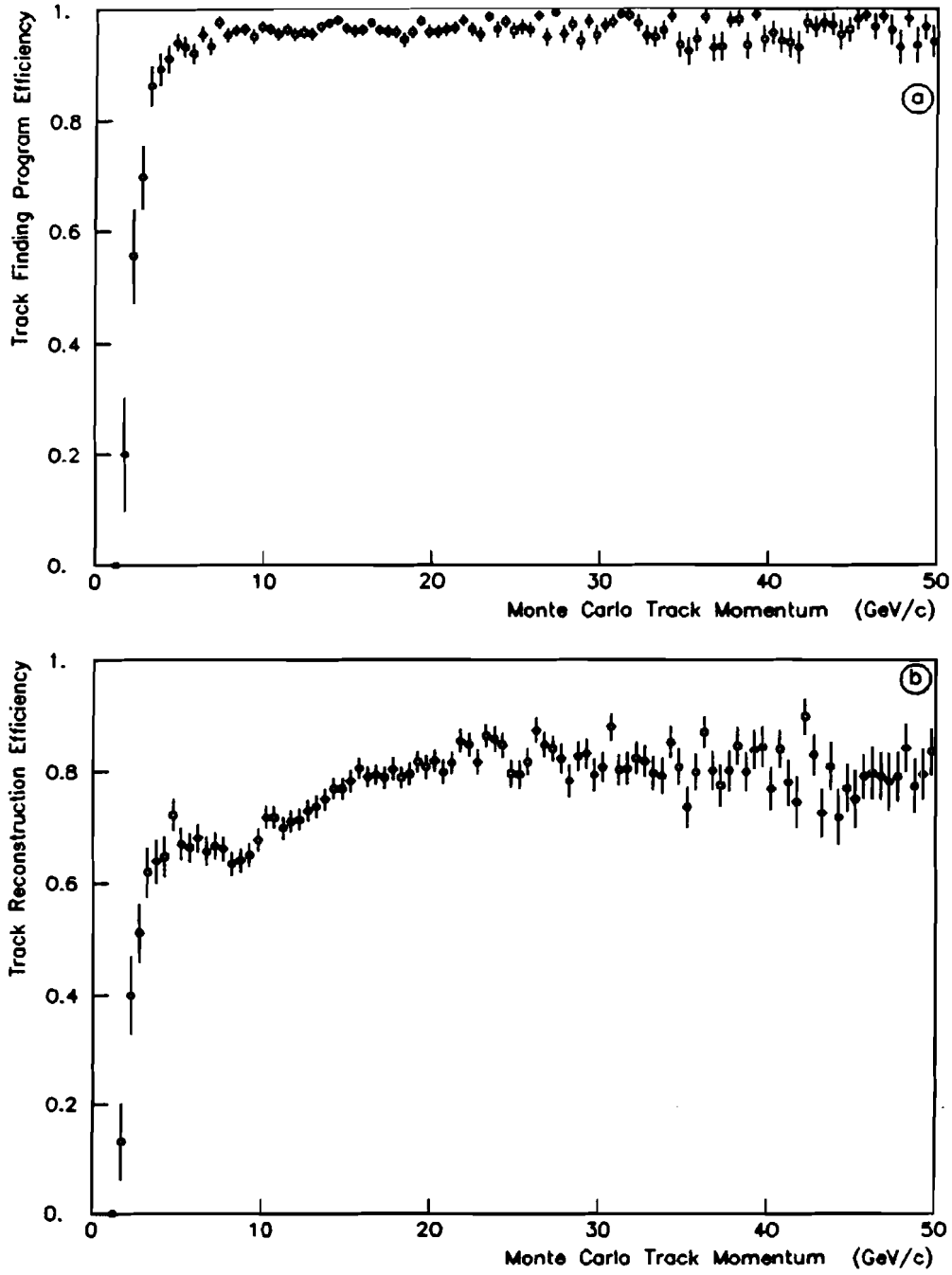

FIGURE 21. Efficiency of the forward arm track finding programs as a function of the momentum of the simulated track. (a) With 100 percent efficient chambers. (b) With measured chamber efficiency maps employed.

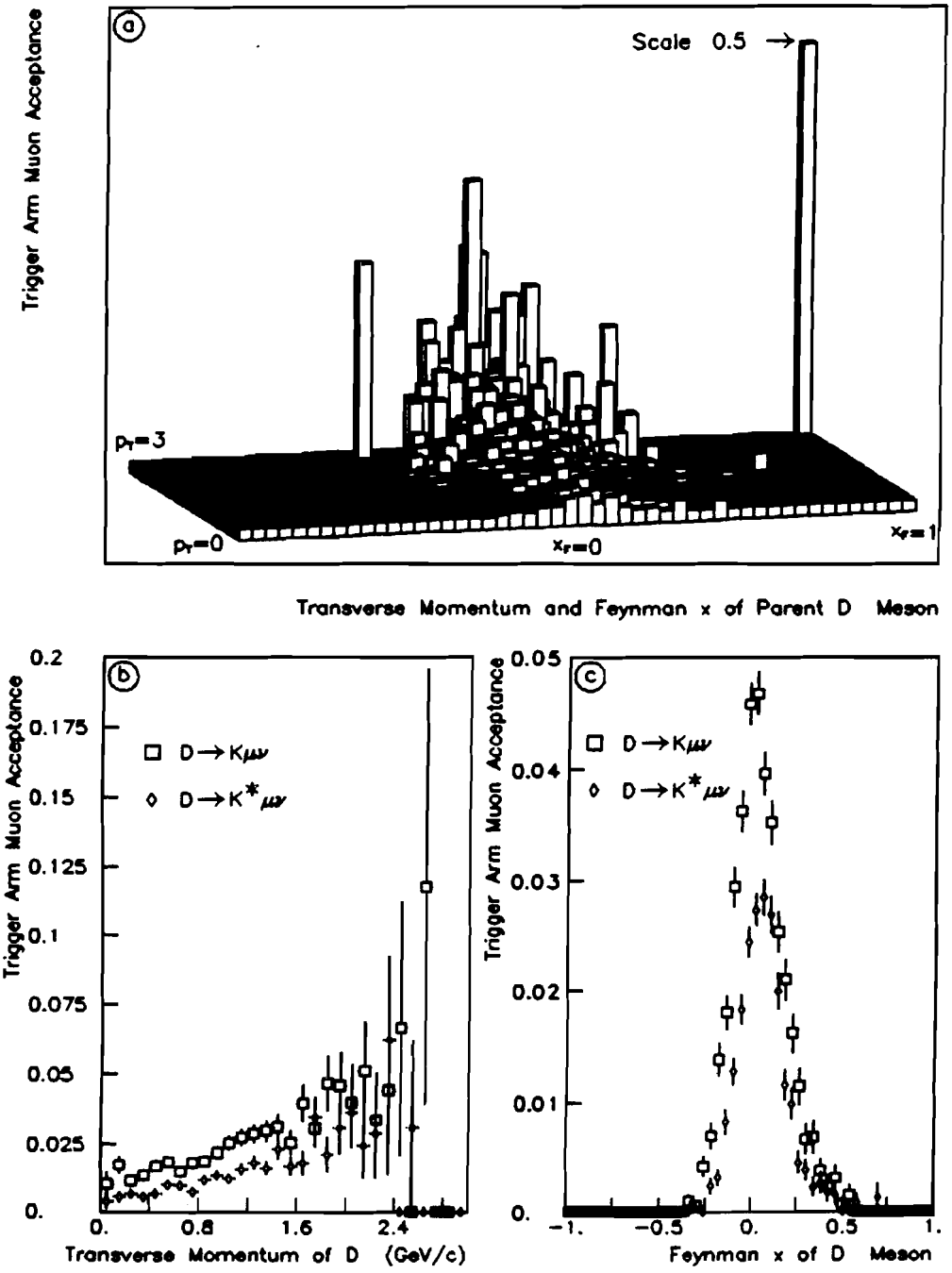

FIGURE 22. Trigger arm acceptance for muons from the semileptonic decay of D mesons. (a) Acceptance as a function of the x_F and p_T of the generated D mesons. (b) Acceptance as a function of p_T using model I with n=3. (c) Acceptance as a function of x_F using model I with b=1.1 $(GeV/c)^{-2}$.

TABLE 3. Acceptance of the trigger arm for muons from the decay $D \to K\mu\nu$. Results are presented for several different D meson production models. The quoted uncertainties represent the statistical uncertainties of the Monte Carlo simulation.

			$D \to K \mu \nu$		
Production Model	n	b	μ^- Acceptance	μ^+ Acceptance	Average Acceptance
I	1	1.1	0.0129±0.0007	0.0134±0.0007	0.0131±0.0005
I	3	1.1	0.0217±0.0007	0.0211±0.0006	0.0214±0.0006
I	6	1.1	0.0283±0.0010	0.0303±0.0011	0.0293±0.0008
II	1	1.1	0.0181±0.0008	0.0184±0.0008	0.0182±0.0006
II	3	1.1	0.0251±0.0010	0.0234±0.0010	0.0242±0.0007
II	6	1.1	0.0298±0.0011	0.0299±0.0011	0.0298±0.0008
III	5	2.0	0.0353±0.0008	0.0361±0.0008	0.0357±0.0006

TABLE 4. Acceptance of the trigger arm for muons from the decay $D \to K^*(890)\mu\nu$. Results are presented for several different D meson production models. The quoted uncertainties represent the statistical uncertainties of the Monte Carlo simulation.

			$D \to K^*(890)\ \mu\ \nu$		
Production Model	n	b	μ^- Acceptance	μ^+ Acceptance	Average Acceptance
I	1	1.1	0.0073±0.0005	0.0079±0.0006	0.0076±0.0004
I	3	1.1	0.0115±0.0007	0.0124±0.0007	0.0119±0.0005
I	6	1.1	0.0172±0.0008	0.0171±0.0008	0.0171±0.0006
II	1	1.1	0.0100±0.0006	0.0117±0.0007	0.0109±0.0005
II	3	1.1	0.0151±0.0008	0.0145±0.0008	0.0148±0.0005
II	6	1.1	0.0180±0.0008	0.0193±0.0009	0.0186±0.0006
III	5	2.0	0.0208±0.0006	0.0228±0.0007	0.0218±0.0005

cuts employed to isolate the likely muon candidates from accidental tracks in the trigger arm. On average, the imposition of the trigger arm PWC efficiencies accounted for a six percent reduction in the muon acceptance, while the imposition of other software cuts reduced the acceptance by one percent. Note that the trigger arm muon acceptances were basically independent of the sign of the muon for the models tested.

The acceptance of the forward arm for the D meson decay $D \to K\pi$ is illustrated in figure 23, and tabulated in table 5. The column labeled "Geometric Acceptance" represents the acceptance of the spectrometer when the detectors and the track finding program were assumed to have no inefficiency. The column labeled "Acceptance" contains the forward arm acceptance including the effects of chamber inefficiencies and track reconstruction inefficiencies. The column labeled "CER Acceptance" includes the additional requirement that the kaon momentum was in the range of 7 to 20 GeV/c, and that the kaon intersected the active area of the Cherenkov counter. The CER acceptances do not include a correction for the efficiency of the Cherenkov identification. All uncertainties quoted in the table are purely statistical. The correlated model forward arm acceptance was only calculated for those simulated events in which the trigger muon from the partner state was reconstructed in the trigger arm.

Table 6 presents forward arm acceptances for the decay modes $D \to K\pi\pi\pi$ and $D \to K\pi\pi$. Figure 24 illustrates the acceptance of the forward arm for the charged D^* decay into a charged pion and a neutral D meson

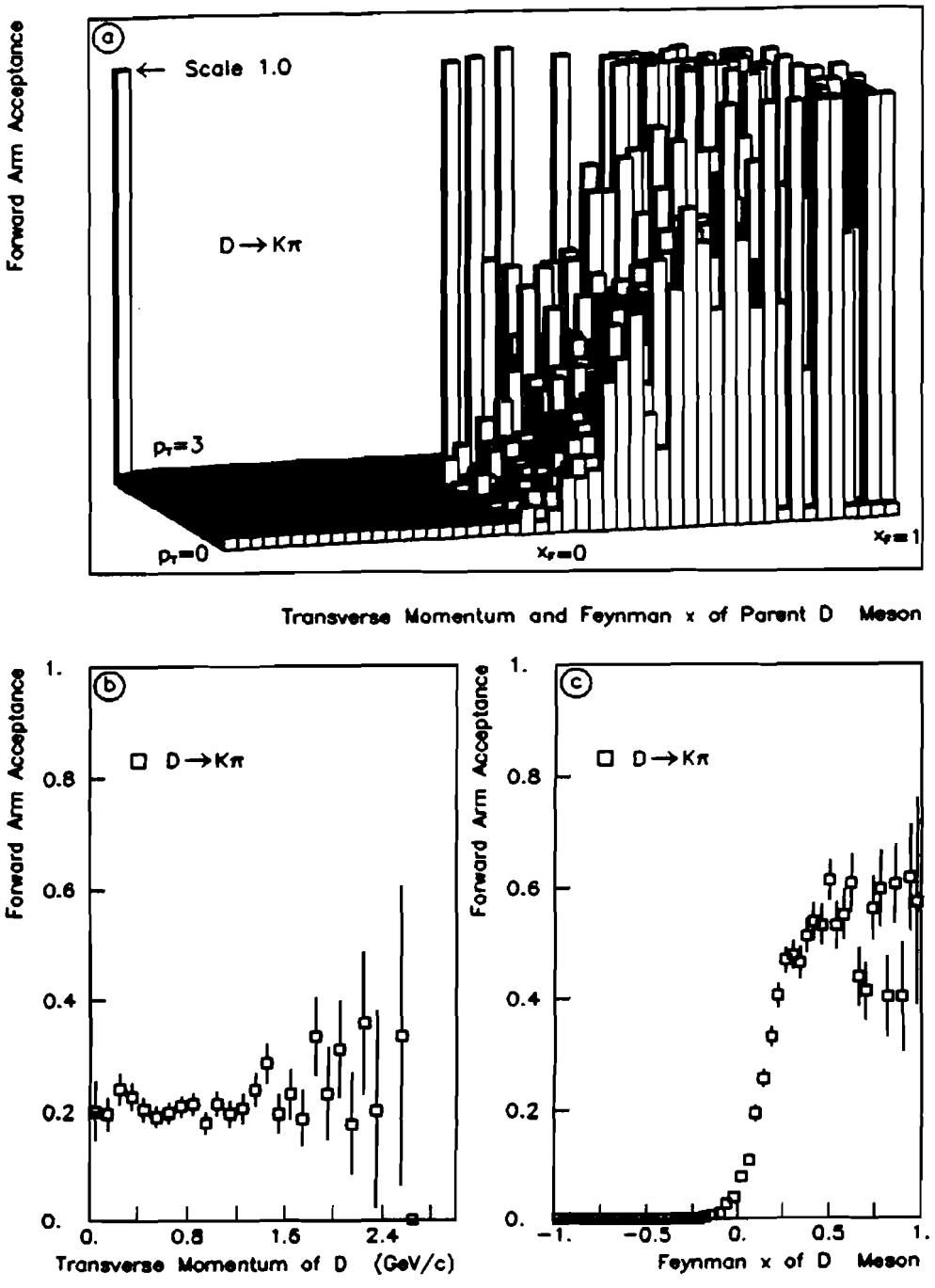

FIGURE 23. Forward arm acceptance for the D meson decay $D \to K\pi$. (a) Acceptance as a function of the x_F and p_T of the generated D meson. (b) Acceptance as a function of p_T using model I with $n=\frac{3}{2}$. (c) Acceptance as a function of x_F using model I with b=1.1 (GeV/c)$^{-2}$.

TABLE 5. Acceptance of the forward arm for $D \to K\pi$. Results are presented for several different D meson production models. Entries in the column labeled "Acceptance" include the effects of chamber inefficiencies. Entries in the column labeled "CER Acceptance" also include the requirement that the kaon be discernible by Cherenkov counter. The quoted uncertainties represent the statistical uncertainties of the Monte Carlo simulation.

				$D \to K \pi$		
Production Model	n	b	Kaon Sign	Geometric Acceptance	Acceptance	CER Acceptance
I	1	1.1	+	0.346±0.009	0.207±0.008	0.041±0.004
I	1	1.1	-	0.337±0.010	0.202±0.008	0.041±0.004
I	3	1.1	+	0.271±0.009	0.146±0.007	0.043±0.004
I	3	1.1	-	0.273±0.009	0.159±0.007	0.055±0.005
I	6	1.1	+	0.221±0.008	0.120±0.006	0.052±0.004
I	6	1.1	-	0.212±0.008	0.118±0.006	0.049±0.004
II	1	1.1	+	0.278±0.009	0.160±0.007	0.045±0.004
II	1	1.1	-	0.301±0.009	0.174±0.008	0.048±0.004
II	3	1.1	+	0.233±0.008	0.135±0.007	0.054±0.004
II	3	1.1	-	0.244±0.009	0.142±0.007	0.053±0.005
II	6	1.1	+	0.198±0.008	0.112±0.006	0.047±0.004
II	6	1.1	-	0.198±0.008	0.105±0.006	0.045±0.004
III	5	2.0	+	0.200±0.007	0.107±0.006	0.058±0.004
III	5	2.0	-	0.216±0.008	0.115±0.006	0.060±0.004

TABLE 6. Acceptance of the forward arm for $D \to K\pi\pi\pi$ and $D \to K\pi\pi$. Results are presented for D meson production model II. Entries in the column labeled "Acceptance" include the effects of chamber inefficiencies. Entries in the column labeled "CER Acceptance" also include the requirement that the kaon be discernible by Cherenkov counter. The quoted uncertainties represent the statistical uncertainties of the Monte Carlo simulation.

$D \to K \pi \pi \pi$

Production Model	n	b	Kaon Sign	Geometric Acceptance	Acceptance	CER Acceptance
II	3	1.1	+	0.117±0.005	0.039±0.003	0.020±0.002
II	3	1.1	-	0.108±0.004	0.037±0.003	0.020±0.002

$D \to K \pi \pi$

Production Model	n	b	Kaon Sign	Geometric Acceptance	Acceptance	CER Acceptance
II	3	1.1	+	0.171±0.007	0.070±0.005	0.031±0.003
II	3	1.1	-	0.161±0.007	0.074±0.005	0.033±0.004

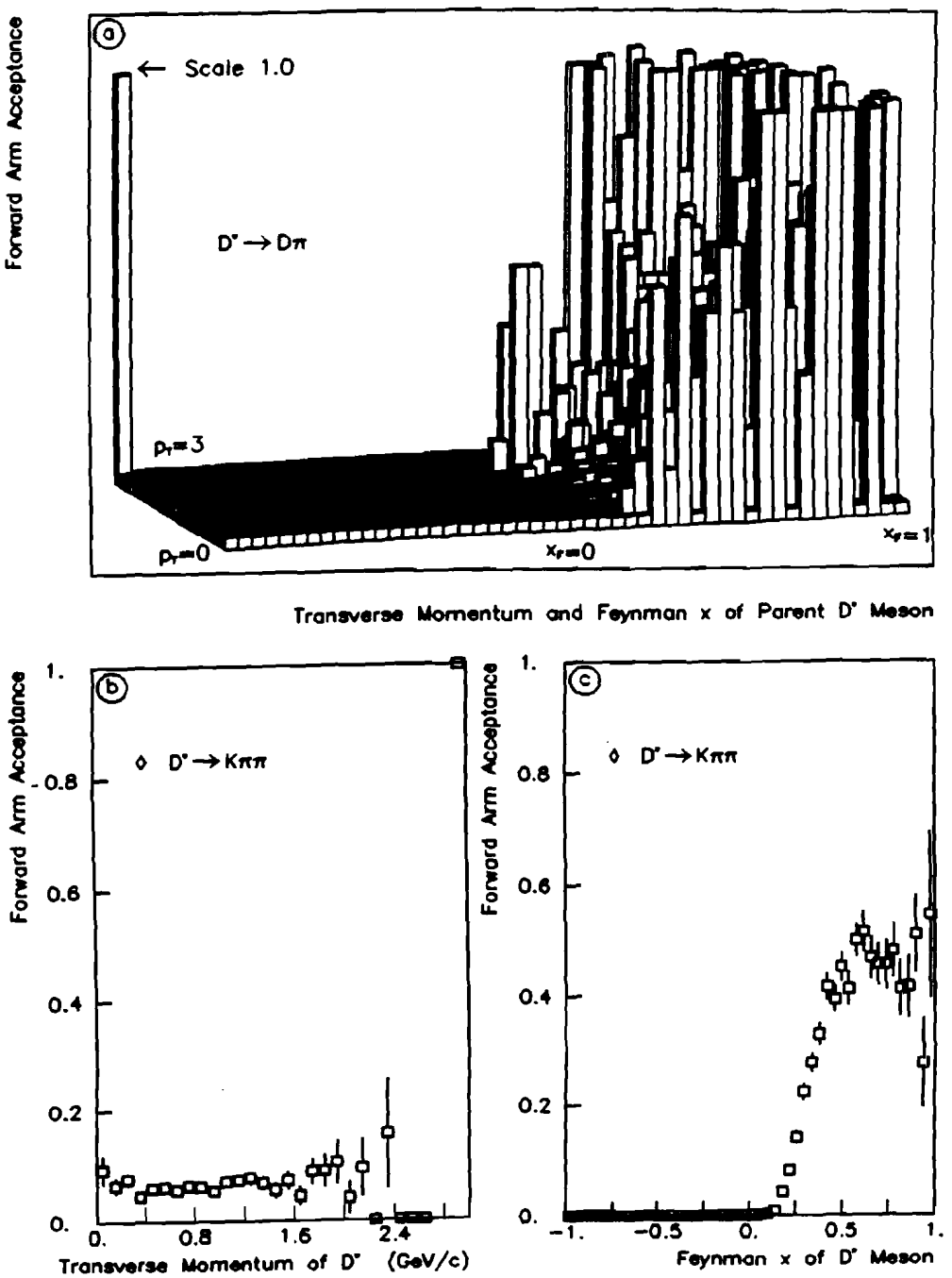

FIGURE 24. Forward arm acceptance for the charged D^* meson decay $D^* \rightarrow D\pi^{\pm}$ followed by $D_* \rightarrow K\pi$. (a) Acceptance as a function of the x_F and p_T of the generated D^* meson. (b) Acceptance as a function of p_T using model I with $n=3_{-2}$ (c) Acceptance as a function of x_F using model I with b=1.1 $(GeV/c)^{-2}$.

when the neutral D meson decayed into a charged kaon and a charged pion. The forward arm acceptances for this charged D^* decay mode are listed in table 7.

The chamber efficiencies together with the minimum hit requirements used to define a track result in a 75 percent efficiency for finding a forward arm track that was geometrically accepted by the forward arm. About two percent of the simulated particles undergo secondary interactions in the target. Roughly six percent of the simulated forward arm kaons and one percent of the simulated pions decayed before getting through the last drift chamber.

Figure 25 illustrates the mass resolution of the spectrometer for the reconstructed simulated $D \rightarrow K\pi$ decays generated by model I. The mean mass of the reconstructed simulated D meson decays was about 0.003 GeV/c^2 lower than the generated mass. This mass shift is apparently due to the polynomial invoked in the momentum analysis. The width of the reconstructed state was dependent upon the production model selected, and the mass resolution for the centrally produced D mesons was generally better than the resolution for the forward D mesons.

The resolution of the spectrometer for the charged D^* decays generated by model I with n=3 and b=1.1 $(GeV/c)^{-2}$ is illustrated in figure 26.

TABLE 7. Acceptance of the forward arm for charged D^* decay $D^*\to D\pi$ followed by $D\to K\pi$. Results are presented for D^* meson production models I and II. Entries in the column labeled "Acceptance" include the effects of chamber inefficiencies. Entries in the column labeled "CER Acceptance" also include the requirement that the kaon be discernible by Cherenkov counter. The quoted uncertainties represent the statistical uncertainties of the Monte Carlo simulation.

$$\begin{array}{l} D^* \to D\,\pi \\ \qquad\;\hookrightarrow K\,\pi \end{array}$$

Production Model	n	b	Kaon Sign	Geometric Acceptance	Acceptance	CER Acceptance
I	1	1.1	+	0.274±0.006	0.116±0.005	0.018±0.002
I	1	1.1	-	0.260±0.006	0.110±0.004	0.017±0.002
I	3	1.1	+	0.174±0.005	0.066±0.004	0.014±0.002
I	3	1.1	-	0.161±0.005	0.056±0.003	0.010±0.001
I	6	1.1	+	0.091±0.004	0.026±0.002	0.006±0.001
I	6	1.1	-	0.089±0.004	0.027±0.002	0.006±0.001
II	3	1.1	+	0.113±0.004	0.040±0.003	0.007±0.001
II	3	1.1	-	0.113±0.005	0.035±0.003	0.007±0.001

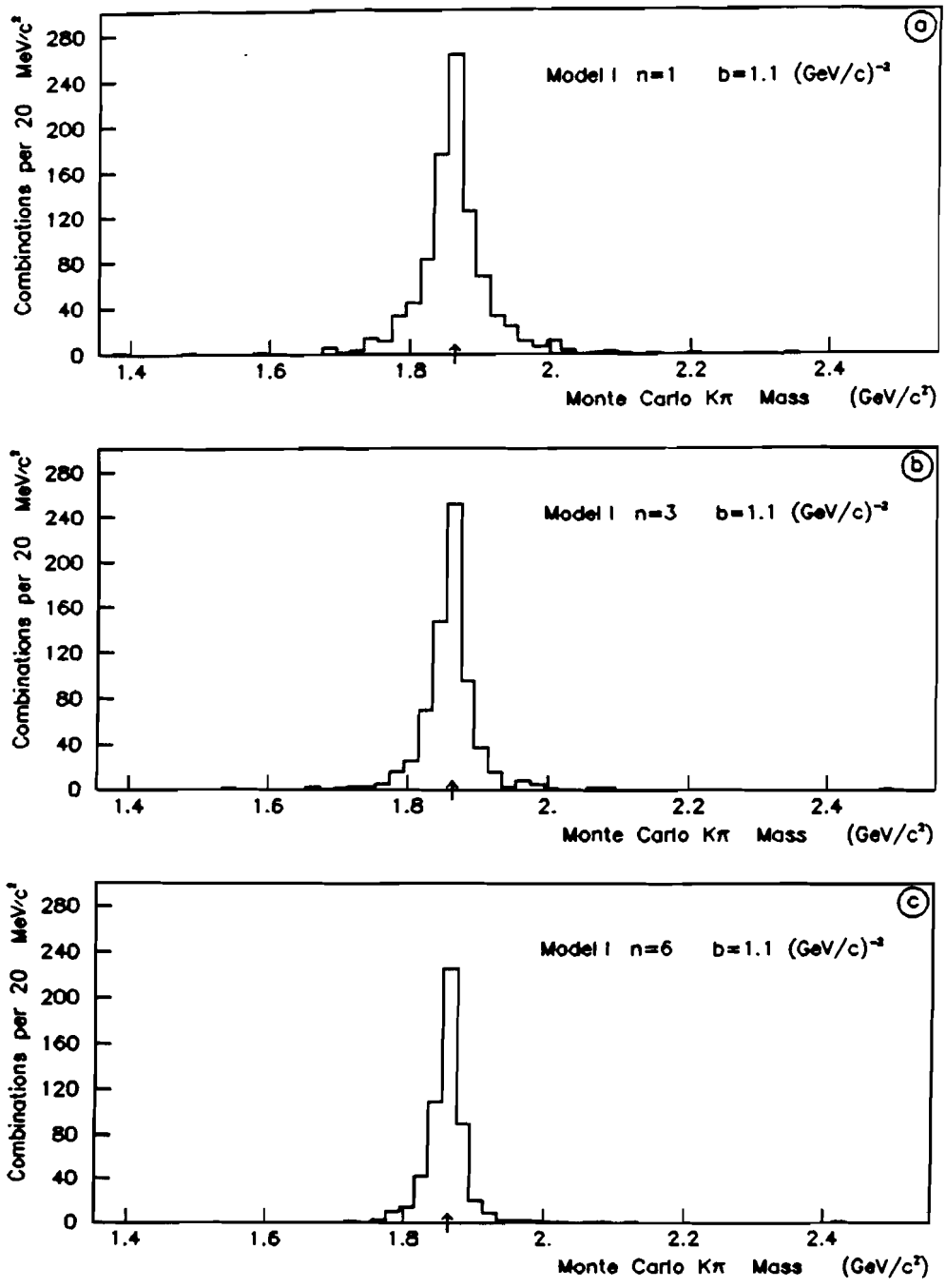

FIGURE 25. Kπ invariant mass plots resulting from the analysis of Monte Carlo simulated events produced with model I using $b=1.1\ (GeV/c)^{-2}$ and several values of n. There were 5000 $D \rightarrow K\pi$ decays generated and analyzed for each value of n.
(a) n=1. (b) n=3. (c) n=6.

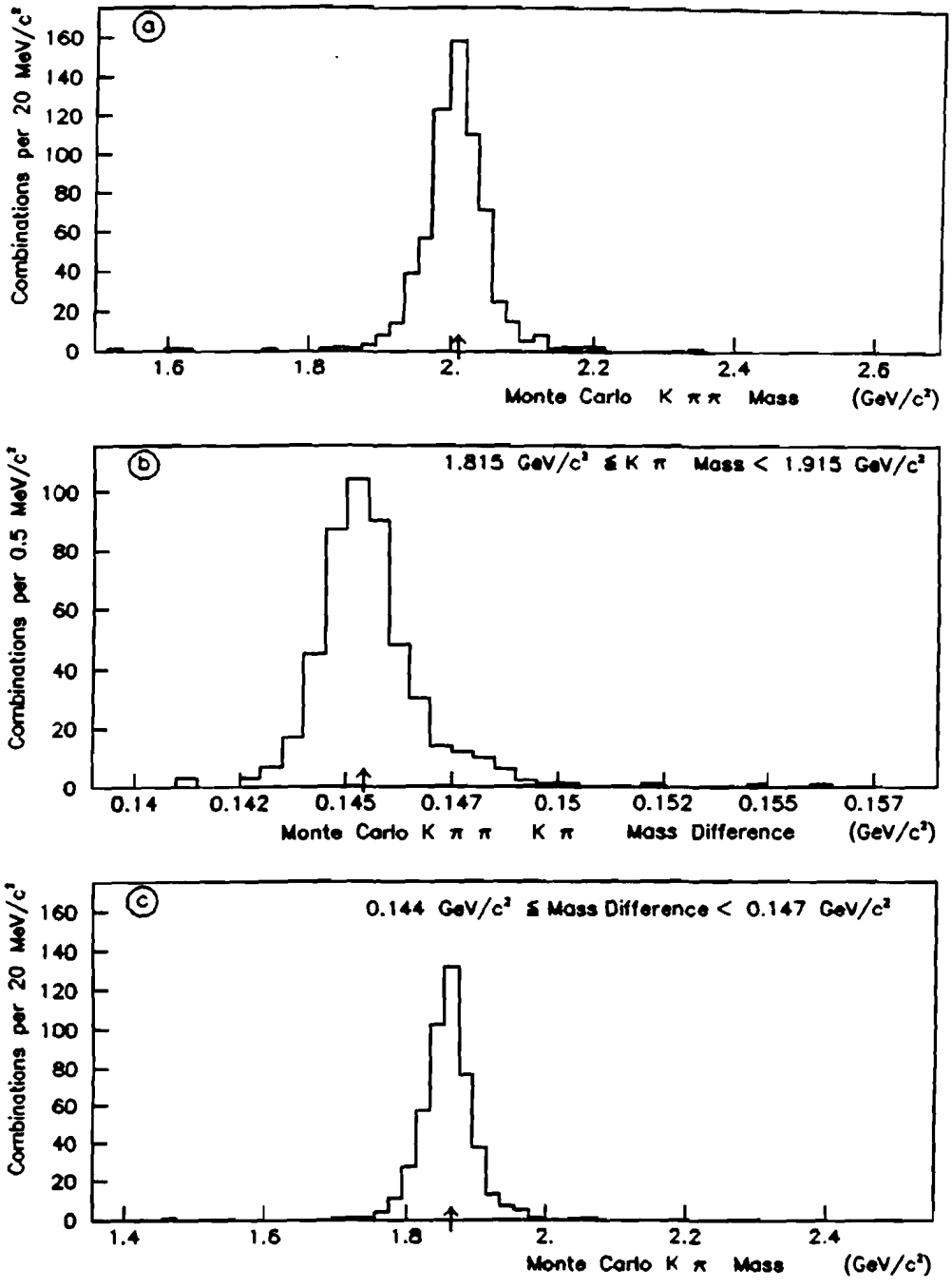

FIGURE 26. Charged D^* mass plots resulting from the analysis of 10 000 Monte Carlo simulated events produced with model I using n=3 and b=1.1 $(GeV/c)^{-2}$. (a) $K\pi\pi$ invariant mass plot of D^* meson. (b) $K\pi$ invariant mass plot of neutral D meson from charged D^* decay. (c) D^* minus D mass plot.

CHAPTER 5

THE CHARM SEARCH

This chapter describes some of the analysis techniques employed in searching for evidence of hadronic production of charm among the events summarized on the DST, and presents several mass plots. The first section of this chapter contains a summary of the information obtained from the scalers. The second section discusses some criteria that were employed in excluding DST events and particle combinations from contributing to various invariant mass plots. The third section describes the particle identification schemes employed in calculating the invariant mass of forward arm particle combinations. The fourth section illustrates the spectrometer's capabilities via mass plots that show clear evidence of some non-charmed particle decays. The fifth section describes additional requirements placed upon the trigger arm tracks to define a triggering muon. The last section

presents some of the invariant mass plots that were employed in the charm search.

5.1 SCALERS

As described in the second chapter, signals from many of the scintillation counters in the experiment were sent to scalers, which accumulated a sum of the number of such signals detected per spill. The scalers were divided into two sets, the beamgated scalers, which were inhibited from accumulating by the $\overline{\text{BEAMGATE}}$ signal, and the livetime scalers, which were inhibited by the signal DT+$\overline{\text{BEAMGATE}}$. These scalers provided a monitor of the stability of the beam targeting, and the trigger logic. The scalers also provided an estimate of the total number of incident beam particles and the livetime fraction of the apparatus.

5.1.1 Processing of the Scalers

All the raw data tapes that eventually contributed events to the DST were processed by a program which checked that the order of the types of events recorded on the data tapes were consistent with expectations [85]. Events were grouped into "logical spills" which were required to be less than three seconds in duration. Any logical spill that contained a test pulse trigger sandwiched between data

triggers, or was missing the end-of-spill scaler record was considered to be a "damaged spill." The event numbers and run numbers of all events that were members of damaged spills were recorded on an output file. About 0.6 percent of the A interrupts were members of damaged spills. All end-of-spill scaler records were written to a separate series of magnetic tapes, and then the end-of-spill scaler records were summed by run for each individual scaler, to provide the following results.

5.1.2 Scaler Sums and Rates

The average beamgated BEAM per spill for each run employed in this charm search is shown in figure 27. The mean BEAM per spill was 4.81×10^{6}.

The mean livetime B1 per livetime BEAM for each run is shown in figure 28(a). Figure 28(b) illustrates the mean livetime B2 per livetime BEAM, while figure 28(c) shows the mean livetime B1*B2 per livetime BEAM for individual runs. These scaler ratios indicate that the incident beam was on average well centered upon the B1 and B2 overlap, and at least 83 percent contained within the B1*B2 overlap.

Figure 29(a) shows the mean livetime M per livetime BEAM for individual runs, and its mean was 4.93×10^{-5}. Figure 29(b) shows the ratio of the livetime $M*\overline{A}$ to the livetime BEAM for individual runs, and the ratio had a mean value of 1.05×10^{-5}. The mean number of

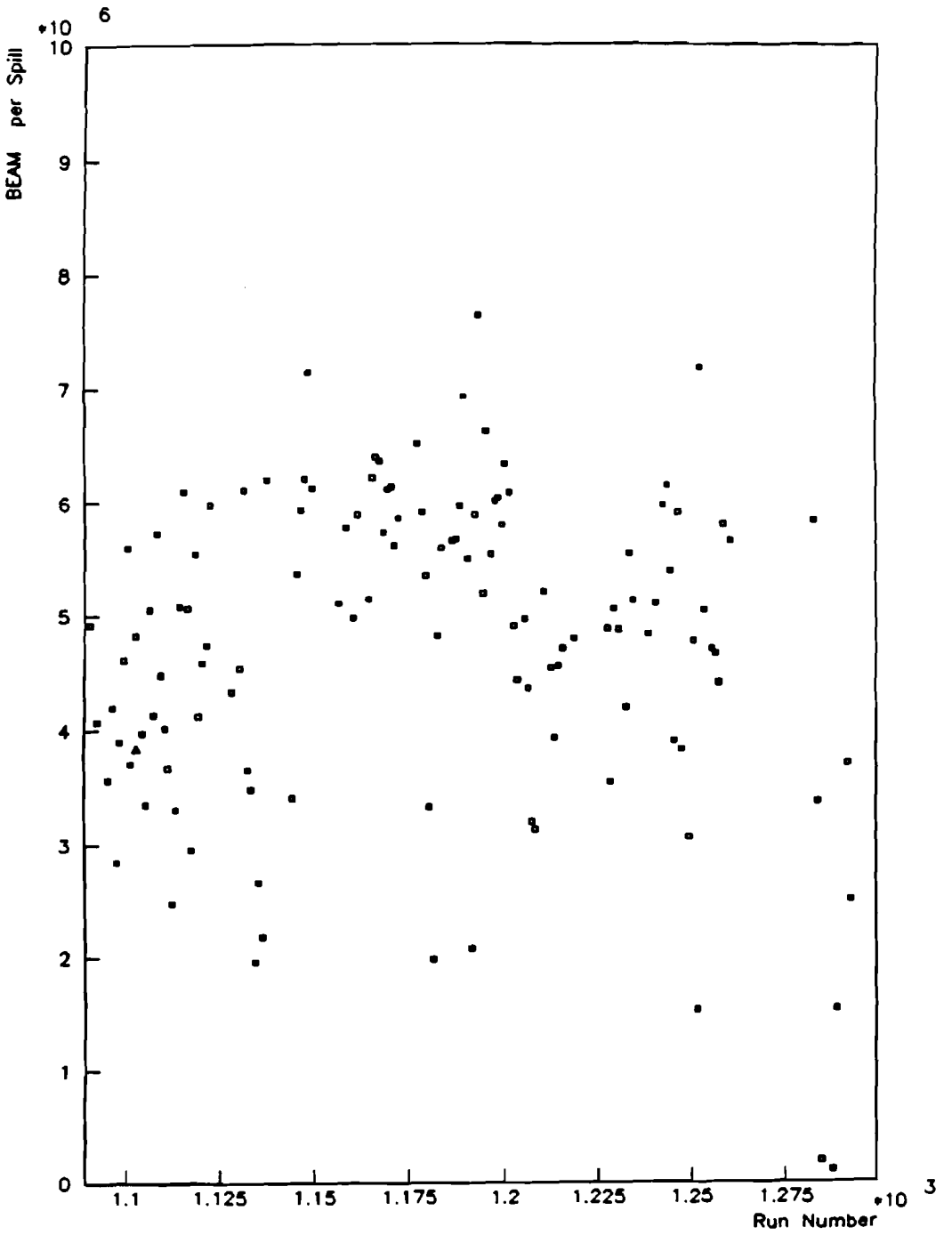

FIGURE 27. Average beamgated BEAM per spill for all runs employed in this charm search.

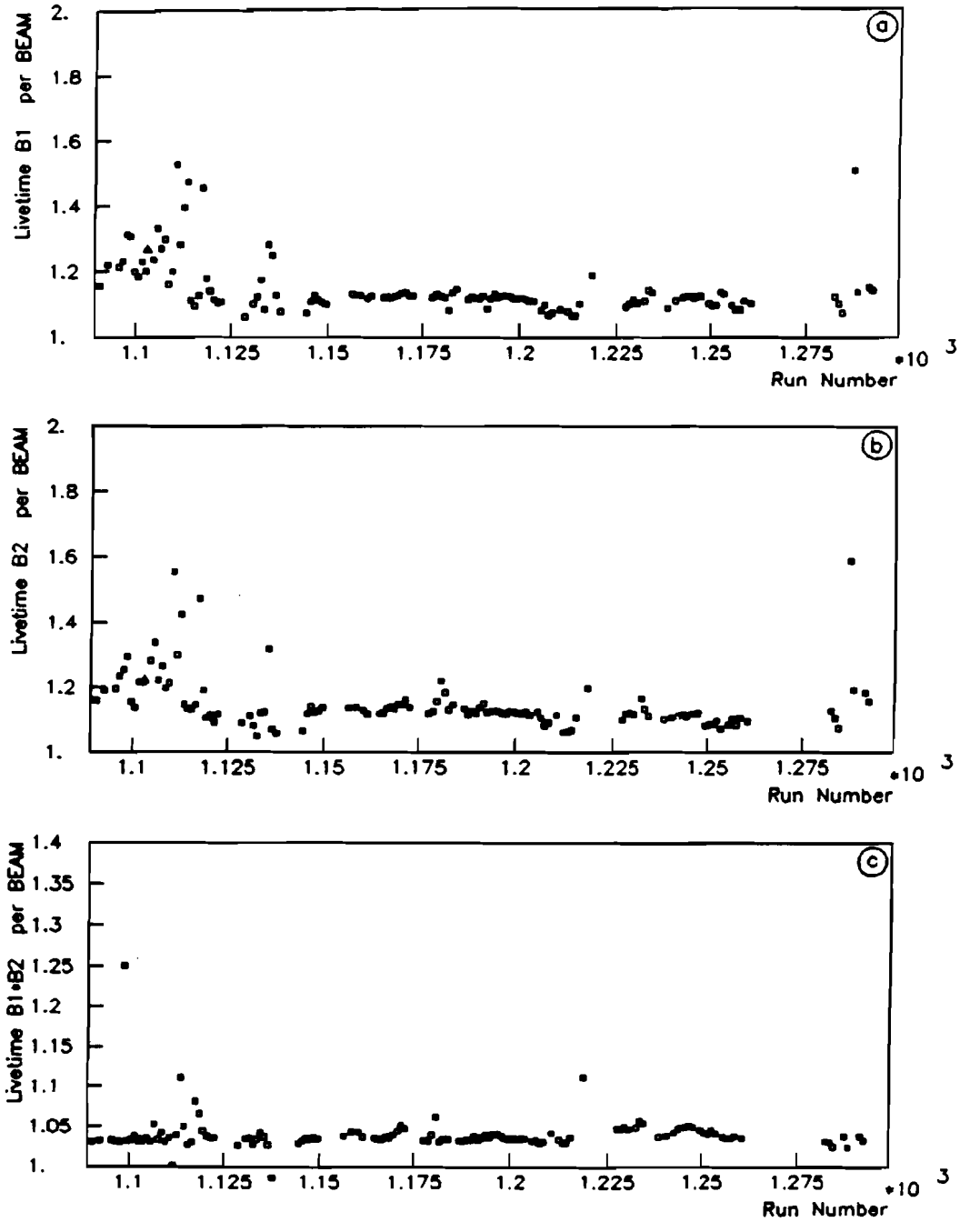

FIGURE 28. Beam related scaler ratios for all runs employed in this charm search. (a) Livetime B1 per livetime BEAM. (b) Livetime B2 per livetime BEAM. (c) Livetime B1*B2 per livetime BEAM.

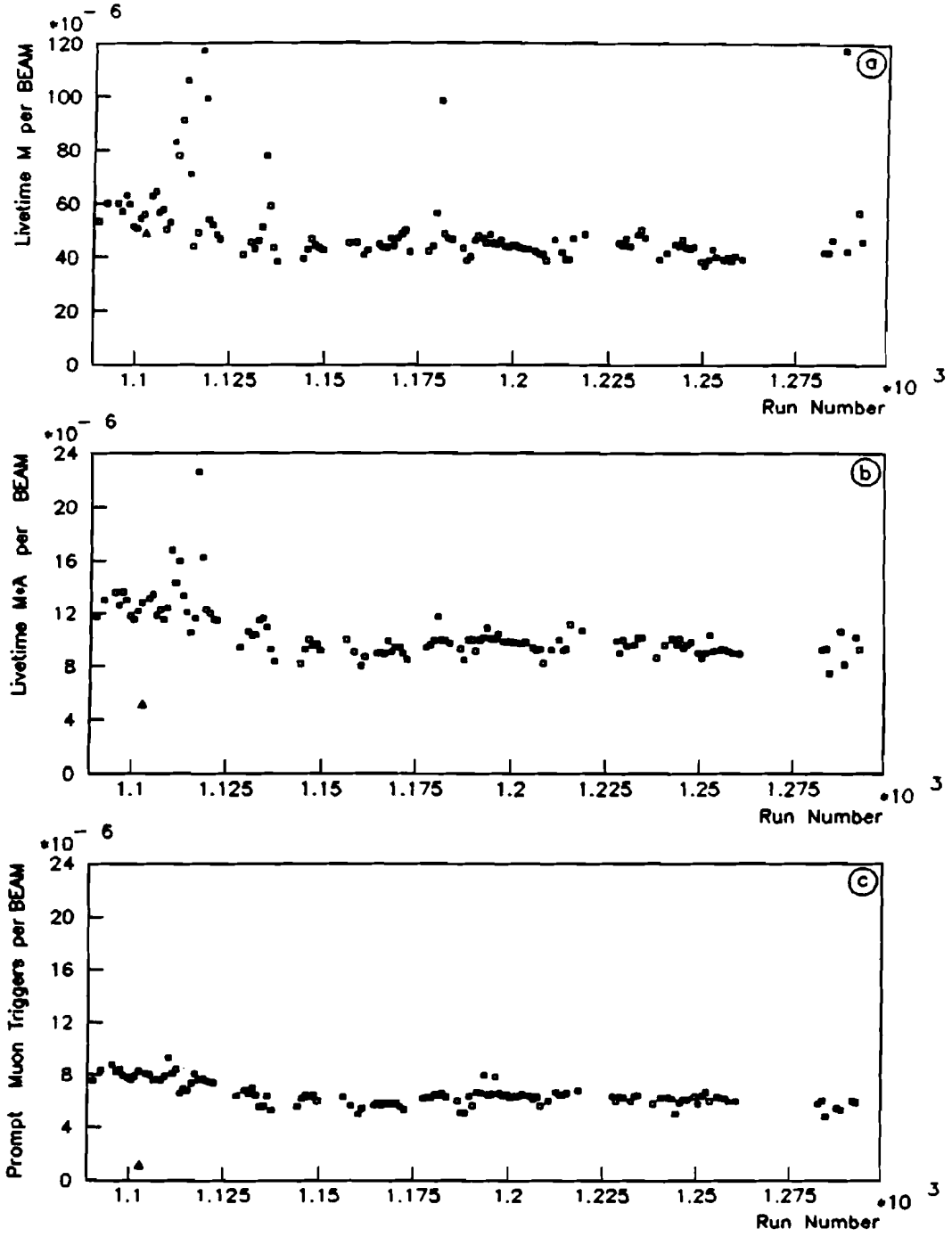

FIGURE 29. Trigger arm scaler ratios for all runs employed in this charm search. (a) Livetime M per livetime BEAM. (b) Livetime M*$\bar{A}$ per livetime BEAM. (c) Number of prompt muon triggers per livetime BEAM.

prompt muon triggers per livetime BEAM was 6.56×10^{-6}, and the ratio is shown for individual runs in figure 29(c). It is clear that the trigger rate, that is, the number of prompt muon triggers per BEAM, changed during the course of the data accumulation. One possible contribution to the change in the trigger rate might have been a shift in the quality or steering of the beam incident upon the spectrometer target. (However, based upon an analysis of a target-out run, the beam steering or quality was not responsible for more than 40 percent of the change in the trigger rate.) Another possibility is that the trigger rate changed due to minor adjustments made to the trigger timing between runs during the early runs. Furthermore, the veto counters A8 and A9 were added after run 1112, so some portion of the larger trigger rate during the early runs may be due to accidentals that would have been vetoed during the later runs by the additional veto counters. Another possible contributor to the larger trigger rate during the early runs is that the number of incident beam particles may have been underestimated during those runs due to improper thresholds on the B1 and B2 discriminators.

The sums of the livetime scalers over all the runs that were employed in the charm search are listed in table 8. A total of 82 196 undamaged spills contributed to the scaler sums listed in that table. Any livetime scaler sum divided by the corresponding beamgated scaler sum measures the fraction of the time that the apparatus was capable of detecting and processing a trigger, and that fraction is referred to as the "livetime fraction." The available estimates of

TABLE 8. Scaler sums and rates.

Scaler	Livetime Scaler Sum	Livetime Sum per Spill	Livetime Sum per BEAM	Fractional Livetime
B1	305 836 141 704	3 720 815	1.142	
B2	307 009 751 908	3 735 094	1.146	
B1*B2	278 244 950 873	3 385 140	1.039	0.678
BEAM	267 910 908 520	3 259 415	1.000	0.678
A6	13 267 206 813	161 409	0.0495	0.837
A7	8 562 486 549	104 172	0.0320	0.693
$\overline{A}$	16 395 329 366	199 466	0.0612	
M0*M00	5 283 672 145	64 281	0.0197	
M1R	2 453 048 744	29 844	0.00916	
M1	4 392 619 695	53 441	0.0164	
M2	5 656 926 971	68 822	0.0211	
M3	6 145 595 230	74 768	0.0229	
M	13 207 145	161	0.0000493	0.684
M*$\overline{A}$	2 818 023	34	0.0000105	0.672
M TRIG	1 758 663	22	0.00000656	

the livetime fraction are also listed in table 8. The estimates are nearly in agreement, with the exception of ratio of the A6 sums (which are distorted by a problem with the A6 scaler during the early runs). Figure 30 presents the fractional livetime as estimated by the BEAM scalers for individual runs.

5.1.3 Beam Count

The total number of beam particles incident upon the target while the spectrometer was capable of recording events must be estimated in order to report any production cross section results. For the runs employed in this charm search, the livetime BEAM scaler sum yielded a total of 2.679×10^{11} counts in the undamaged spills. A number of small corrections were applied to this BEAM sum to obtain the best estimate of the total number of live incident beam particles.

A correction to the BEAM sum was made to account for the presumed underestimation of the beam flux during the early runs due to the B1 and B2 discriminator thresholds. This correction factor is estimated to be 1.07, based upon the change in the number of M per BEAM observed between the early and the later runs.

Since the fast logic generated signals that were 10 nsec wide, and the particle beam delivered by the accelerator had an RF structure which caused the particles to be grouped into bunches that were separated in time by 19 nsec, the scalers of the BEAM signal counted

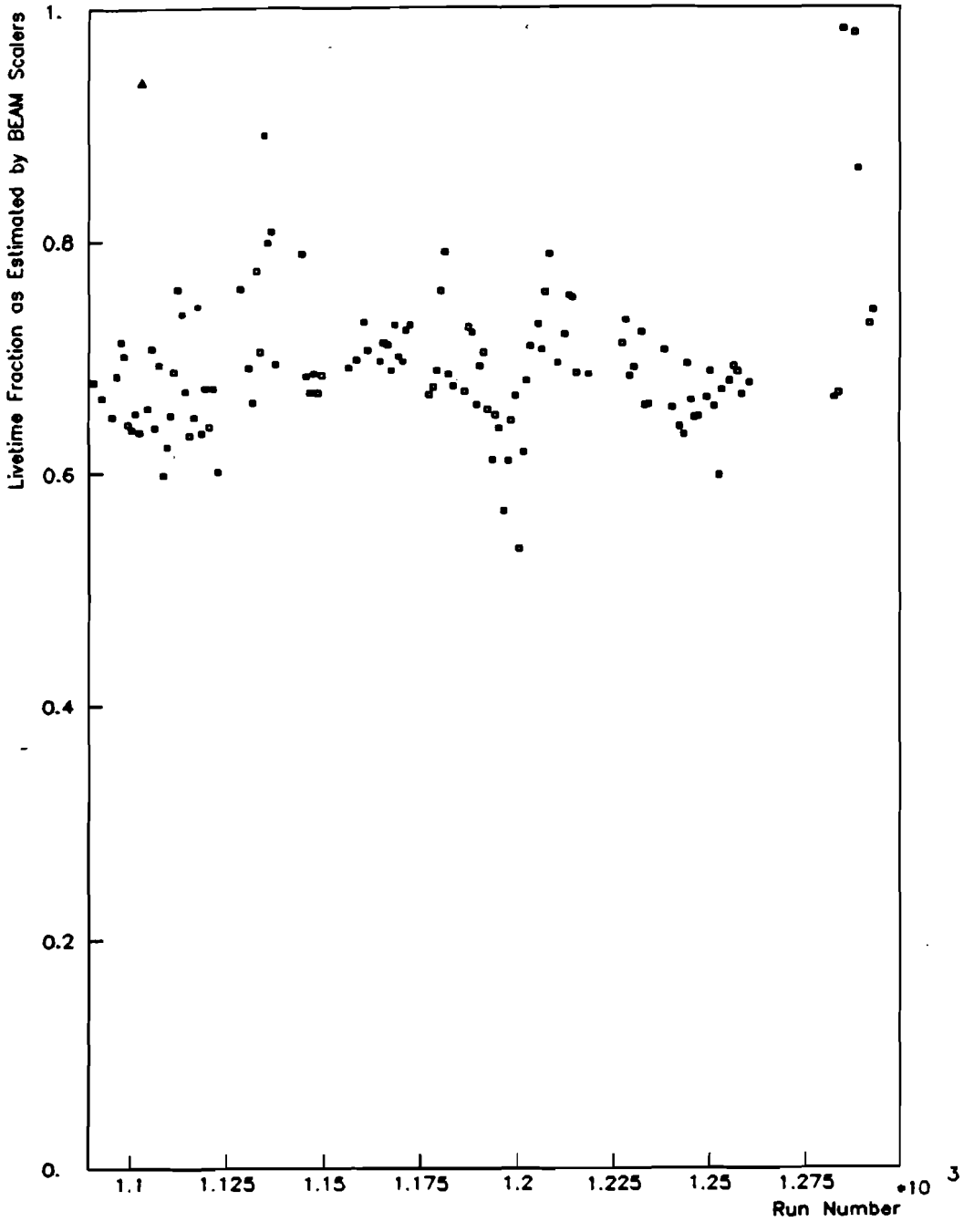

FIGURE 30. Spectrometer livetime fraction as estimated by the BEAM scalers for all runs employed in this charm search.

only the number of occupied bunches. The number of beam particles in each occupied bunch was not measured. The correction to the BEAM sum to account for multiple occupancy of the bunches was estimated by assuming that the bunch occupancy was described by a Poisson distribution, and that the character of the beam was basically uniform throughout the spill. Based upon the beamgated scaler BEAM sum (and including the B1 and B2 threshold correction), there were on average 5.14×10^{6} occupied bunches per spill, and since the spill had a one second duration, there were 5.26×10^{7} bunches per spill. Thus the probability that a bunch was occupied is estimated to be 0.098. Assuming the Poisson distribution was applicable, the mean occupancy of a bunch was 0.103. The probability that a bunch contained one particle is 0.093. The probability that a bunch contained two particles is 0.005. The probability that a bunch contained three or more particles is $2.\times10^{-4}$. The correction factor which is to be multiplied by the livetime BEAM scaler sum to account for multiple occupancy of the bunches is given by the mean occupancy divided by the probability that a bunch is occupied and is equal to 1.05. Measurements of the probability that the bunch following an occupied bunch was also occupied yielded a value of 0.20 ± 0.03, which is a factor of two larger than anticipated for a uniform spill. The distribution of the time of triggers relative to the beginning of the spill was found to be relatively smooth but decreases by about 14 percent over the course of the spill, which indicates that the spills were not terribly non-uniform.

The incident beam was attenuated by interactions as it passed through the target, so not all of the beam was incident upon the entire target length. The resulting thick target correction factor is estimated to be 0.97, based upon the absorption length of the beryllium target.

The events that were recorded during the damaged spills do not have scaler records, and since these events were included in the charm search, a correction factor of 1.004 was introduced.

The contamination of the beam by particles other than pions is ignored. The contribution of accidental coincidences between B1 and B2 is also neglected. The net correction factor for the beam flux is 1.10. The total number of incident live beam particles employed in this study is estimated to be 2.95×10^{11}.

5.2 DST CUTS

The information available on the DST's makes possible the generation of a variety of invariant mass plots. The major drawback of the mass plot technique is that the invariant mass of all valid particle combinations in each selected event must be calculated and entered into the plot, and generally only a tiny fraction of those combinations arise from the daughters of a decay of interest. The other combinations contribute to a background that can easily obscure a small signal. The prompt muon trigger combined with the muon pass

attempted to isolate those events that contained a candidate muon in the trigger arm. This section describes additional criteria that were invoked to remove or "cut" certain events from further consideration in an attempt to selectively suppress background relative to signal. Cuts were invoked on entire runs, events, and individual tracks.

A few of the runs that were processed and written to the DST were excluded from the analysis described in this chapter due to concerns about the quality of those individual runs. Most of the excluded runs had hardware problems that were detected while the runs were in progress. Approximately 22 500 prompt muon triggers were eliminated by this cut. The events employed in this DST charm search were distilled from runs representing 1 758 663 prompt muon triggers and including 31 944 pre-scaled beam triggers.

All forward arm tracks that had momenta above 250 GeV/c were excluded from contributing to any of the mass plots displayed in this chapter.

5.2.1 Clean Vertex Cut

In order to achieve reasonable mass resolution, the location of the interaction vertex must be well identified. Figure 31(a) shows the distribution of the number of unblemished vertex clusters in the DST events. Distributions of the number of unblemished single-chamber and multi-chamber vertex cluster are presented in figures 31(b)

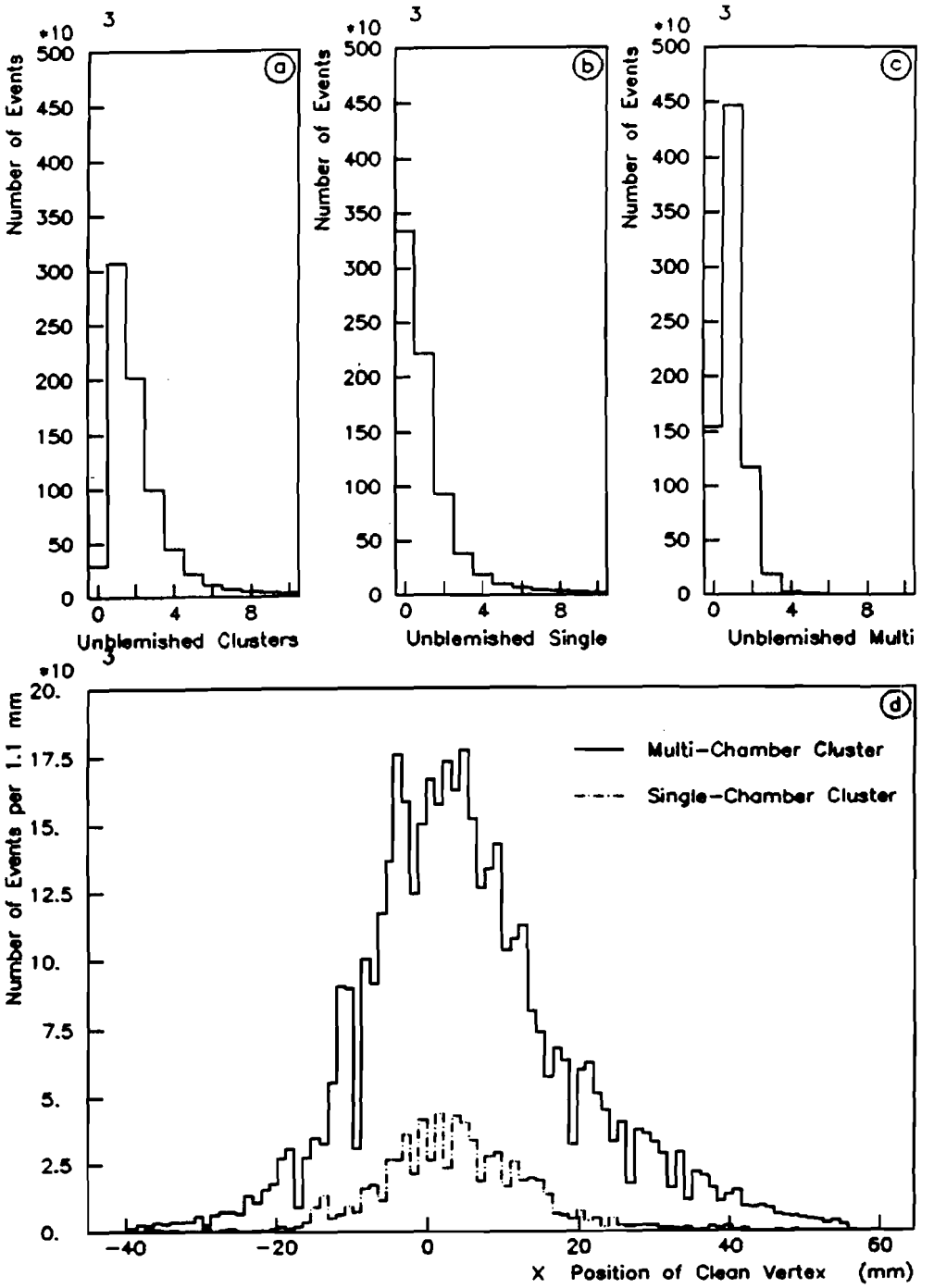

FIGURE 31. Interaction vertex selection. (a) The number of unblemished vertex clusters per event. (b) The number of unblemished single-chamber clusters per event. (c) The number of unblemished multi-chamber clusters per event. (d) X position of the interaction vertex for those events that survive the clean vertex cut.

and 31(c). Due to the number of vertex clusters per event, it was not always possible to reliably distinguish the interaction vertex from the other unblemished vertex clusters in the event. A cut was implemented, referred to as the "clean vertex cut," that excluded some of those events whose vertex selection was subject to confusion. The clean vertex cut requires that the event have at least one unblemished vertex cluster, and no more than five unblemished multi-chamber vertex clusters. Furthermore, the cluster selected as the interaction vertex cluster must be unblemished. If the selected cluster is a multi-chamber cluster, it must have at least two more UPMX matchups than any other unblemished multi-chamber cluster in that event, and it must have at least one more UPMX matchup than any unblemished single-chamber cluster in that event. If the selected cluster is a single-chamber cluster, there must be no more than five unblemished single-chamber clusters in the event, and the mean number of UPMX matchups per forward arm track must be at least 0.49 for the selected cluster. Furthermore, if a single-chamber cluster was selected, all unblemished multi-chamber clusters must have at least one beam tag and at least two fewer UPMX matchups than the selected single-chamber cluster. All other unblemished single-chamber clusters must also have at least one fewer UPMX matchup than the selected single-chamber cluster.

If the event failed to meet any of the above requirements, it was rejected by the clean vertex cut. About 69 percent of the DST events survive the clean vertex cut. Approximately 56 percent of the events

that survive the clean vertex cut have only one unblemished vertex cluster. Of the events that satisfy the clean vertex requirements, 86 percent employed a multi-chamber vertex cluster to determine the interaction vertex location. The X position of the vertex for the events surviving the cut is illustrated in figure 31(d). Based upon studies of the UPMX matchup criteria employed in the clean vertex cut, 96 percent of the events that survive the cut are anticipated to have their vertex position properly identified.

5.2.2 Forward Arm Track Quality Cut

The distribution of the number of forward arm tracks per event, which has a mean of 6.2, is shown in figure 32(a). The momentum distribution of the negatively charged forward arm tracks is presented in figure 32(b), while the momentum distribution of the positively charged tracks is shown in figure 32(c). The transverse momentum distributions of the charged forward arm tracks are shown in figures 32(d) and 32(e).

All the forward arm tracks have a minimum of four hits from among the six downstream X chambers, two hits from the four Y chambers, and at least one hit from among the three rotated chambers. These minimal hit requirements admit tracks of questionable quality. As a result, a cut was devised, called the "track quality cut," which excludes a track from participation in invariant mass combinations if any of the following conditions is satisfied:

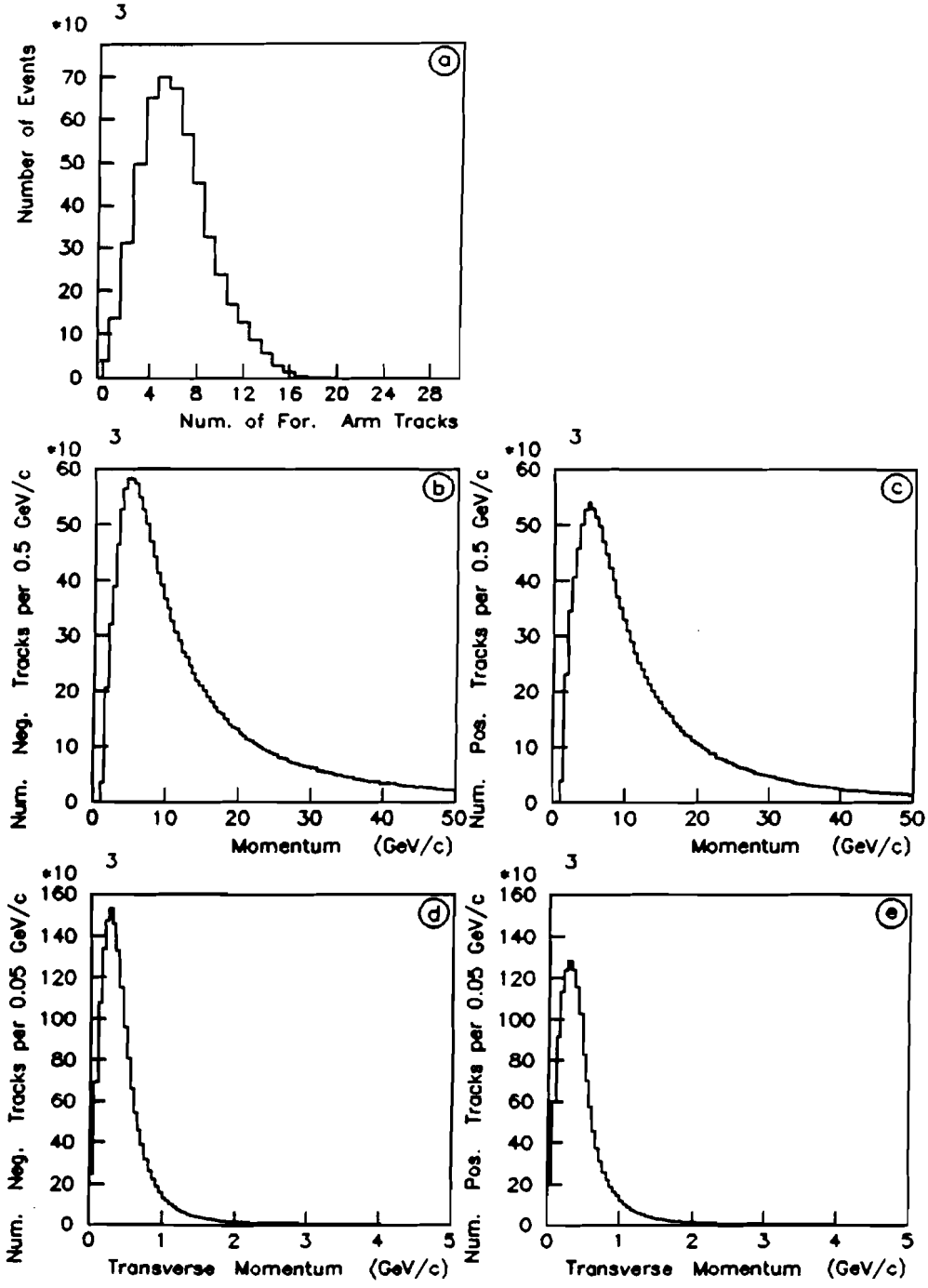

FIGURE 32. Forward arm track distributions. (a) Number of forward arm tracks per event. (b) Momentum distribution of the negatively charged forward arm tracks. (c) Momentum distribution of the positively charged forward arm tracks. (d) Transverse momentum distribution of the negatively charged forward arm tracks. (e) Transverse momentum distribution of the positively charged forward arm tracks.

1. The track has one rotated hit and one downstream Y hit.
2. The track has one rotated hit, four X hits, and no hit in UPMX.
3. The track has two rotated hits, one downstream Y hit, four X hits, but no hit in UPMX.

This cut rejects approximately 12 percent of all forward arm tracks. The mean number of forward arm tracks that survive the track quality cut is 5.9 per clean vertex DST event.

5.3 PARTICLE IDENTIFICATION ALGORITHMS

In order to calculate the invariant masses of combinations of tracks, the masses of the particles that generated the tracks must be established or assigned. The LAC, the forward muon identifier, and the Cherenkov counter could be employed to provide guidance in making these particle mass assignments. Since only decay modes in which all participating particles were charged were investigated in this analysis, the LAC could only be effectively employed to separate electrons from other charged particles. There were relatively few electrons detected [94], and none of the decay modes under study employed electrons, so the information from the LAC was neglected. The forward muon identifier was only employed in dimuon mass plots, and was not used to reject a particle as a candidate hadron due to the possibility of accidental matchups, and the possibility that the hadron decayed into a final state that included a muon before being

absorbed in the filter. Thus, the Cherenkov counter provided the primary guidance for particle identification in this analysis. Recall that the Cherenkov analysis performed in generating the DST calculated PROBK, which is a variable primarily aimed at separating pions from kaons. Due to the Cherenkov radiation thresholds of pions and kaons, this Cherenkov identification was only employed for those tracks whose momenta was in the range of 7 to 20 GeV/c. Those tracks that intersected the Cherenkov counter within its active area, and whose momenta were between 7 and 20 GeV/c are said to be in the "discrimination domain" of the Cherenkov counter.

Several different particle identification schemes were employed. The first scheme, referred to as the BLIND identification scheme, neglected the data from the Cherenkov counter and simply made every hypothesis for the various particle identities which could contribute combinations to the mass plot under study. This scheme led to tremendous backgrounds, but it introduced no particle identification inefficiency.

Another particle identification scheme employed, referred to as CONCER identification, made every hypothesis for each particle's identity which was consistent with the Cherenkov counter data in the following manner. If the track was in the discrimination domain of the Cherenkov, and it was isolated, and had a PROBK2 less than 0.1, then that track was only assigned a pion or less massive particle identity in the CONCER scheme. If an isolated track within the discrimination domain had a PROBK1 greater than or equal to 0.8, then

that track was only assigned a kaon or more massive particle identity in this scheme. All other tracks were assigned all possible identities which formed combinations that contributed to the mass plot under consideration. In this way, every combination employed in the mass plot was consistent with the particle identification data available from the Cherenkov counter. According to the results of the Cherenkov efficiency studies described in the fourth chapter, an isolated pion in the discrimination domain had a 91.2 percent probability of being only identified as a pion by this scheme, and a 0.6 percent probability of being only misidentified as a kaon. An isolated kaon in the discrimination domain had a 68.9 percent probability of being only identified as a kaon, and a 9.1 percent probability of being only misidentified as a pion. Although this scheme lowered the combinatorial background in the mass plots, it also introduced a slight particle identification inefficiency.

In the third particle identification scheme, referred to as the CER scheme, kaons or more massive particles were defined to be any particles that were in the discrimination domain of the Cherenkov and had a PROBK2 greater than a specified value, referred to as the "PROBK level." All other particles were labeled as pions or less massive particles. This scheme dramatically lowered the acceptance of the spectrometer by requiring the kaon to be in the discrimination domain, but for reasonable choices of the PROBK2 level, the kaons in the discrimination domain were seldom misidentified.

5.4 STANDARD STATES

A demonstration of the forward arm spectrometer's capabilities is provided by the reconstruction of several non-charmed particle states. Only events that survive the clean vertex cut contribute to the mass plots shown in this section. Furthermore, all tracks that contribute to the mass plots presented in this section are required to satisfy the track quality cut.

Figure 33 shows the invariant mass plot of all opposite sign pairs that are identified as kaons by the CER scheme with the PROBK2 level at various values. The mass plot that requires PROBK2 greater than or equal to 0.0 effectively only requires that the contributing tracks be in the discrimination domain of the Cherenkov, and that plot has no obvious mass peak, although it does have a shoulder. However, as the PROBK2 level required to identify a kaon is raised, a clear and significant mass peak is observed at a mass of 1.020 GeV/c^2. As the PROBK2 level is increased, the signal to background ratio in the peak also increases but the number of combinations in the peak decreases. When the PROBK2 level is increased above 0.5, the statistical significance of the peak decreases. The K^+K^- mass plots were fit to a Gaussian plus a fourth order polynomial. For the mass plot with the PROBK2 level at 0.5, the mean of the Gaussian is at 1.0199 ± 0.0005 GeV/c^2, and the standard deviation is 0.0043 ± 0.0006 GeV/c^2. This mass peak is interpreted as evidence of ϕ meson production since both the mean mass and the measured width of

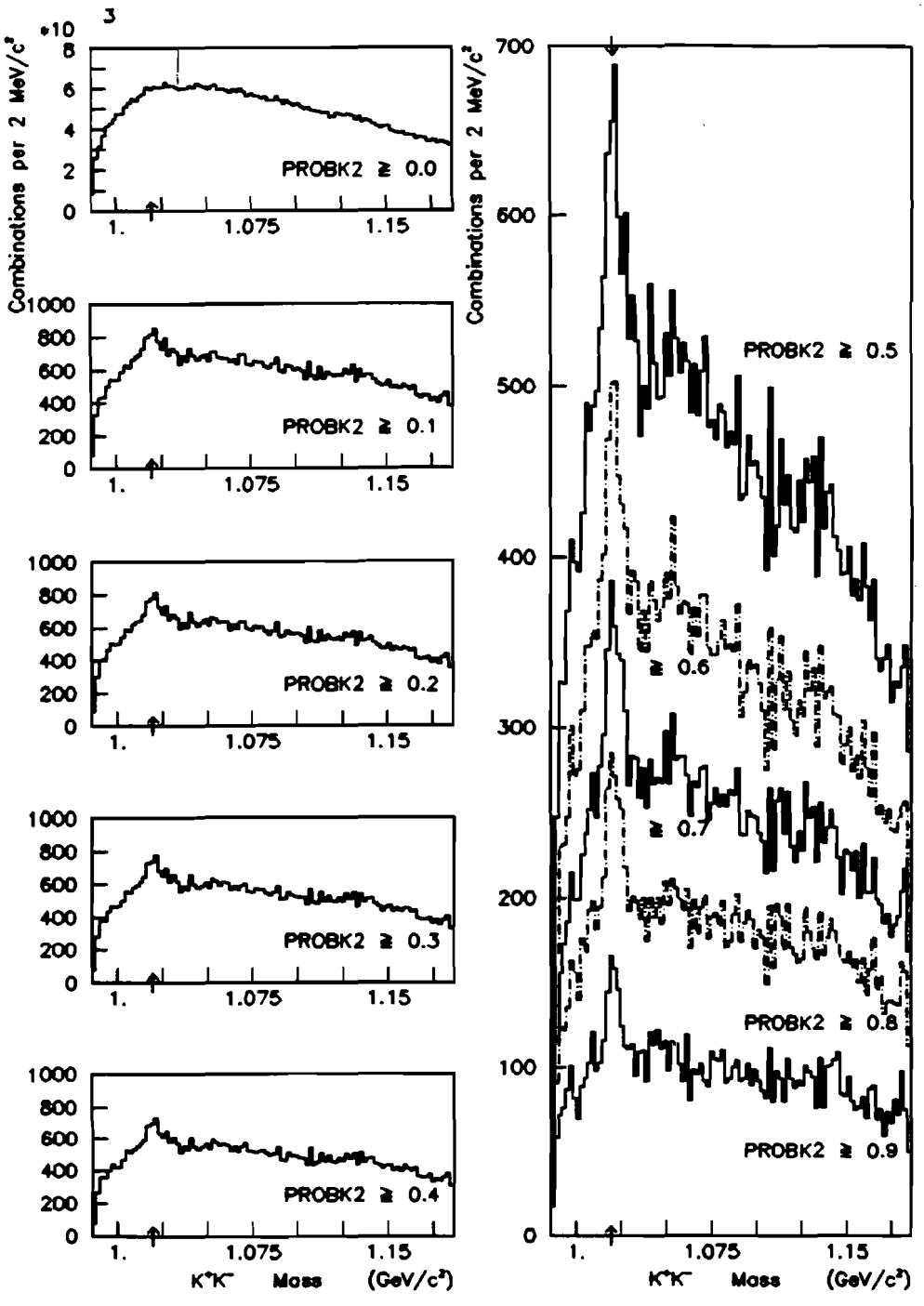

FIGURE 33. Invariant mass plots of oppositely charged pairs of tracks identified as kaons by the CER identification scheme for a variety of PROBK2 levels.

the peak are consistent with Monte Carlo expectations for the ϕ meson. The ϕ meson has a mass of 1.019513±0.000069 GeV/c^2, a natural width of 0.00422±0.00013 GeV/c^2, and a branching ratio to decay into a pair of opposite sign kaons of 0.493±0.010 [70]. (The small broad enhancement around 1.130 GeV/c^2 in the K^+K^- mass plots with low PROBK requirements is interpreted as a kinematic reflection of the $K^*(890)$.)

The mass plot of all $K^+\pi^-$ pairs identified by the CONCER scheme is shown in figure 34(a). The corresponding mass plot of all $K^-\pi^+$ pairs identified by the CONCER scheme is shown in figure 34(b). These mass plots exhibit evidence of the production of the neutral $K^*(890)$. The neutral $K^*(890)$ has a mass of 0.89645±0.00037 GeV/c^2 [70]. Mass plots of the $K^+\pi^-$ and $K^-\pi^+$ pairs as identified by the CER scheme with the PROBK2 level at 0.7 are shown in figure 34(c). (For final states involving only a single kaon, a PROBK2 level of 0.7 was employed because of the additional suppression of misidentified pions provided by this more stringent PROBK requirement.) Evidence of the neutral $K^*(890)$ is clear.

The data gathered by the LAC was employed to make invariant mass plots of two photon states, and clear π^0 and η signals were observed. The neutral pions were combined with the charged pions to yield evidence for the $\pi^+\pi^-\pi^0$ decay mode of the $\omega(783)$, as well as the two pion decay mode of the negatively charged ρ [95].

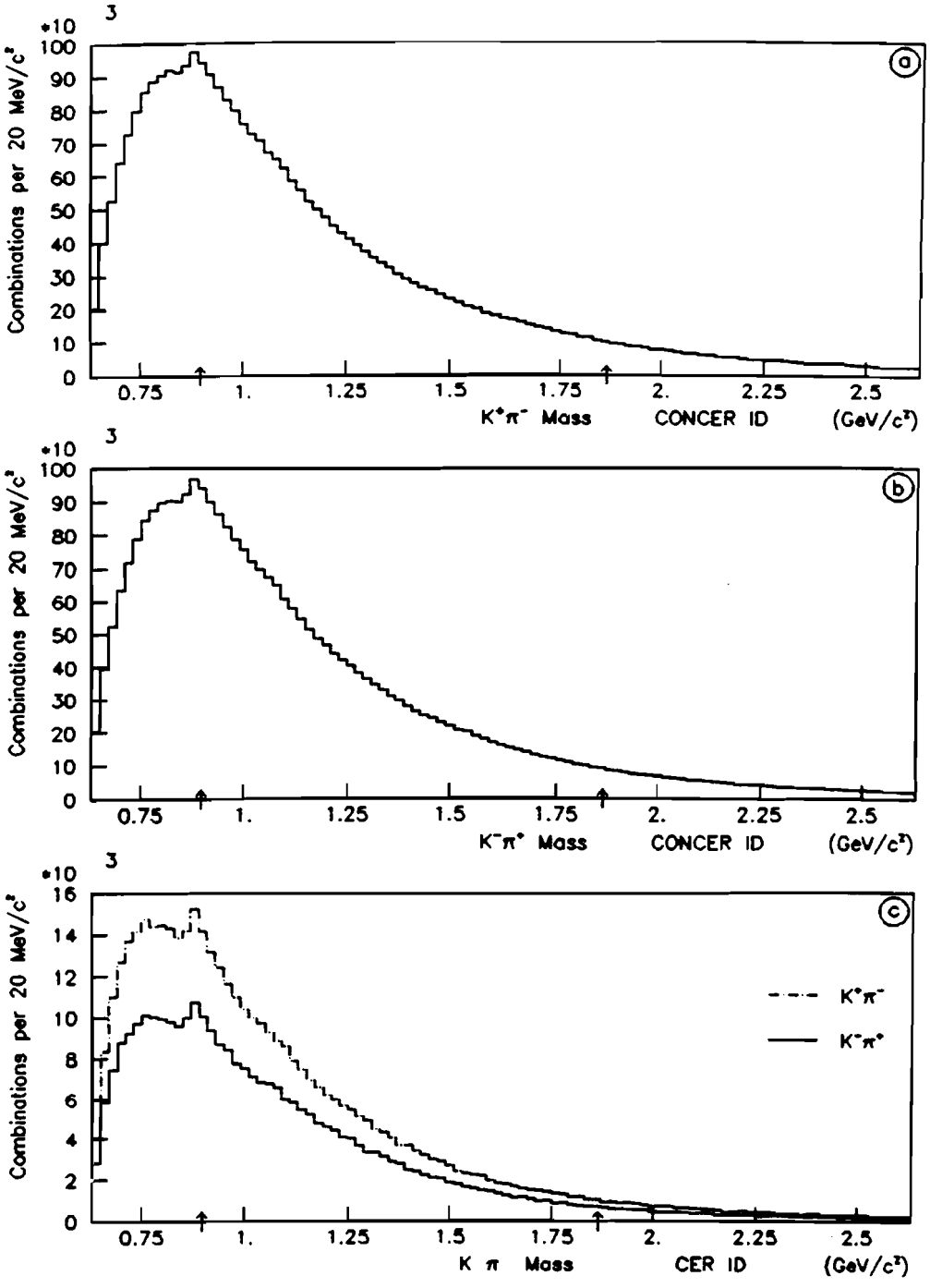

FIGURE 34. $K^+\pi^-$ and $K^-\pi^+$ invariant mass plots. (a) $K^+\pi^-$ identified via the CONCER scheme. (b) $K^-\pi^+$ identified via the CONCER scheme. (c) Particles identified via the CER scheme with the PROBK2 level at 0.7.

5.5 TRIGGER ARM MUON DEFINITION AND CUTS

This section describes additional requirements imposed upon the trigger arm data to reject accidental tracks, halo muons, and events with multiple trigger arm muons of opposite charge.

About 0.7 percent of the clean vertex DST events have more than 19 valid M1 points, and in order to limit the confusion in the selection of the upstream trigger arm segment, these events are excluded from contributing to the charm search mass plots.

For an event to be represented on the DST, the trigger arm data associated with that event must have trigger hodoscope latches set that are consistent with the prompt muon trigger logic. The events written on the DST were also required to have at least one downstream trigger arm track, which is defined by a minimum of two out of a possible three X hits, two out of three Y hits, and one out of two rotated hits. A trigger arm track is considered a muon if it satisfies all of the following additional requirements:

1. If the downstream track extrapolates through an M2 or M3 hodoscope element, that element must be latched. Allowances for multiple scattering and extrapolation uncertainty are made. Approximately 90 percent of the clean vertex DST events have at least one trigger arm track that satisfies this requirement.

2. The downstream track must have at least one rotated hit on the track within a tighter search window of ±1.5 cm for MUU3 and ±3.0 cm for MUV4. About 96 percent of the clean vertex DST events have at least one trigger arm track that meets this condition.

3. The downstream track must employ a hit in at least one of the two PWC's downstream of the downstream trigger arm absorber. This condition is satisfied by at least one track in 92 percent of the clean vertex DST events.

4. The difference between the extrapolated upstream and downstream track positions at the magnet midplane must be less than or equal to ±0.25 m in both X and Y. Only 77 percent of the clean vertex DST events have a track that satisfies this condition.

5. The upstream and downstream track matchup must satisfy loose chi-squared cuts. About 99 percent of the clean vertex DST events have a track that satisfies this condition.

6. The simple bend determination of the track's charge must be consistent with the charge determined by the iterative fit for the track's momentum. Almost all of the clean vertex DST events have at least one track that meets this condition.

Approximately 64 percent of the DST events with a clean vertex have at least one trigger arm track that is a muon by the above definition. The distribution of the number of trigger arm muons in each clean vertex DST event is shown in figure 35(a). The mean number of trigger arm muons is 0.8 per clean vertex DST event.

To enhance the likelihood that a muon was indeed responsible for the prompt muon trigger and that the triggering muon came from an interaction in the target, additional requirements were made upon each event employed in the charm search mass plots. For an event to contribute to the charm search mass plots, at least one of the trigger arm muons identified by the above cuts must also satisfy all of the following requirements:

1. The downstream track associated with the muon must extrapolate through M2 and M3 hodoscope elements that are consistent with a triggering road. About 93.1 percent of the clean vertex DST events with a muon also satisfy this requirement.

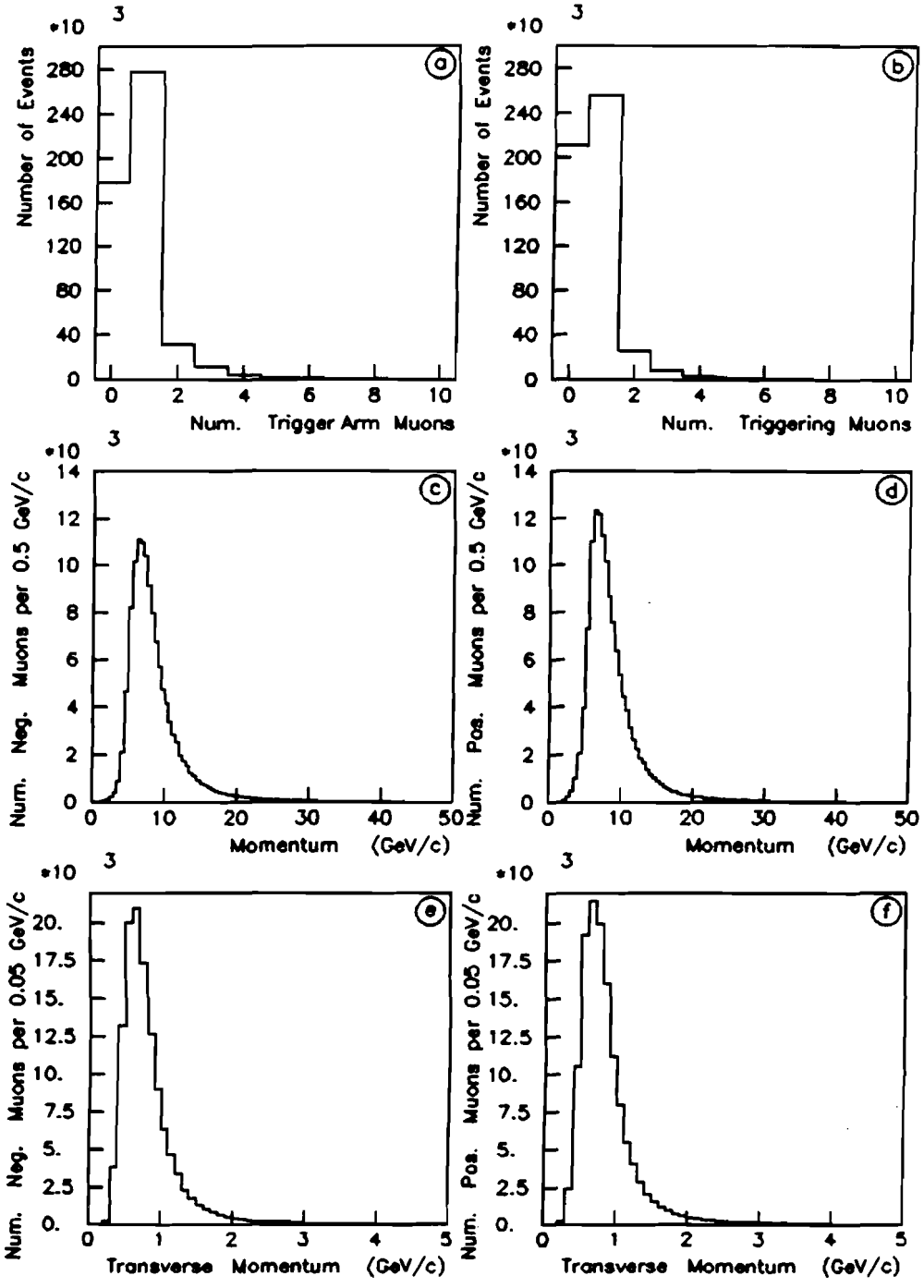

FIGURE 35. Trigger arm muon distributions. (a) Number of trigger arm muons per event. (b) Number of triggering muons per event. (c) Momentum distribution of the negative triggering muons. (d) Momentum distribution of the positive triggering muons. (e) Transverse momentum distribution of the negative triggering muons. (f) Transverse momentum distribution of the positive triggering muons. (Events with more than one triggering muon are excluded from the momentum distribution plots.)

2. The momentum of the muon must be less than or equal to 50 GeV/c. Of the clean vertex DST events which contain a muon, about 98.3 percent meet this requirement.

3. The muon must not be identified as a halo muon, that is, either the downstream YZ slope of the muon is greater than 0.015, or the downstream XZ slope of the muon is outside the range of -0.012 to +0.010. About 98.1 percent of the clean vertex DST events with a muon also satisfy this requirement.

About 58 percent of the clean vertex DST events have at least one such muon referred to as a "triggering muon." Figure 35(b) shows the distribution of the number of triggering muons in each clean vertex DST event. The mean number of triggering muons is 0.7 per clean vertex DST event.

Of the clean vertex DST events with a triggering muon, 87 percent have only one such muon, and the momentum and transverse momentum distributions for those triggering muons are shown in figure 35(c) through 35(f). There are about 6.7 percent more positive single triggering muons than negative single triggering muons.

The mean number of events with a fully reconstructed triggering muon per livetime BEAM is 1.62×10^{-6}, and the ratio is shown for individual runs in figure 36. These numbers have been corrected to account for the vertex identification inefficiency, but not the trigger arm PWC inefficiency.

A special run was recorded with the beryllium target removed, and the data was processed in the same manner as the standard data. The resulting number of prompt muon triggers per BEAM for the target-out run represented 17.6 percent of the target-in rate. The efficiency corrected number of events with a fully reconstructed triggering muon

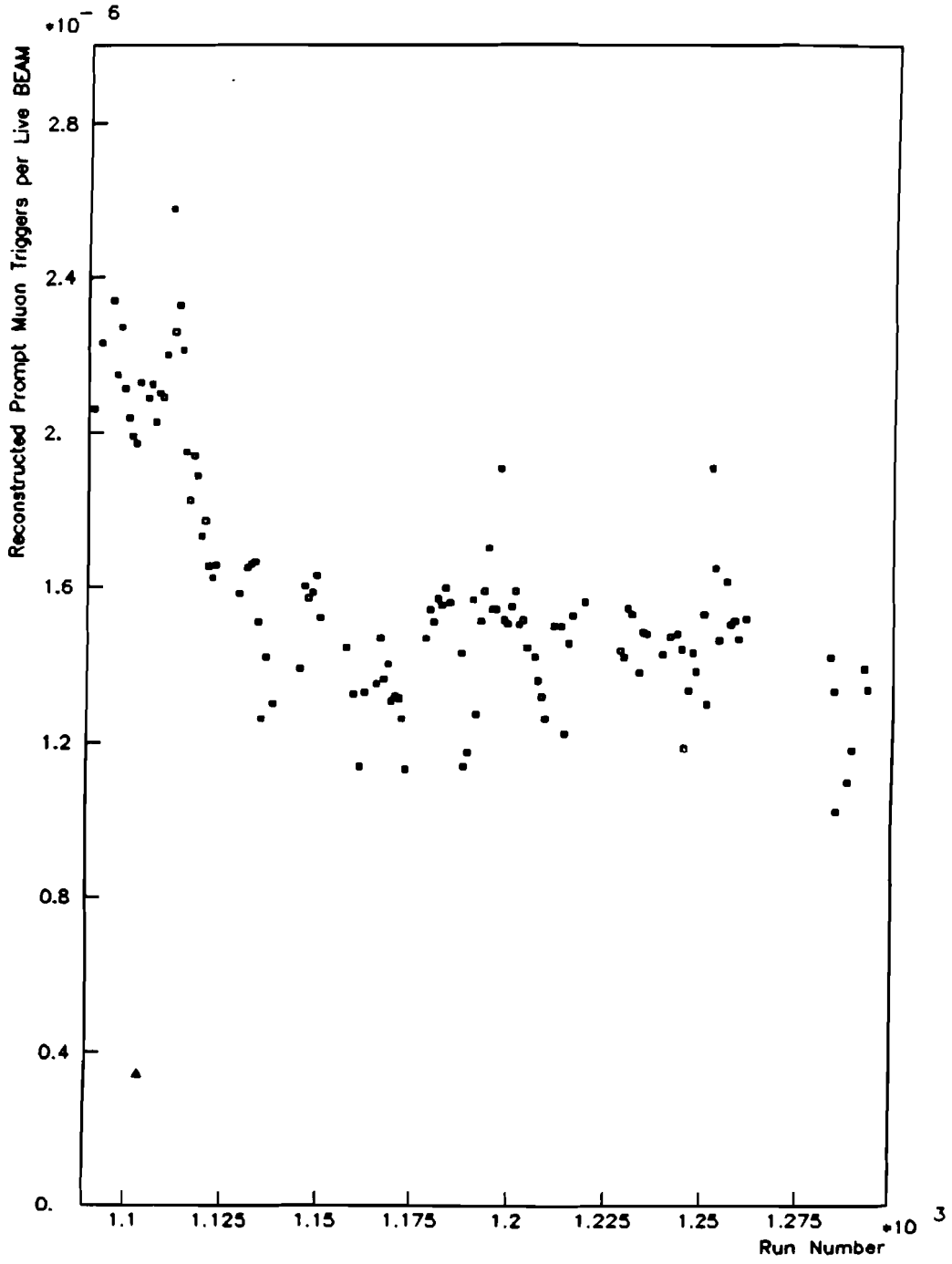

FIGURE 36. The ratio of the number of prompt muon triggered events with at least one reconstructed triggering muon to the number of live BEAM, for all runs employed in the charm search. (Corrections have been made for detector inefficiencies with the exception of trigger arm PWC inefficiencies.)

per BEAM for the target-out run was 16.7 percent of the corresponding target-in rate. These results imply that the beryllium was indeed the primary target in the interactions, but some of the interactions occurred in the surrounding material, such as B1 and B2.

5.6 CHARM SEARCH INVARIANT MASS PLOTS

Under the assumption that the triggering muon originated from the associated production of a charm anticharm quark pair followed by the semileptonic decay of the charmed or anticharmed state, the sign of the triggering muon can place restrictions upon the identity of the particles in the decay products of the partner state (in the absence of $D^0\overline{D}^0$ mixing). For instance, in searching for evidence of the neutral D meson decaying into a charged kaon and one or three charged pions, the sign of the kaon should be the same as the sign of the triggering muon. A similar situation arises for the case of the charged D meson decaying into a charged kaon and two charged pions. This correlation between the triggering muon sign and the charge of the kaon allows one to separate the mass plots into right-sign and wrong-sign mass plots.

To contribute to any of the charm search mass plots described in this section, an event must have been successfully processed by the event reconstruction programs described in the third chapter. Furthermore, the event must satisfy the clean vertex cut and have at

least one triggering muon. To take advantage of the right-sign and wrong-sign classification of the mass plots, an event is employed in the charm search only when all muons in the trigger arm for that event have the same sign (excluding halo muons and muons with momenta greater than 50 GeV/c). This requirement eliminates 1.2 percent of the clean vertex DST events that have at least one triggering muon. A total of 290 708 events satisfy all the above requirements, and are employed in the charm search mass plots. In addition, unless explicitly stated otherwise, the track quality cut is imposed upon all forward arm tracks employed in the charm search mass plots presented.

Of the events employed in this charm search, 51.67 percent have positive triggering muons. Thus there is a small but statistically significant trigger charge asymmetry in this data.

5.6.1 Kπ Invariant Mass Plots

The neutral D meson decays into a charged kaon and a charged pion with a branching ratio of 0.049±0.009±0.005 [96], so one can search for evidence of D meson production in the Kπ invariant mass plots. The invariant mass plots of all right-sign $K^+\pi^-$ and $K^-\pi^+$ combinations with the particles identified by the CONCER scheme are shown in figure 37. That figure also shows the sum of all right-sign Kπ pairs with a polynomial fit superimposed. The Kπ combinations with mass between 1.795 and 1.935 GeV/c^2 were excluded from contributing to the

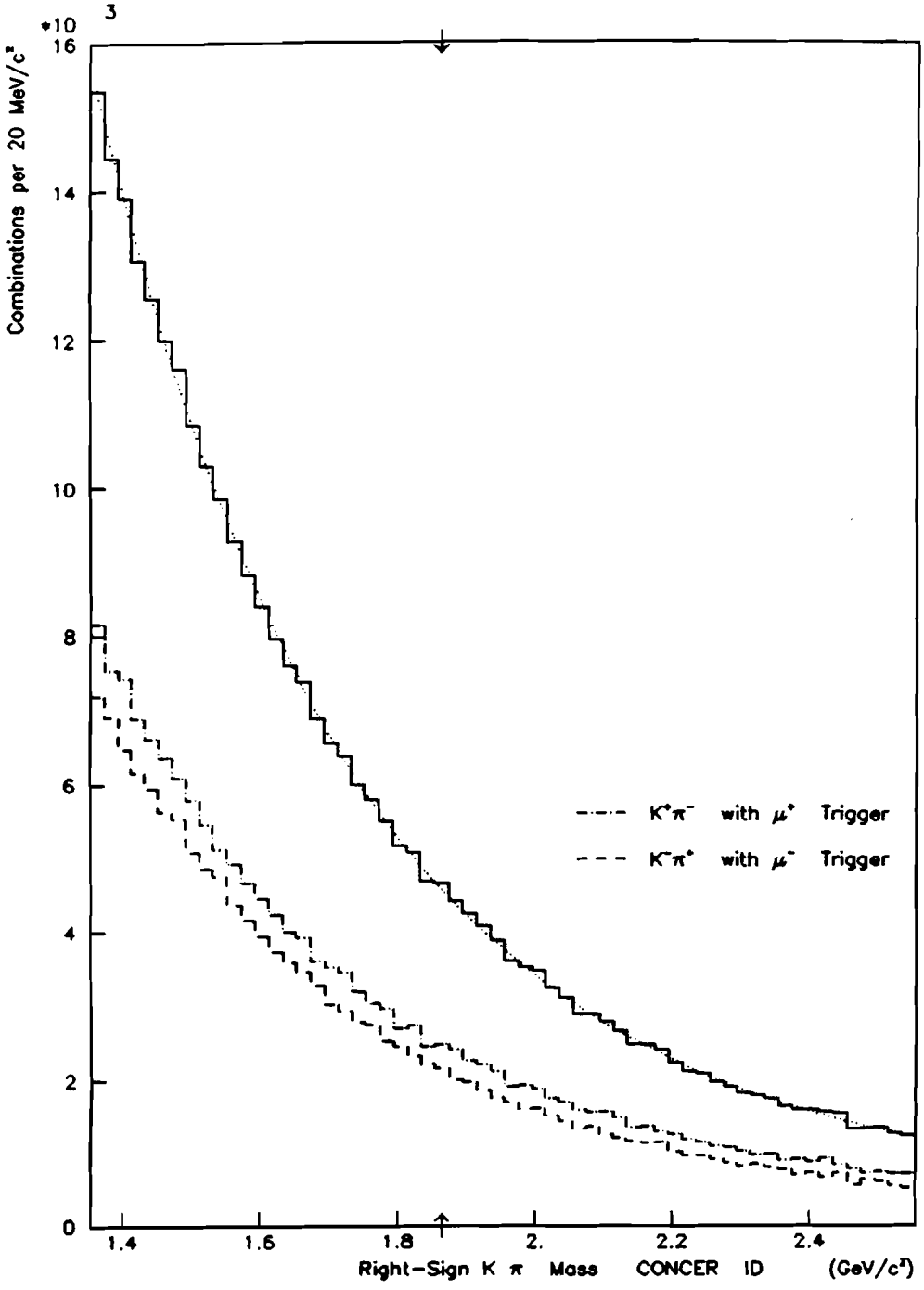

FIGURE 37. Right-sign $K^+\pi^-$ and $K^-\pi^+$ invariant mass plots. Particles are identified by the CONCER scheme. The sum of the two right-sign mass plots was fit to a polynomial. The entries in the vicinity of the D mass were excluded from the fit.

fit that determined the polynomial. There is no significant enhancement in the vicinity of the neutral D meson mass, which is 1.8647 ± 0.0006 GeV/c^2 [70].

The inset in figure 38 shows the distribution of the cosine of the angle between the direction of the kaon in the Kπ center of momentum frame and the direction of the Kπ pair in the laboratory, for those Kπ pairs that have a mass between 1.815 and 1.915 GeV/c^2. This angle is referred to as Θ_{CM}. The tracks employed in this plot are identified via the CONCER scheme. This $\cos(\Theta_{CM})$ plot clearly shows that many of the high mass combinations arise from pairs that include a very forward or very backward kaon. Since the D is a pseudoscalar meson, the $\cos(\Theta_{CM})$ distribution for kaons coming from Kπ decays of neutral D mesons should be uniform. The acceptance of the spectrometer introduced greater losses for those Kπ pairs that had large forward or backward kaon angles. Thus cutting out the Kπ pairs that have $\cos(\Theta_{CM})$ less than -0.7 or greater than or equal to +0.7 should improve the opportunity to observe a charm signal. Figure 38 shows the right-sign Kπ mass plot with this $\cos(\Theta_{CM})$ cut applied. The cut fails to reveal a significant enhancement in the vicinity of the D mass.

The mass plots of all right-sign Kπ combinations as identified by the CER scheme with the PROBK2 level at 0.7 are shown in figure 39. Although the background level has been reduced by imposing the CER identification, the D acceptance has also dropped and there is still no obvious enhancement. The corresponding wrong-sign Kπ mass plots

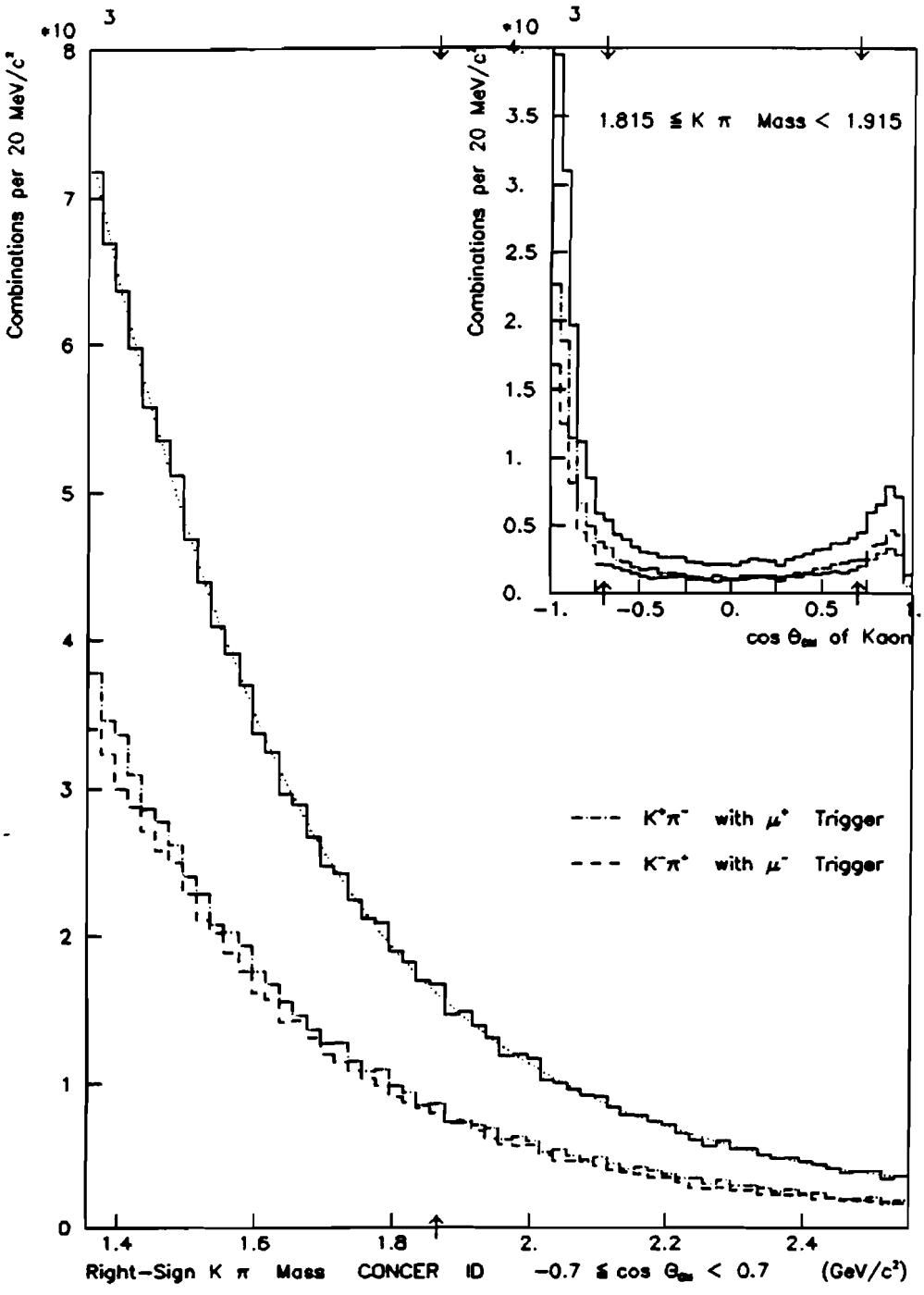

FIGURE 38. Right-sign $K^+\pi^-$ and $K^-\pi^+$ invariant mass plots with a cut applied on the angle between the kaon in the center of momentum frame of the $K\pi$ system and the $K\pi$ direction in the lab. The sum of the two right-sign mass plots is fit to a polynomial. The inset shows the distribution of the cosine of that angle for those $K\pi$ combinations with mass in the range of 1.815 to 1.915 GeV/c^2. Particles are identified by the CONCER scheme.

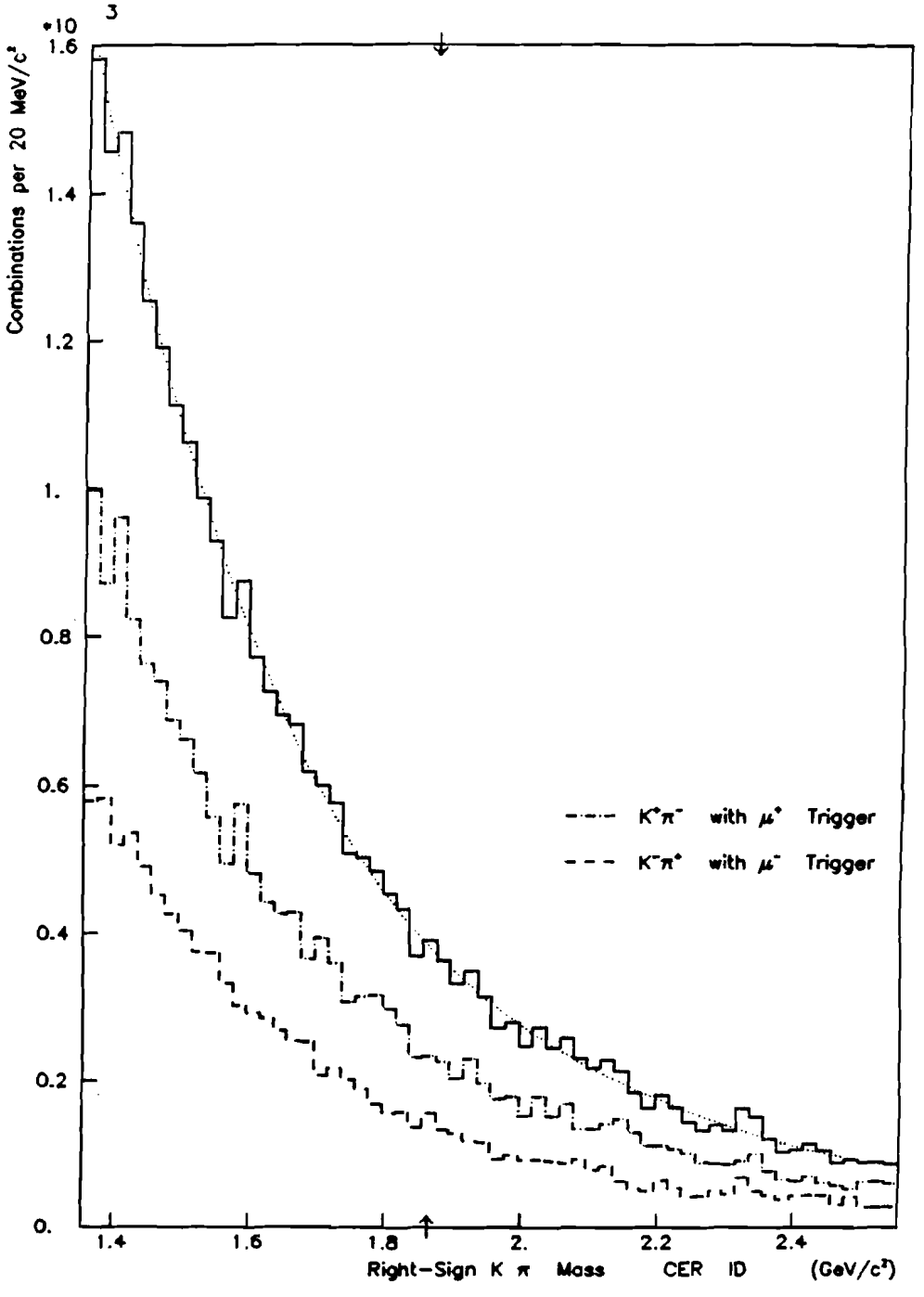

FIGURE 39. Right-sign $K^+\pi^-$ and $K^-\pi^+$ invariant mass plots. Particles are identified by the CER scheme with the PROBK2 level at 0.7. The sum of the two right-sign mass plots was fit to a polynomial. The entries in the vicinity of the D mass were excluded from the fit.

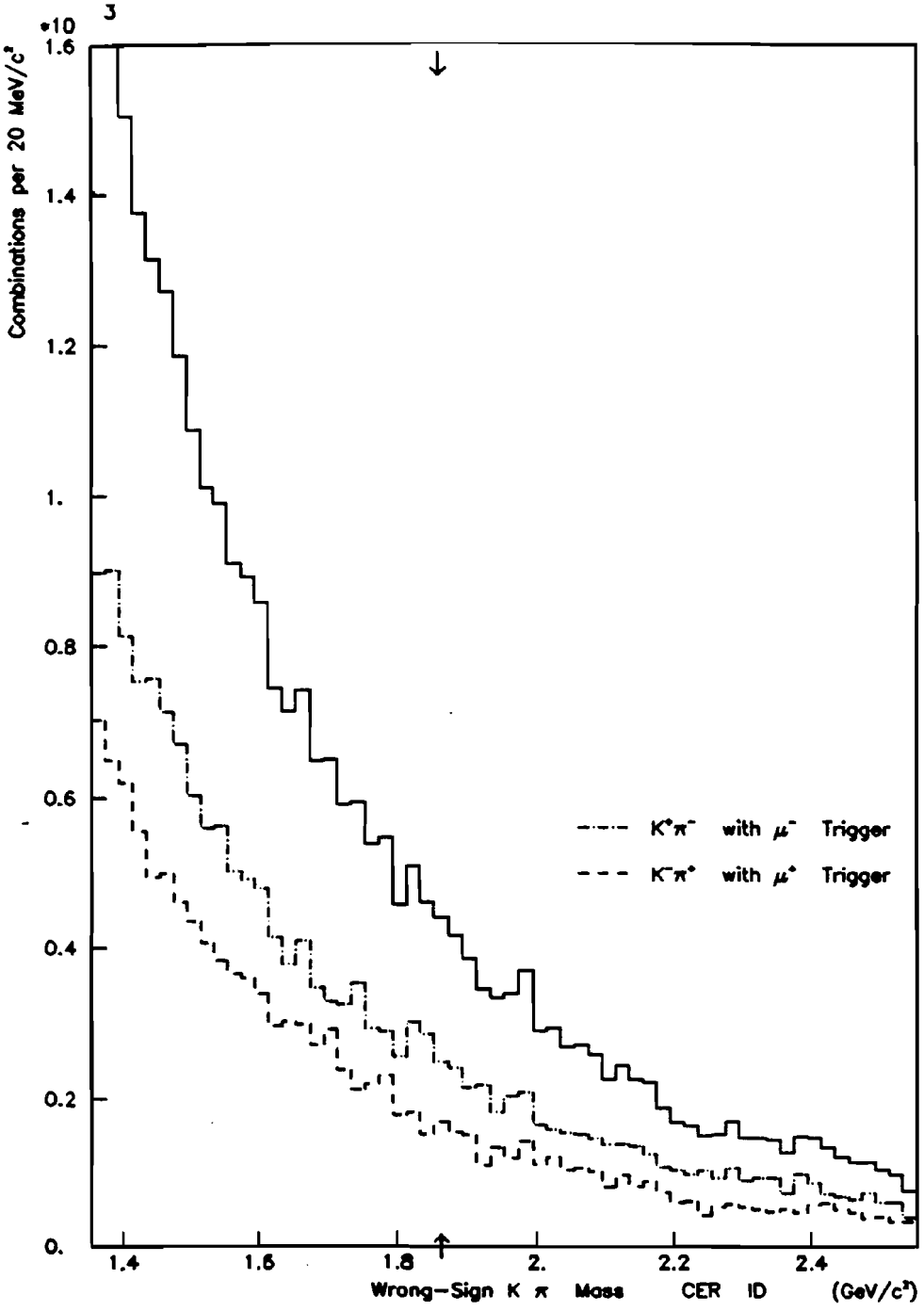

FIGURE 40. Wrong-sign $K^+\pi^-$ and $K^-\pi^+$ invariant mass plots. Particles are identified by the CER scheme with the PROBK2 level at 0.7. The sum of the two wrong-sign mass plots is also shown.

are shown in figure 40. Due to the momentum range cut imposed on the kaon by the CER identification scheme, the $\cos(\Theta_{CM})$ cut has lost most of its potency and is not presented here.

Additional cuts upon various kinematic variables associated with the $K\pi$ pairs and the triggering muons have failed to reveal any statistically significant bumps in the $K\pi$ mass plots in the region of the neutral D mass.

5.6.2 $K\pi\pi\pi$ Invariant Mass Plots

The neutral D meson also decays into a final state of one charged kaon and three charged pions, with a branching ratio of $0.075\pm0.012\pm0.014$ [96]. Though this branching ratio is larger than the branching ratio for the $K\pi$ decay mode of the D meson, the prospects for observing a signal are limited due to the tremendous combinatorial backgrounds, and the lower acceptances for the four body final state. The right-sign $K\pi\pi\pi$ mass plots are shown in figure 41. The particles are identified via the CER scheme with the PROBK2 level at 0.7. The background peaks near the D meson mass, and no significant signal is observed. In an attempt to isolate a signal, a variety of additional cuts were invoked upon the $K\pi\pi\pi$ mass plots without success.

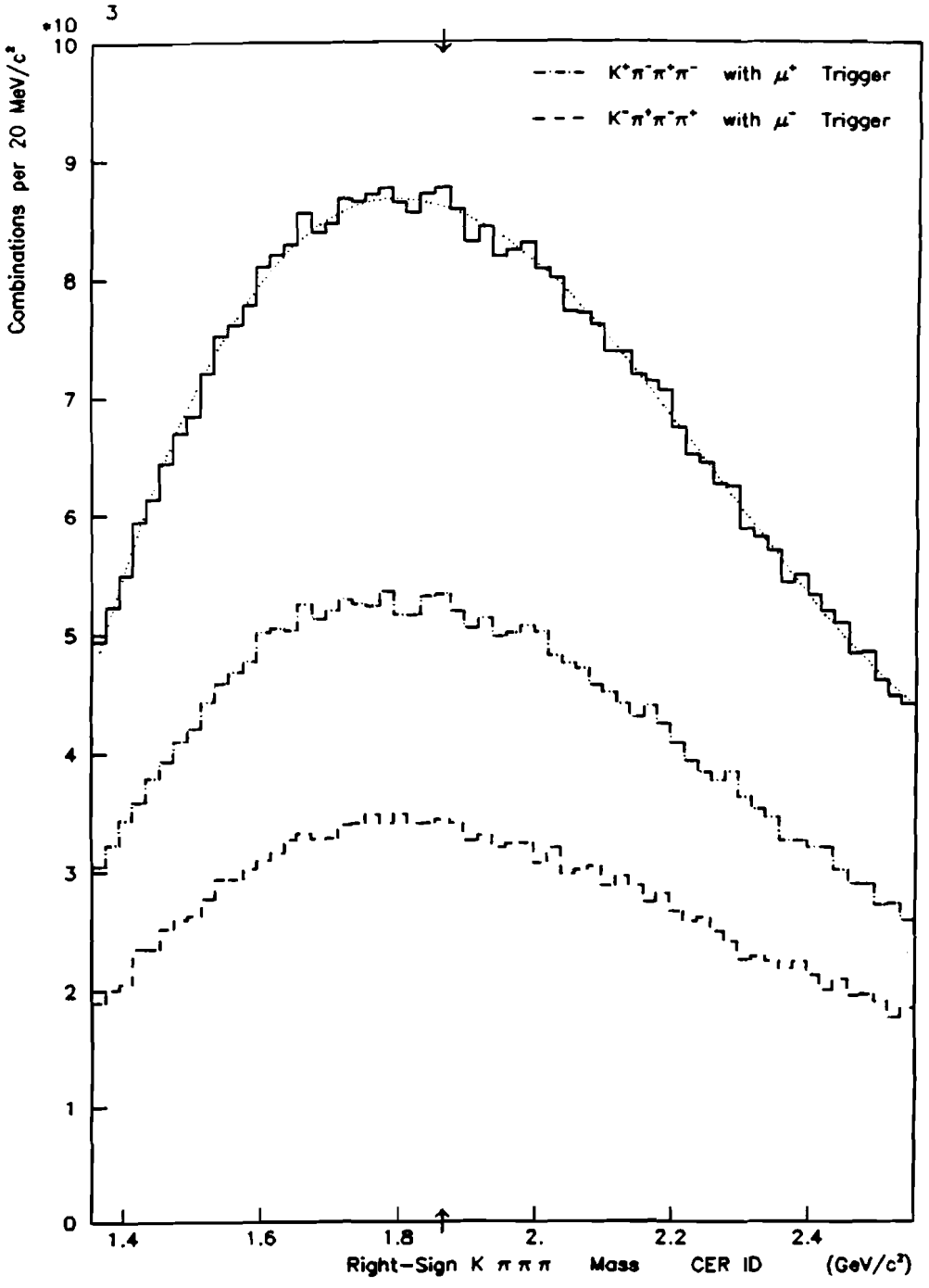

FIGURE 41. Right-sign $K^+\pi^-\pi^+\pi^-$ and $K^-\pi^+\pi^-\pi^+$ invariant mass plots. Particles are identified by the CER scheme with the PROBK2 level at 0.7. The sum of the two right-sign mass plots is fit to a polynomial.

The wrong-sign $K\pi\pi\pi$ mass plots are shown in figure 42. The particles are identified via the CER scheme with the PROBK2 level at 0.7.

5.6.3 $K\pi\pi$ Invariant Mass Plots

The charged D meson, which has a mass of 1.8694 ± 0.0006 GeV/c^2 [70], decays into two same sign pions and an opposite sign kaon with a branching ratio of $0.091\pm0.015\pm0.009$ [96]. Employing the CER particle identification scheme with the PROBK2 level at 0.7, the right-sign $K\pi\pi$ mass plots are shown in figure 43. No obvious excess is observed around the charged D mass. As with the other D meson mass plot searches, a variety of other cuts were invoked upon the data in an unsuccessful attempt to observe a statistically significant enhancement.

The wrong-sign $K\pi\pi$ mass plots are shown in figure 44. The particles are identified by the CER identification scheme with the PROBK2 level at 0.7.

5.6.4 Charged D^* Search

The charged D^* meson has a mass of 2.0101 ± 0.0007 GeV/c^2 [70], and it decays into a neutral D and a charged pion with a branching ratio of 0.489 ± 0.083 [97]. The mass difference between the charged D^* and

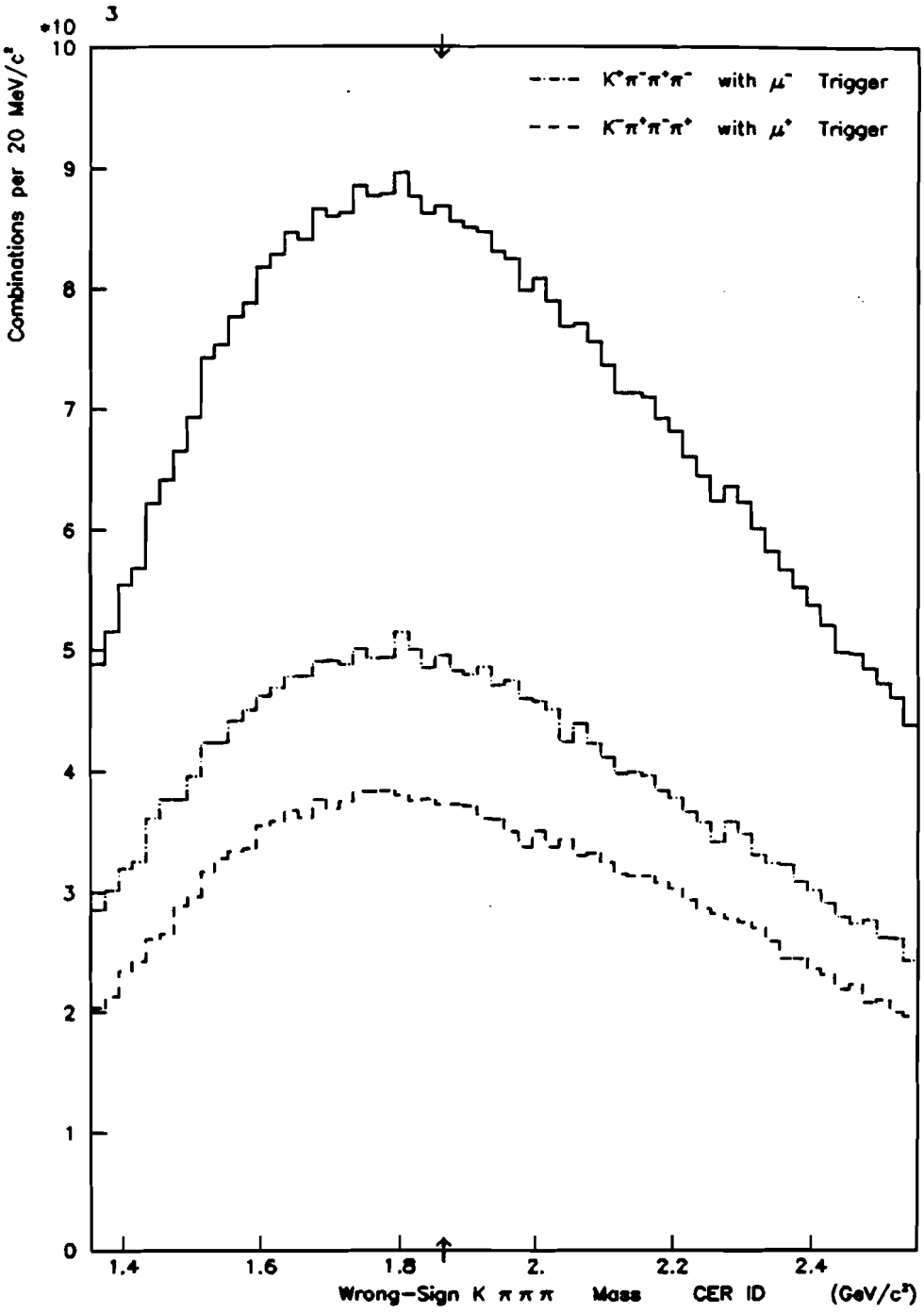

FIGURE 42. Wrong-sign $K^+\pi^-\pi^+\pi^-$ and $K^-\pi^+\pi^-\pi^+$ invariant mass plots. Particles are identified by the CER scheme with the PROBK2 level at 0.7. The sum of the two wrong-sign mass plots is also shown.

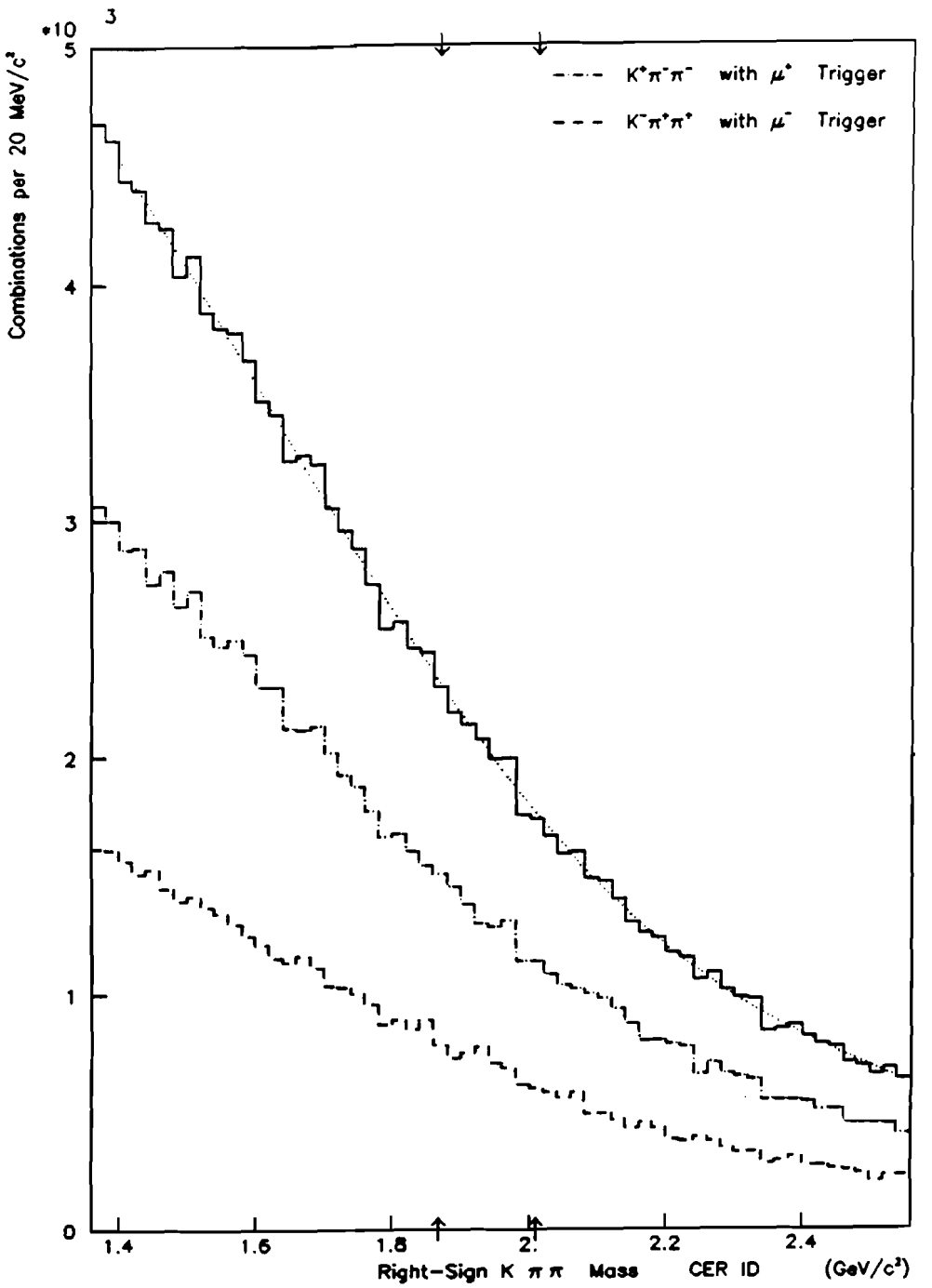

FIGURE 43. Right-sign $K^+\pi^-\pi^-$ and $K^-\pi^+\pi^+$ invariant mass plots. Particles are identified by the CER scheme with the PROBK2 level at 0.7. The sum of the two right-sign mass plots is fit to a polynomial.

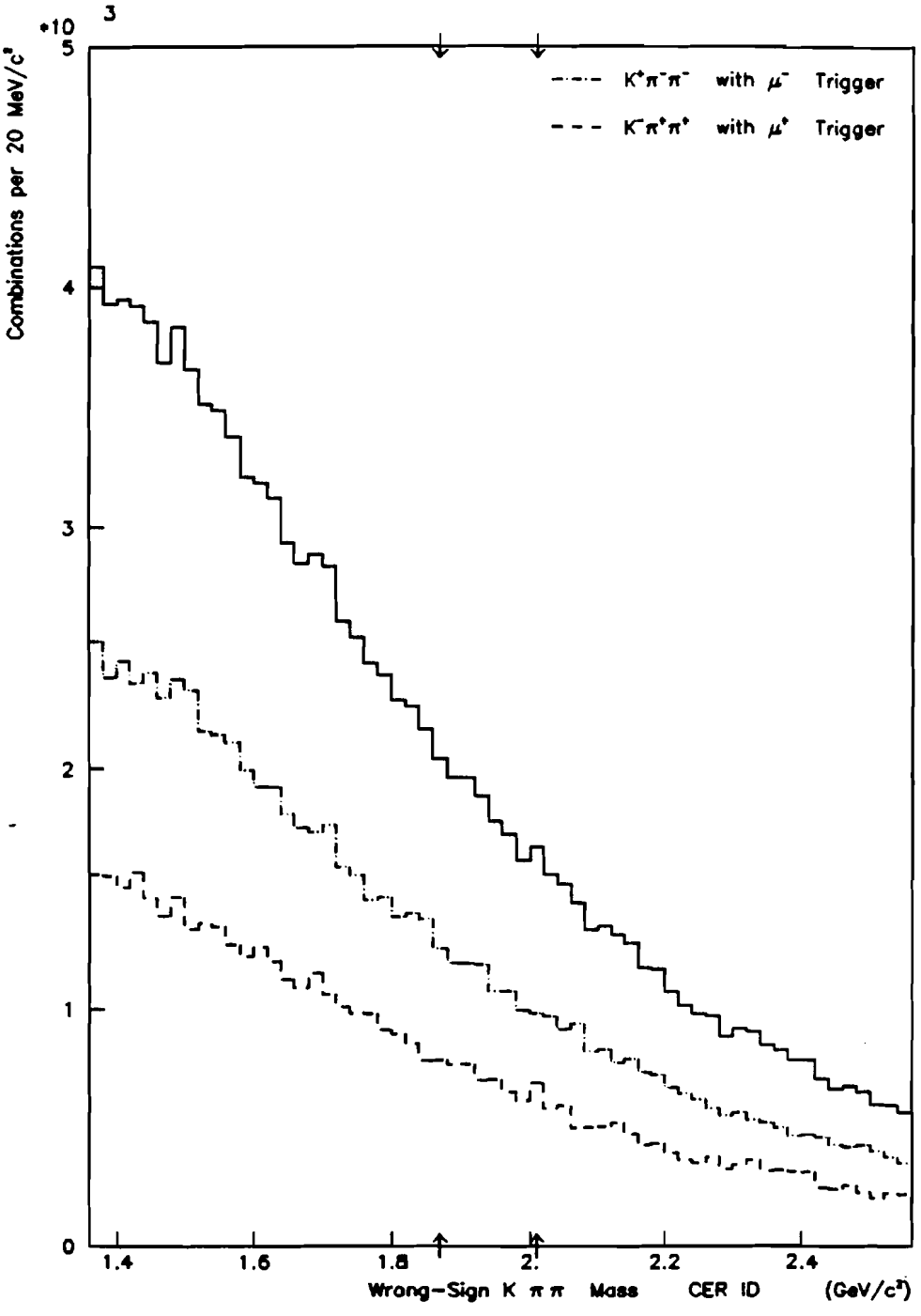

FIGURE 44. Wrong-sign $K^+\pi^-\pi^-$ and $K^-\pi^+\pi^+$ invariant mass plots. Particles are identified by the CER scheme with the PROBK2 level at 0.7. The sum of the two wrong-sign mass plots is also shown.

the neutral D is 0.14541 ± 0.00016 GeV/c^2 [70], which is only slightly larger than the charged pion mass. As a result, the width of the charged D^* is relatively narrow and reported to be less than 2 MeV/c^2. Since the D^* decay mode into a $D\pi$ pair yields only a few MeV of kinetic energy, the π, referred to as the soft pion, tends to have a low momentum in the laboratory frame. The soft pion momentum as measured in the laboratory, p_π, is given approximately by the expression

$$p_\pi \approx (m_\pi / m_D) p_D \approx 0.075 \, p_D$$

where p_D is the laboratory momentum of the D meson. Since the spectrometer did not accept many particles with momenta below 2 GeV/c, the acceptance of the spectrometer for centrally produced D^* mesons as detected via the neutral D and charge pion decay mode was relatively small. Nevertheless, since the neutral D can decay into a $K\pi$ pair, where the kaon should have an electric charge opposite of the soft pion emitted by the D^* decay, one can search for evidence of the charged D^* in the right-sign $K\pi\pi$ mass plots presented in figure 43. No evidence of charged D^* production is observed in these right-sign $K\pi\pi$ mass plots.

The $K\pi\pi$ mass plots shown in the previous subsection do not employ the constraint that one of the $K\pi$ pairs in the $K\pi\pi$ combination must have a mass consistent with the D meson in order for the $K\pi\pi$ final state to be due to the decay of a D^* meson. One can apply this constraint directly, and plot only those $K\pi\pi$ combinations for which at least one of the $K\pi$ pairs has a mass consistent with a D meson.

However, due to the small kinetic energy released by the D^* decay, the resolution of the spectrometer in the mass difference between the D^* and the D is expected to be much better than the mass resolution for the D^* meson. Thus a plot of the mass difference between the $K\pi\pi$ combinations and the $K\pi$ pairs that are subsets of the $K\pi\pi$ combinations should provide an enhanced signal to background by improving the resolution of the signal. This mass difference plot technique is a standard means of searching for the charged D^* [48].

The left hand column of figure 45 shows the right-sign mass difference plots for a scan of several bands in the $K\pi$ mass. Due to the small acceptance for the D^* state, the particles are identified via the BLIND scheme and the track quality cut is not invoked. The band that has the $K\pi$ mass restricted to between 1.815 and 1.915 GeV/c^2 has an enhancement around 0.1465 GeV/c^2. The right hand column of figure 45 shows the right-sign $K\pi$ mass plots for a scan over several $K\pi\pi$ $K\pi$ mass difference ranges. When the mass difference is restricted to the 1 MeV/c^2 bin that exhibits the enhancement around 0.1465 MeV/c^2, the corresponding right-sign $K\pi$ mass plot also exhibits an enhancement in the vicinity of the D meson mass. A similar set of mass difference plots and $K\pi$ mass plot scans for the wrong-sign correlations are shown in figure 46. The wrong-sign scan also employs the BLIND identification scheme and does not use the track quality cut.

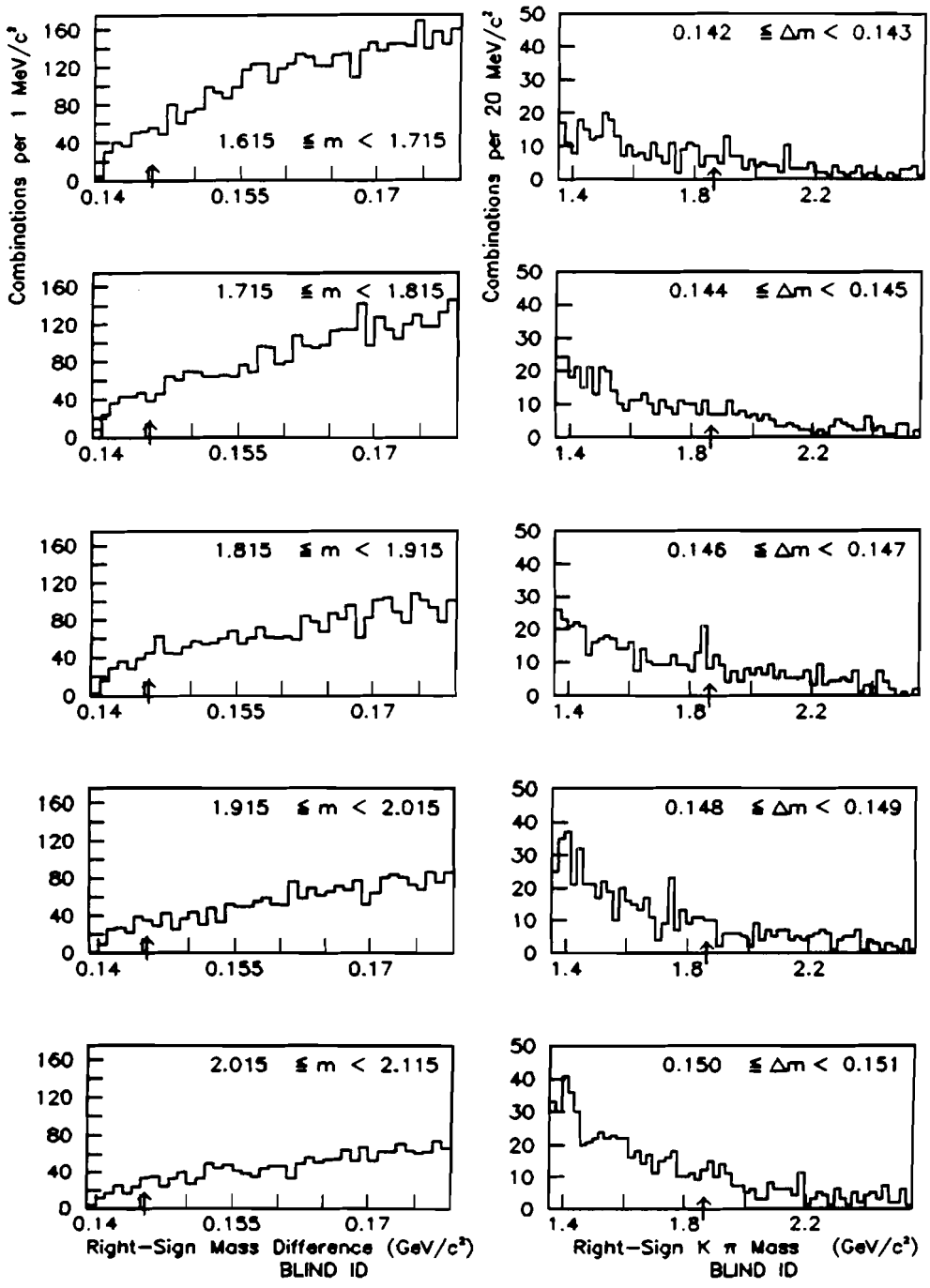

FIGURE 45. Slices of a scatterplot of right-sign $K\pi\pi$ minus $K\pi$ mass difference versus $K\pi$ mass. The left hand column presents the mass difference plots for several ranges of the $K\pi$ mass. The right hand column presents the $K\pi$ mass for several ranges of the mass difference. Particles are identified via the BLIND scheme, and the track quality cut is not invoked.

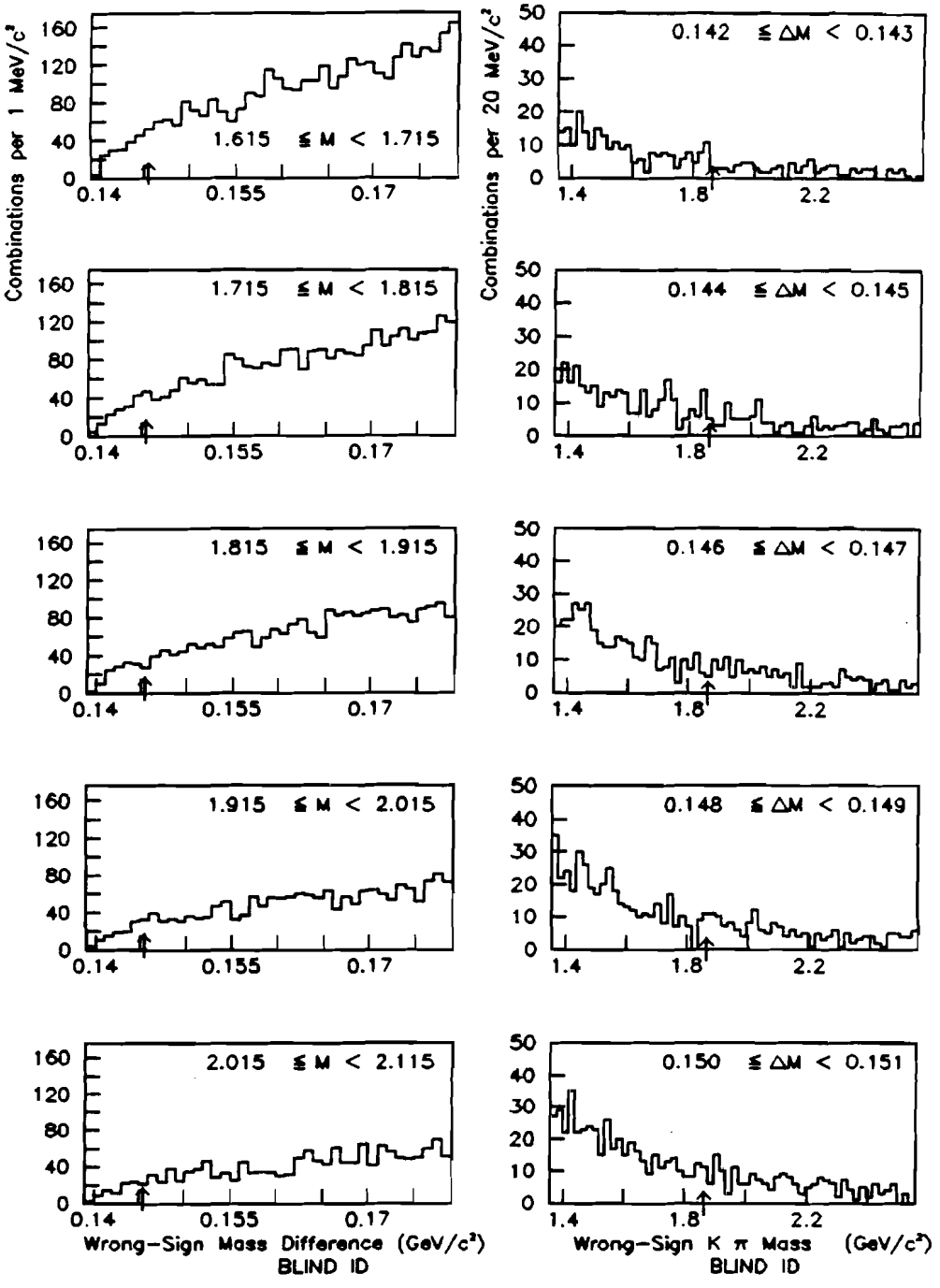

FIGURE 46. Slices of a scatterplot of wrong-sign Kππ minus Kπ mass difference versus Kπ mass. The left hand column presents the mass difference plots for several ranges of the Kπ mass. The right hand column presents the Kπ mass for several ranges of the mass difference. Particles are identified via the BLIND scheme, and the track quality cut is not invoked.

Figure 47(a) shows the right-sign mass difference plots in more detail for those $K\pi$ combinations within ± 50 MeV/c^2 of the D mass. Figures 47(b) and 47(c) show the two individual right-sign mass difference plots separately. The superimposed polynomials were determined by fits that excluded the contributions between 0.1445 and 0.1485 GeV/c^2. The corresponding right-sign $K\pi$ mass plots, with the constraint that the mass difference is between 0.145 and 0.148 GeV/c^2, are shown in figure 48. The superimposed polynomial fits exclude the masses between 1.795 and 1.935 GeV/c^2.

Although these enhancements in the right-sign $K\pi$ mass plot and mass difference plot are small, they appear in both plots with minimal software cuts. The mass difference plot excess contains 26 ± 16 combinations above the polynomial background. The corresponding $K\pi$ mass plot contains 33 ± 14 combinations above the polynomial background. The 153 combinations within the band containing the enhancement come from 150 different events from runs spread throughout the 1981 data sample. Furthermore, the locations of the enhancements are consistent with the locations anticipated for charged D^* decays. When the $K\pi$ mass plot is fit to a Gaussian plus polynomial background, the mean of the Gaussian is at 1.847 ± 0.010 GeV/c^2 and the standard deviation is 0.022 ± 0.010 GeV/c^2. (The neutral D meson mass is 1.8647 ± 0.0006 GeV/c^2 [70].) The mean of the mass difference enhancement is about 1 MeV/c^2 above the measured D^* value. The widths of both enhancements are comparable to those anticipated by the Monte Carlo studies (see figure 26). In addition, no similar enhancement is

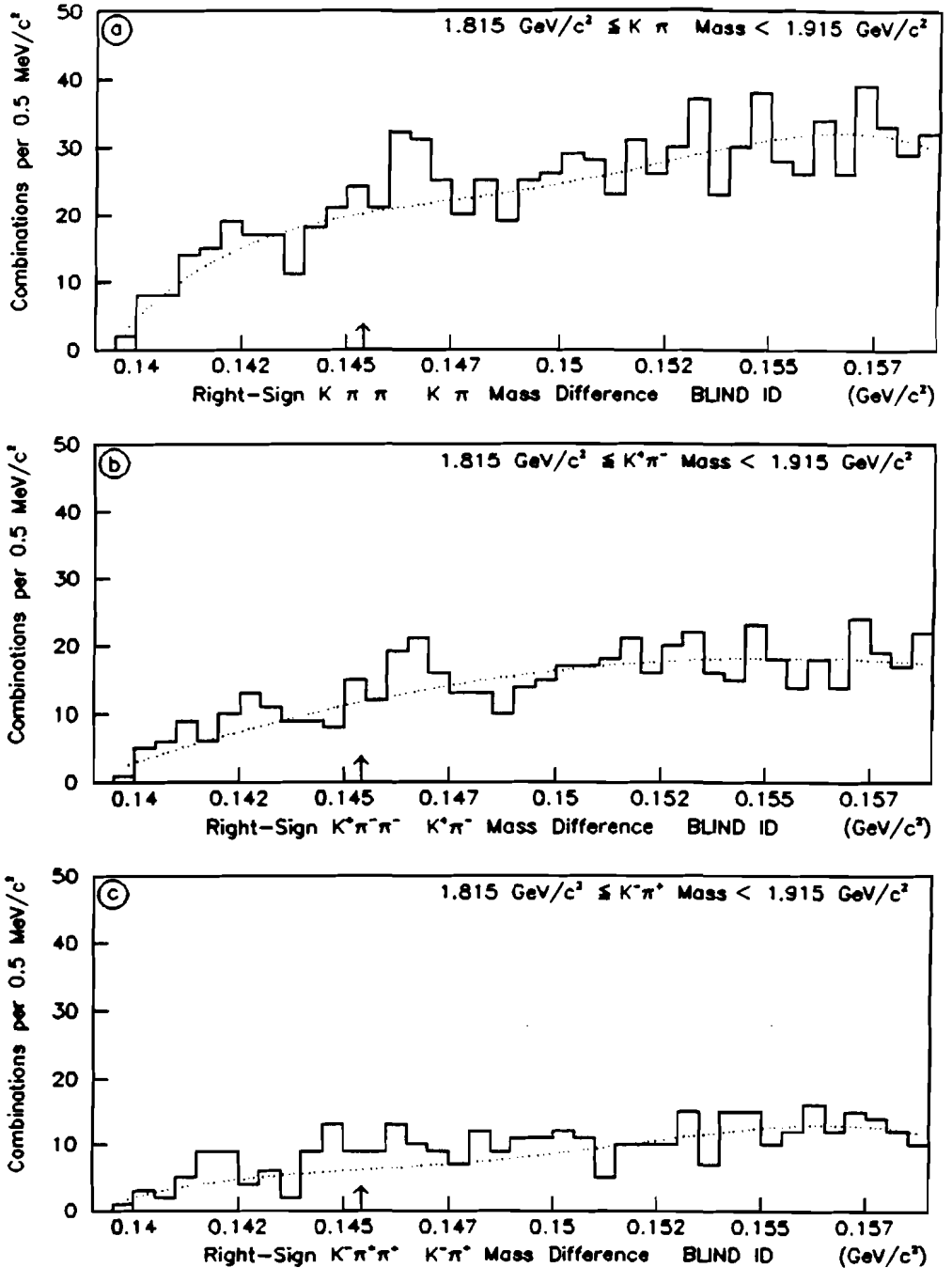

FIGURE 47. Right-sign Kππ Kπ mass difference plots with the Kπ mass restricted to the range 1.815 to 1.915 GeV/c^2. Particles are identified via the BLIND scheme and no track quality cut is invoked. (a) Sum of both right-signs. (b) Positive triggering muon. (c) Negative triggering muon.

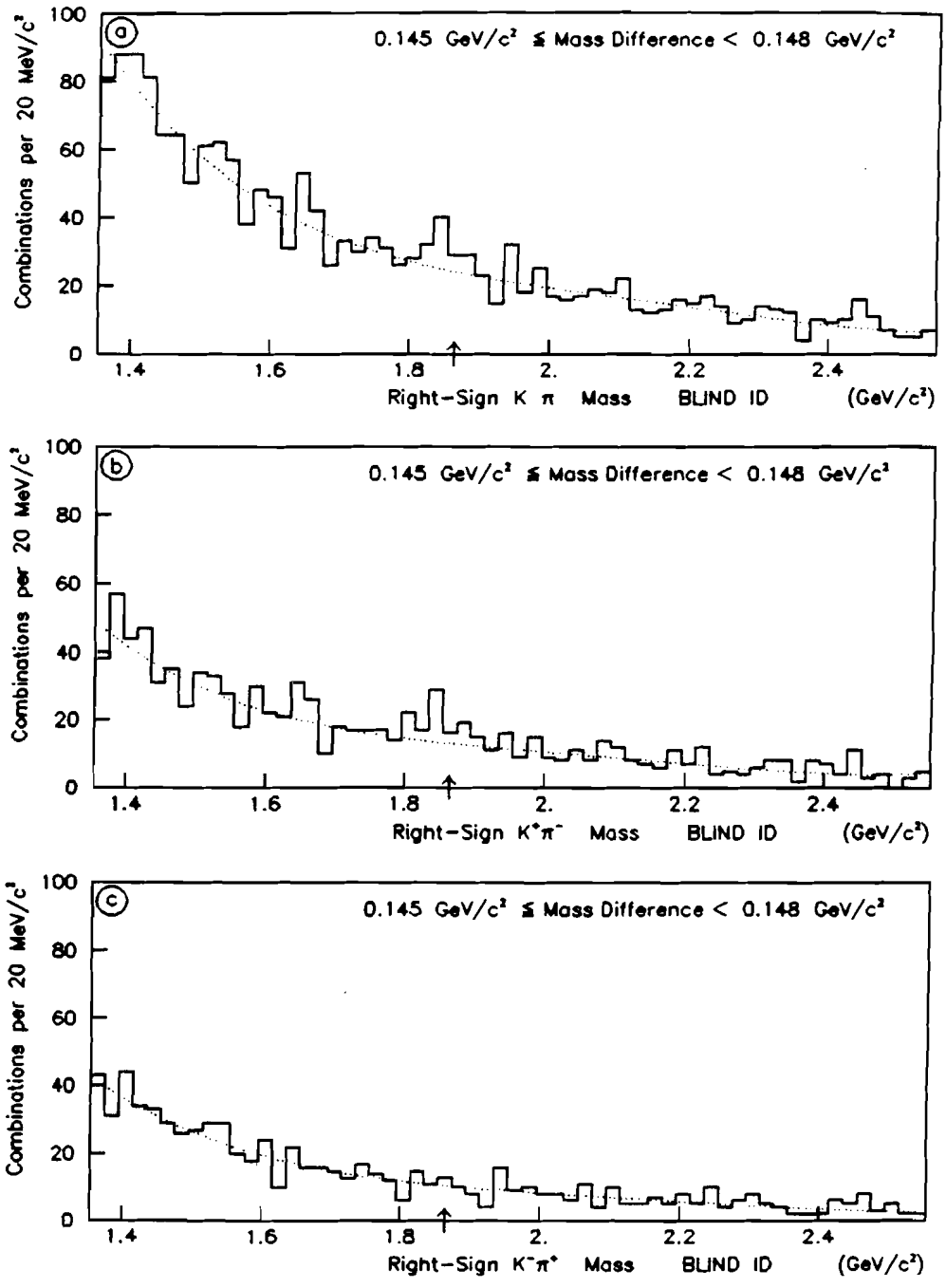

FIGURE 48. Right-sign Kπ mass plots with the Kππ $K\pi_2$ mass difference restricted to the range 0.145 through 0.148 GeV/c^2. Particles are identified via the BLIND scheme and no track quality cut is invoked. (a) Sum of both right-signs. (b) Positive triggering muon. (c) Negative triggering muon.

observed in the corresponding wrong-sign plots. Thus the interpretation of this small excess as evidence of charged D^* production appears to be consistent with the available information.

CHAPTER 6

RESULTS AND CONCLUSIONS

The data presented in the charm search mass plots of the previous chapter are summarized and interpreted as limits upon the total $D\overline{D}$ production cross section in π^- nucleon interactions at 205 GeV/c.

6.1 PRODUCTION CROSS SECTION

The cross section (σ) for an interaction is defined by the relation

$$\sigma = N_g / (N_b \eta)$$

where N_g is the number of such interactions that are generated by N_b beam particles incident upon a thin target that has η scattering centers per unit area. For this analysis, N_b is estimated to be

2.95×10^{11} based upon the livetime BEAM scaler and including minor corrections for a discriminator threshold problem, double bucket occupancy, and the beam attenuation due to the target thickness. The number of scattering centers (beryllium nuclei) per unit area in this experiment is determined from the properties and dimensions of the target. (Based upon a comparison of target-out and standard runs, a 12 percent increase in the calculated number of scattering centers was introduced to account for the materials in addition to the beryllium that served as target in this experiment.) So if the number of interactions generated can be determined, the cross section associated with that interaction can be estimated. If an upper limit on the number of such interactions generated can be measured, a corresponding upper limit upon the cross section for that process can be reported. In order to relate the number of interactions detected to the number of interactions generated, one must estimate the overall efficiency or acceptance of the detector for observing that interaction.

The prompt muon triggered data recorded and analyzed in this experiment represented interactions between incident negative pions and beryllium nuclei which yielded muons in the trigger arm and also particles in the forward arm. Coupled with assumptions concerning the types of charmed states produced, and the spectrum of the kinematic variables of those states, this data may be employed to estimate the cross section for production of $D\overline{D}$ pairs in interactions between pions and nucleons. If the average branching ratio for the D meson to decay to a state that includes a muon is given by B_T, and the branching

ratio for the associated $\overline{D}$ meson to decay via the mode considered in a mass plot is given by B_F, then the number of such events detected in that mass plot, N_d, is related to the number generated, N_g, by the expression

$$N_d = N_g \, B_T \, B_F \, \epsilon$$

where ϵ is the acceptance of the spectrometer for the muon from the D decay and the daughters of the partner $\overline{D}$ decay.

Since the cross section per nucleon is a more fundamental quantity than the cross section per nucleus, it is common practice to report measurements made with a nuclear target in terms of a measurement made upon a nucleon target. The relationship between a cross section as measured on a nuclear target (σ_A) whose mass number is A, and the cross section as measured with a nucleon target (σ), is frequently parametrized by the following expression:

$$\sigma_A = \sigma \, A^{\alpha}$$

Thus the expression for the $D\overline{D}$ cross section per nucleon can be written as follows:

$$\sigma = N_g \, / \, (\, N_b \, \eta \, A^{\alpha} \,) = N_d \, / \, (\, N_b \, \eta \, A^{\alpha} \, B_T \, B_F \, \epsilon \,).$$

A study of the A dependence of the absorption cross section for negative pions at 200 GeV/c yielded $\alpha=0.759\pm0.010$ [71]. The A dependence of inclusive ϕ production by a 120 GeV/c π^+ beam is parametrized by $\alpha=0.90\pm0.02$ [98]. The A dependence of J/ψ production by a 200 GeV/c π^- beam is given by $\alpha=0.97\pm0.02$ [99]. Since little experimental guidance is currently available on the A dependence of the hadronic production of charm, linear A dependence is assumed.

In order to estimate the detector acceptance and the average branching ratios appropriate for this data, assumptions must be made concerning the types of charmed particles that result from the hadronization of the produced charm anticharm quark pairs.

The prompt muon triggers recorded by our detector that arose from the decay of charmed particles are all assumed to come from the decay of D mesons. This assumption neglects contributions from the other charmed states that are stable against strong and electromagnetic decays.

Since the D and D^* mesons have comparable masses, and assuming that the probabilities for a naked charm quark to dress itself with a u or a d quark are equal, then counting the spin degrees of freedom, one might anticipate that the relative production ratios of direct D and D^* mesons to be as follows:

$$D^0 : D^+ : D^{*0} : D^{*+} = 1 : 1 : 3 : 3.$$

The same spin-weighted production ratios are assumed to apply to the antiparticles. Using the measured branching ratios for the D^* decays into D mesons, one finds that the expected number of D^0 to the number of D^+ is 2.16. This value is consistent with the ratio of 1.8 ± 0.7 reported by the prompt electron triggered experiment NA11 [52]. Taking the inclusive muonic D branching ratios as equal to the measured inclusive electronic D branching ratios, and assuming the relative direct D and D^* production rates listed above, the average branching ratio for D mesons into muons is

$$B_T = BR(D^0 \to \mu^+ X)\left[N(D^0)/N(D^0+D^+)\right] + BR(D^+ \to \mu^+ X)\left[N(D^+)/N(D^0+D^+)\right] = 0.105.$$

Using the spin-weighted production ratio assumption and the measured branching ratios for D^* cascades, the expected ratio of $D^{*+} \rightarrow D^0 \pi^+$ to total D^0 (including the D^0 mesons resulting from D^* decays) is 0.27. Experiment NA11 reported that this ratio is 0.17±0.08 [52], while LEBC provided a lower limit of 0.27±0.11 for that ratio [56].

To estimate the acceptance of the spectrometer for a $D\overline{D}$ pair, models for selecting the kinematic properties of the produced states are assumed. The Monte Carlo described in the fourth chapter is employed to estimate the acceptance for various models. In most of the results presented, the D and the $\overline{D}$ are assumed to be produced independently and with the same p_T and x_F distributions. Symmetry about x_F of zero is assumed in all models employed. This assumption neglects the possibility of leading particle effects. The trigger arm acceptance is calculated by assuming that half of the D mesons whose decay products include a muon decay via the mode $D \rightarrow K\mu\nu$, while the other half decay via the mode $D \rightarrow K^*(890)\mu\nu$ [29]. The trigger hodoscope efficiency is assumed to be unity. The acceptances calculated by the Monte Carlo must be corrected by a factor, labeled f, which accounts for the fraction of events that are rejected by cuts not represented in the Monte Carlo simulation. The correction factor f is a product of several different contributions:

1. The fraction of events that survive the clean vertex cut is 0.6891.

2. The fraction of events that survive the clean vertex cut in which the vertex selection algorithm selected the correct vertex is estimated to be 0.96.

3. The fraction of the events that survive the requirement that there be less than twenty valid M1 points in the event is 0.9932.

4. The fraction of events that survive the requirement that the trigger arm muons all have the same sign is 0.9878.

5. The factor to account for those events not completely processed due to CAMAC, hardware, or software errors detected during some stage of the processing of the events is 0.98.

The net product of the above correction factors yields f=0.64. A compilation of the various constants employed in the cross section estimates is provided in table 9.

6.1.1 Upper Limits from the Kπ Mass Plots

Coupled with the above assumptions concerning the production characteristics of charm, the data presented in the right-sign mass plots were employed to calculate results on the cross section for $D\bar{D}$ production by 205 GeV/c pions. The number of combinations above background in the Kπ mass plots in the vicinity of the D meson mass was determined by fitting a polynomial to the mass plot, excluding the contributions between 1.795 and 1.935 GeV/c^2. The resulting polynomial was employed to calculate the number of background combinations in the D mass region, and the covariance matrix that resulted from the polynomial fit was used to determine the uncertainty in the number of background combinations. The number of excess combinations between 1.815 and 1.915 GeV/c^2 was then calculated, and

TABLE 9. Constants employed in the cross section calculations.

N_b	number of incident live beam	2.95×10^{11}
ρ	density of beryllium	1.848 g/cm^3
ℓ	length of the target	3.0 cm
N_A	Avogadro Number	6.022×10^{23} mole^{-1}
M	molecular weight of beryllium	9.012 g/mole
$\eta = 1.12\ \rho\ \ell\ N_A\ /\ M$	scatterers per area	4.14×10^{23} cm^{-2}
A	mass number of beryllium	9
α	exponent for A dependence	1.0
$N_b\ \eta\ A^{\alpha}$	integrated luminosity	1.10 pb^{-1}
f	event cut correction	0.64
$BR(D^0\rightarrow\mu^+X)$	0.075±0.011±0.004	[27]
$BR(D^+\rightarrow\mu^+X)$	0.170±0.019±0.007	[27]
$BR(D^0\rightarrow K^-\pi^+)$	0.049±0.009±0.005	[96]
$BR(D^0\rightarrow K^-\pi^+\pi^-\pi^+)$	0.075±0.012±0.014	[96]
$BR(D^+\rightarrow K^-\pi^+\pi^+)$	0.091±0.015±0.009	[96]
$BR(D^{*0}\rightarrow D^0\pi^0)$	0.538±0.094	[97]
$BR(D^{*0}\rightarrow D^0\gamma)$	0.462±0.094	[97]
$BR(D^{*+}\rightarrow D^0\pi^+)$	0.489±0.083	[97]
$BR(D^{*+}\rightarrow D^+\pi^0)$	0.340±0.070	[97]
$BR(D^{*+}\rightarrow D^+\gamma)$	0.17±0.11	[97]
$N(D^0)/N(D^+)$	number of D^0 per D^+	2.16
B_T	average D to muon branching ratio	0.105

the uncertainty in the number of excess combinations resulted from the statistical uncertainty in the total number of combinations between 1.815 and 1.915 GeV/c^2 in quadrature with the uncertainty in the number of background combinations.

Since none of the direct $K\pi$ mass plots contain a statistically significant enhancement in the vicinity of the D meson mass, the results are interpreted as upper limits upon the level of $D\bar{D}$ production. Both right-sign mass plots individually measure the $D\bar{D}$ cross section, but, since the acceptances are similar for right-sign $K^+\pi^-$ and $K^-\pi^+$ combinations, and the backgrounds in the $K^+\pi^-$ and $K^-\pi^+$ mass plots are also similar, the lowest upper limits are achieved by combining both right-sign mass plots, and thus increasing the acceptance by about a factor of two. Assuming the fluctuations in the number of excess combinations in the vicinity of the D mass in the right-sign mass plots have a Gaussian distribution, then since

$$\frac{1}{\sqrt{(2\pi)}} \int_{-\infty}^{1.645} \exp(-\tfrac{1}{2}z^2) \, dz \approx 0.95$$

the 95 percent confidence upper limit on the number of detected $D\rightarrow K\pi$ decays is given by the sum of the number of excess combinations observed plus 1.645 times the uncertainty in the number of excess combinations observed. This upper limit on the number of D decays is employed to calculate the 95 percent confidence upper limit on the $D\bar{D}$ production cross section using various production models to estimate the acceptance. The statistical uncertainty introduced by the Monte Carlo calculation of the acceptance is small and neglected in this

upper limit calculation. Due to the finite resolution of the spectrometer, the entire signal is not necessarily limited to the window from 1.815 to 1.915 GeV/c^2, and a correction must be introduced to account for this mass window cut. The spectrometer acceptances employed in the calculation of the upper limits also include corrections for the efficiency of the particle identification scheme, the track quality cut, and the trigger muon quality cuts. The systematic uncertainties are not included in these upper limit calculations.

The results of the polynomial fit to the combined right-sign $K\pi$ mass plot using the CONCER identification scheme (figure 37) are presented in table 10. The trigger arm acceptance (A_T), the forward arm acceptance (A_F), and the fraction of the signal anticipated within the mass window selected (ξ), are also presented in the table. The acceptance ε is given by the expression

$$\varepsilon = 2\ f\ A_T\ A_F\ \xi.$$

The sensitivity, and the 95 percent confidence upper limits on the $D\bar{D}$ production cross section resulting from that mass plot are also presented in table 10. The sensitivity is the expected number of detected charmed particles per microbarn of $D\bar{D}$ production cross section.

Similar results for the right-sign $K\pi$ mass plot with CONCER identification and the $\cos(\Theta_{CM})$ cut (figure 38) are presented in table 11. Although the imposition of the cut on the kaon center of momentum angle has not revealed a signal, it does provide lower upper

TABLE 10. The 95 percent confidence upper limits on the $D\bar{D}$ production cross section determined from the right-sign $K\pi$ mass plot with CONCER identification (figure 37). The column labeled A_T contains the trigger arm acceptances. The column labeled A_F lists the corresponding forward arm acceptances. The column labeled ξ shows the fraction of the signal expected within the selected mass window.

$B_F = BR(D^0 \to K^- \pi^+)\ N(D^0) / [N(D^0) + N(D^+)] = 0.0335$

Number of combinations with $1.815 \leq K\pi$ mass $< 1.915 = 23074$

Number of parameters in background polynomial fit = 5

χ^2 per degree of freedom = 46.2 / 48 = 0.963

Number of combinations above background = 168±177

The 95 percent confidence upper limit for N_d is 459

Model	n	b	A_T	A_F	ξ	Sensitivity $(\mu b)^{-1}$	σ Upper Limit (μb)
I	1	1.1	0.0104	0.181	0.76	7.0	65
I	3	1.1	0.0167	0.132	0.86	9.4	49
I	6	1.1	0.0232	0.103	0.92	10.9	42
II	1	1.1	0.0146	0.148	0.85	9.0	51
II	3	1.1	0.0195	0.120	0.92	10.6	43
II	6	1.1	0.0242	0.094	0.95	10.7	43
III	5	2.0	0.0287	0.094	0.96	12.8	36

TABLE 11. The 95 percent confidence upper limits on the $D\bar{D}$ production cross section determined from the right-sign $K\pi$ mass plot with CONCER identification and $-0.7 \leq \cos(\Theta_{CM}) < 0.7$ (figure 38). The column labeled A_T contains the trigger arm acceptances. The column labeled A_F lists the corresponding forward arm acceptances. The column labeled ξ shows the fraction of the signal expected within the selected mass window.

$B_F = BR(D^0 \to K^- \pi^+)\ N(D^0)/[N(D^0)+N(D^+)] = 0.0335$

Number of combinations with $1.815 \leq K\pi$ mass $< 1.915 = 8141$

Number of parameters in background polynomial fit = 5

χ^2 per degree of freedom = 35.3 / 48 = 0.736

Number of combinations above background = 104±105

The 95 percent confidence upper limit for N_d is 277

Model	n	b	A_T	A_F	ξ	Sensitivity $(\mu b)^{-1}$	σ Upper Limit (μb)
I	1	1.1	0.0104	0.143	0.79	5.7	48
I	3	1.1	0.0167	0.111	0.87	8.0	35
I	6	1.1	0.0232	0.088	0.92	9.3	30
II	1	1.1	0.0146	0.117	0.86	7.3	38
II	3	1.1	0.0195	0.103	0.94	9.4	30
II	6	1.1	0.0242	0.078	0.95	8.8	31
III	5	2.0	0.0287	0.085	0.96	11.6	24

limits on the $D\overline{D}$ cross section.

Table 12 contains the upper limits determined from the right-sign $K\pi$ mass plot with CER identification (figure 39). These are the lowest upper limits presented, however, the sensitivities associated with this mass plot are significantly smaller due to the Cherenkov requirements imposed. Consequently, the acceptance corrections are larger, and more dependent upon the Cherenkov counter efficiency measurements. Furthermore, the N_d associated with figure 39 has a negative value, which corresponds to an unphysical result for the number of generated charmed particles. As a result, the reported upper limits listed in table 12 are probably artificially low. Thus, the upper limits derived from figure 38 are believed to be more reliable results.

The upper limits for the $D\overline{D}$ production cross section determined from the $K\pi$ mass plot in figure 38 vary between 24 and 48 μb per nucleon depending upon the production model employed. The general level of hadronic production of charm reported in the literature at similar center of momentum energies is on the order of tens of microbarns, implying that this analysis is just short of being sensitive to the direct $K\pi$ decay mode of the D meson.

TABLE 12. The 95 percent confidence upper limits on the $D\bar{D}$ production cross section determined from the right-sign $K\pi$ mass plot with CER identification (figure 39). The column labeled A_T contains the trigger arm acceptances. The column labeled A_F lists the corresponding forward arm acceptances. The column labeled ξ shows the fraction of the signal expected within the selected mass window.

$B_F = BR(D^0 \to K^- \pi^+)\ N(D^0)/[N(D^0)+N(D^+)] = 0.0335$

Number of combinations with $1.815 \leq K\pi$ mass $< 1.915 = 1887$

Number of parameters in background polynomial fit = 5

χ^2 per degree of freedom = 44.9 / 48 = 0.936

Number of combinations above background = -24±51

The 95 percent confidence upper limit for N_d is 60

Model	n	b	A_T	A_F	ξ	Sensitivity $(\mu b)^{-1}$	σ Upper Limit (μb)
I	1	1.1	0.0104	0.030	0.83	1.3	47
I	3	1.1	0.0167	0.035	0.93	2.7	22
I	6	1.1	0.0232	0.033	0.95	3.6	17
II	1	1.1	0.0146	0.033	0.89	2.1	29
II	3	1.1	0.0195	0.034	0.91	3.0	20
II	6	1.1	0.0242	0.033	0.96	3.9	16
III	5	2.0	0.0287	0.039	0.99	5.5	11

6.1.2 Upper Limits from the $K\pi\pi\pi$ and $K\pi\pi$ Mass Plots

The right-sign $K\pi\pi\pi$ mass plot was fit to determine the number of excess combinations in the vicinity of the D mass, and the results are presented in table 13. Similar calculations were performed for the right-sign $K\pi\pi$ mass plot, and the results are presented in table 14. The larger combinatorial backgrounds in these mass plots result in less restrictive upper limits on the $D\overline{D}$ production cross section than those determined from the $K\pi$ mass plots.

6.1.3 Cross Sections from the Charged D^* Search

Evidence for the charged D^* decay into a neutral D meson and a soft pion was searched for in the $K\pi\pi$ mass minus $K\pi$ mass plot when the $K\pi$ mass was restricted to between 1.815 and 1.915 GeV/c^2, and also in the $K\pi$ mass plot when the mass difference was restricted to the vicinity of the measured D^* minus D mass. The right-sign plots show an enhancement near the vicinity of interest. The background in the mass difference plot shown in figure 47(a) was fit to a polynomial excluding the contributions between 0.1445 and 0.1485 GeV/c^2. There is an excess of 26±16 combinations above background with a mass difference between 0.145 and 0.148 GeV/c^2. The excess is centered about 1 MeV/c^2 above the mean of the D^* D mass difference reported in other experiments. Fitting the corresponding right-sign $K\pi$ mass plot

TABLE 13. The 95 percent confidence upper limit on the $D\overline{D}$ production cross section determined from the $K\pi\pi\pi$ mass plot with CER identification (figure 41). The column labeled A_T contains the trigger arm acceptances. The column labeled A_F lists the corresponding forward arm acceptances. The column labeled ξ shows the fraction of the signal expected within the selected mass window.

$B_F = BR(D^0 \to K^-\pi^+\pi^-\pi^+)\ N(D^0)/[N(D^0)+N(D^+)] = 0.051$

Number of combinations with $1.815 \leq K\pi\pi\pi$ mass $< 1.915 = 42892$

Number of parameters in background polynomial fit = 5

χ^2 per degree of freedom = 51.9 / 48 = 1.080

Number of combinations above background = -54 ± 243

The 95 percent confidence upper limit for N_d is 346

Model	n	b	A_T	A_F	ξ	Sensitivity $(\mu b)^{-1}$	σ Upper Limit (μb)
II	3	1.1	0.0195	0.013	0.92	1.8	190

TABLE 14. The 95 percent confidence upper limit on the $D\bar{D}$ production cross section determined from the $K\pi\pi$ mass plot with CER identification (figure 43). The column labeled A_T contains the trigger arm acceptances. The column labeled A_F lists the corresponding forward arm acceptances. The column labeled ξ shows the fraction of the signal expected within the selected mass window.

$B_F = BR(D^+ \to K^- \pi^+ \pi^+)\ N(D^+)/[N(D^0)+N(D^+)] = 0.0288$

Number of combinations with $1.820 \leq K\pi\pi$ mass $< 1.920 = 11509$

Number of parameters in background polynomial fit = 5

χ^2 per degree of freedom = 46.0 / 48 = 0.959

Number of combinations above background = -28±125

The 95 percent confidence upper limit for N_d is 177

Model	n	b	A_T	A_F	ξ	Sensitivity $(\mu b)^{-1}$	σ Upper Limit (μb)
II	3	1.1	0.0195	0.020	0.95	1.6	110

(figure 48(a)) yields an excess of 33±14 combinations between 1.815 and 1.915 GeV/c^2. (Mass combinations between 1.795 and 1.935 GeV/c^2 were excluded from this fit.)

Interpreting the excess observed in the mass difference and the $K\pi$ mass plots as 30±16 charged D^* decays, and using the assumptions outlined in the beginning of this chapter, the corresponding $D\bar{D}$ production cross section can be calculated. The results of the cross section calculation are presented in table 15 for several different assumptions about the kinematic distributions of the produced D^* mesons. The trigger arm acceptance is calculated based upon a generated D meson distribution, while the forward arm acceptance is based upon D^* production distributed according to the same model. The difference in the trigger arm acceptance depending upon whether a D or a D^* is produced according to a given distribution is believed to be negligible since the trigger arm muon acceptances from D and D^* parents that were produced according to model I with n=3 and b=1.1 $(GeV/c)^{-2}$ were equal within the uncertainty due to the statistics of the test. (In calculating the forward arm acceptance, the window applied to the mass difference plot in the Monte Carlo is from 0.144 to 0.147 GeV/c^2.)

Although the $D\bar{D}$ cross sections determined from the charged D^* search are larger than the upper limits determined from the $K\pi$ mass plots for some of the production models presented, the two measurements are consistent when the uncertainties are taken into account, so a comparison of the upper limits and the cross sections

TABLE 15. $*D\bar{D}$ production cross section estimates based upon the charged D^* search presented in figures 47 and 48. The column labeled A_T contains the trigger arm acceptances. The column labeled A_F lists the corresponding forward arm acceptances. The column labeled ξ shows the fraction of the signal expected within the selected mass window.

$B_F = BR(D^{*+} \to D^0 \pi^+)\ BR(D^0 \to K^- \pi^+)\ N(D^{*+}) / [N(D^0) + N(D^+)] = 0.0090$

Fit mass difference plot shown in figure 47(a)

Number of combinations with $0.145 \leq$ mass difference $< 0.148 = 153$

Number of parameters in background polynomial fit = 5

χ^2 per degree of freedom = 20.4 / 26 = 0.786

Number of combinations above background = 26±16

Fit right-sign Kπ mass plot shown in figure 48(a)

Number of combinations with $1.815 \leq K\pi$ mass $< 1.915 = 153$

Number of parameters in background polynomial fit = 5

χ^2 per degree of freedom = 49.8 / 48 = 1.037

Number of combinations above background = 33±14

Model	n	b	A_T	A_F	ξ	Sensitivity (μb)$^{-1}$	σ (μb)
I	1	1.1	0.0104	0.114	0.59	0.92	32±17
I	3	1.1	0.0167	0.061	0.66	0.89	34±18
I	6	1.1	0.0232	0.026	0.75	0.61	49±26
II	3	1.1	0.0195	0.037	0.70	0.68	44±24

fails to discriminate against any of the production models presented.

Based upon a fit to the momentum distribution of the charged D^* mesons observed in the prompt electron triggered experiment NA11, ACCMOR reported an exponent for the x_F dependence of $n=3.2\pm1.5$ for production model I [51]. Using production model I with $n=3$ and $b=1.1$ $(GeV/c)^{-2}$, the charged D^* search presented in this document yields a $D\overline{D}$ production cross section of 34 ± 18 μb, which is compatible with the $D\overline{D}$ production cross sections reported by NA11.

6.2 SYSTEMATIC UNCERTAINTIES

There are many potential sources of systematic uncertainties in this analysis. The sources which are judged to be largest are summarized in table 16.

Uncertainties in the beam count and the effective target material contribute to the systematic uncertainties in the integrated luminosity. The uncertainty in the beam count as manifested in the trigger rate change (illustrated in figure 29(c)) results in a -4 percent to +27 percent estimated uncertainty in the calculated cross sections. The large positive uncertainty results from the unlikely case that the BEAM sum overestimated the incident beam during the majority of the runs, thus causing the apparent trigger rate shift. The multiple occupancy of the beam bunches was not measured, but it is estimated to contribute less than ±5 percent uncertainty to

TABLE 16. Summary of the sources of systematic uncertainties.

Source	Estimated Contribution to the Uncertainty in Cross Section (Percent)	
INTEGRATED LUMINOSITY		
Beam Count	-4	+27
Multiple Bunch Occupancy	-5	+5
Muon Contamination of Beam	---	+2
Effective Target Material	-5	+5
TRIGGER ARM ACCEPTANCE		
Magnetic Field Representation	-20	+8
Trigger Arm Muon Path	-11	---
Target Absorber Geometry	-6	+7
Chamber Efficiency	-5	+5
FORWARD ARM ACCEPTANCE		
Vertex Selection	---	+25
Chamber Efficiency	-5	+5
Mass Scale Calibration	---	+10
Mass Resolution	---	+5

the beam sum. The decay of pions in the beam results in a muon contamination of the beam. Any such muons which were transported by the beam line were counted in the BEAM sum. This muon contamination is estimated to contribute less than a +2 percent uncertainty to the cross section. The amount of effective target material is judged to be uncertain at the ±5 percent level.

The largest systematic uncertainty in the trigger arm acceptance is attributed to the uncertainty in the calculated magnetic field in the 40D48 yoke. Monte Carlo studies of reasonable variations in the calculated yoke field result in variations in the cross section between -20 percent and +8 percent.

In calculating the trigger arm acceptance, all successful Monte Carlo triggering muons were required to pass through each of the trigger arm hodoscopes. However, since particles accompanied the triggering muon in actual interactions, and no tracking coincidences were available in the upstream end of the trigger arm, some of the hodoscope signals necessary to satisfy the trigger requirements may have been generated by particles other than the triggering muon. These "accidental" coincidences would release the triggering muon from the requirement that it pass through each hodoscope in the trigger. If the triggering muon is only required to satisfy the M2 M3 road (MX), then the trigger arm muon acceptance increases by 28 percent. If the triggering muon is only required to satisfy M1*MX, then the acceptance increases by 15 percent. When the triggering muon is only required to satisfy M0*M1*MX, the acceptance increases by 13 percent.

(These calculations were performed using model II with n=3 and b=1.1 $(GeV/c)^{-2}$.) Using the hodoscope scalers to estimate the fraction of probable accidental coincidences, it is estimated that the uncertainty in the triggering muon path results in an uncertainty in the cross section of less than -11 percent.

By altering the geometry in the Monte Carlo simulation of the trigger arm acceptance, it is estimated that uncertainties in the actual target and absorber geometry could result in cross section shifts between -6 percent and +7 percent. Uncertainties in the average efficiency of the trigger arm PWC's result in an estimated uncertainty of ±5 percent in the cross section.

The largest systematic uncertainty in the forward arm acceptance is due to the vertex selection procedure. Recall that the YZ segment finding algorithm depends weakly upon the X vertex location. Only 73 percent of the events surviving the clean vertex cut have the tracking vertex and the DST vertex within ±0.002 m of each other. Thus 27 percent of the events could contain some improper YZ segments because the wrong X_{VTX} was employed in the track search. (This situation was simulated in the Monte Carlo, but no background hits were generated.) It is estimated that this condition is responsible for a +25 percent uncertainty in the cross section derived from the charged D^* search.

The uncertainties in the forward arm chamber efficiencies are estimated to contribute less than ±5 percent uncertainty to the cross section. The uncertainty in the Cherenkov counter efficiency is

negligible.

The uncertainty in the calibration of the forward arm mass scale results in an uncertainty in the appropriate mass plot search window location, and a corresponding uncertainty in the acceptance and cross section. Comparing the ϕ mass measured in this experiment against the world average value, the mass scale is believed to be accurate to within ± 20 MeV/c^2 at the D^0 mass, and thus the uncertainty in the mass scale is estimated to contribute an uncertainty of +10 percent to the cross section.

Uncertainty in the mass resolution of the forward arm also introduces uncertainties in the cross section. Since the observed ϕ and $K^*(890)$ signals have widths in general accord with expectations, it is estimated that uncertainties in the forward arm mass resolution contribute less than +5 percent to the cross section uncertainty.

When the uncertainties described above are combined in quadrature, they result in a systematic uncertainty in the cross section derived from the D^* search of between -26 percent and +41 percent. These systematic uncertainties would contribute less than a 6 percent increase to the cross section upper limits presented.

In addition to the systematic uncertainties discussed above, the assumptions employed in extracting a cross section also introduce additional uncertainties. Although the effect of these assumptions is not included in the quoted systematic uncertainties, the impact of several of the assumptions is briefly described. If the A dependence

is assumed to be $A^{0.76}$ rather than A^1, then the reported cross section would be increased by 69 percent. The effect of the assumption that all prompt muons from charmed sources recorded by the trigger arm of the detector were due to D meson decays is uncertain because the cross sections for Λ_c^+ and F hadronic production have not yet been determined at the beam energy employed in this experiment. (The trigger arm acceptance for muons from Λ_c^+ decays is smaller than that for muons from D decays. Furthermore, the reported Λ_c^+ inclusive electronic branching ratio is smaller than the D semileptonic branching ratios. Reports of the observation of hadronically produced F mesons are scarce.) If equal production rates for D^* and D mesons are assumed rather than the spin-weighted production ratios, then the reported upper limits on the cross sections from the direct D searches are increased by 3 percent, while the cross sections from the D^* search are increased by 42 percent. The measured semielectronic branching ratios are uncertain at the 10 percent level. Altering the assumed mix of $D\rightarrow K\mu\nu$ and $D\rightarrow K^*\mu\nu$ from an even split to 60 percent $D\rightarrow K\mu\nu$ and 40 percent $D\rightarrow K^*\mu\nu$ results in a 5 percent decrease in the reported cross sections. The branching ratios employed in the search for individual decay modes in the forward arm are uncertain at about the 20 percent level. The range of the cross section results from the different production models gives some indication of the sensitivity of the reported cross section to the production model assumptions.

6.3 CHARM CONTENT OF THE PROMPT MUON TRIGGERED EVENTS

The history of the event processing involved in this analysis is summarized in table 17. The upper limits and cross sections resulting from this analysis can be employed to estimate the fraction of the reconstructed prompt muon triggers that are attributable to charmed sources. The number of clean vertex DST events with triggering muons from charmed sources is given by

$$N_\mu = \sigma\ N_b\ \eta\ A^\alpha\ B_T\ 2\ f\ A_T\ /\ 0.96$$

where σ is the $D\bar{D}$ production cross section. From the $D\bar{D}$ cross section upper limits presented in table 11, N_μ is less than 117 000. Thus, the 95 percent confidence upper limit on the fraction of clean vertex DST events with triggering muons attributable to charmed sources is 40 percent. Using the $D\bar{D}$ cross section of 34±18 μb determined from the charge D^* search, the fraction of the clean vertex DST events with triggering muons that are due to charmed sources is 30±16 percent.

The $D\bar{D}$ production cross section as estimated from the D^* search is 300±180 μb per beryllium nucleus. The absorption cross section for π^- on beryllium at 200 GeV/c is estimated to be 139 mb per nucleus [71]. Thus about 0.21±0.13 percent of all interactions in E515 contained charmed particles. The prompt muon trigger enhanced the fraction of recorded events containing charm to about 7.8±4.7 percent. The trigger combined with the off-line analysis enhanced the fraction of selected events containing charmed particles by about two orders of magnitude.

TABLE 17. Summary of the event analysis described in this document.

	Number of Events Remaining	Percent Passing Requirement	Percent of Total
total events recorded	2 302 453		
prompt muon triggers	1 936 057	100	100
omit events recorded during spectrometer shakedown	1 807 000	93	93
omit unreadable data tapes, short runs, events with CAMAC errors	1 768 811	98	91
output by MUON PASS event must have downstream trigger arm segment of potential interest	931 000	52	48
output by HADRON PASS event must have downstream trigger arm track	748 529	80	39
eliminate runs of questionable quality	739 513	99	38
enforce clean vertex cut	508 969	69	26
require reconstructed triggering muon	290 708	57	15

The data gathered during the 1981 data run of E515 was also analyzed to search for evidence of charm production through a study of the semileptonic decay of both the charmed and anticharmed particles produced in the same event [100]. In the absence of $D^0\overline{D}^0$ mixing, the semileptonic decays of charmed anticharmed pairs yield opposite sign leptons. An excess of opposite sign μe pairs over like sign μe pairs was observed. The background subtracted momentum spectrum of the electrons from the opposite sign μe excess was consistent with the electron spectrum generated by the correlated production model, model III. Taking the average semileptonic D branching ratio to be 0.105, the resultant $D\overline{D}$ cross section as determined by the opposite sign μe excess is 10±3 μb per nucleon. The 95 percent confidence upper limit on the $D\overline{D}$ production cross section as determined by the right-sign Kπ mass plots using the same correlated model is 24 μb, which is consistent with the μe result. Using the acceptance calculated with the uncorrelated production model I with n=3 and b=1.1 $(GeV/c)^{-2}$, the μe excess corresponds to a $D\overline{D}$ cross section of 43±14 μb per nucleon, which is consistent with the upper limit of 35 μb determined from the Kπ mass plot and the cross section of $34\pm18^{+14}_{-9}$ μb determined from the charged D^* search. However, the detected electron momentum spectrum predicted by this model is significantly harder than the observed spectrum from the μe excess.

The excess opposite sign μe coincidences observed in this experiment imply that approximately 17 percent of the final event sample was from charmed sources. A study of the dimuons observed in the spectrometer implied that 12 percent of the final event sample was triggered by muons from electromagnetic sources [100]. Pion and kaon decays were probably responsible for the majority of the remaining triggers in the final event sample.

6.4 CONCLUSIONS

Table 18 presents a brief summary of the results of several recent fixed target experiments on the production of charmed particles by incident protons. Where possible, the results presented in the last column have been adjusted to reflect the assumptions employed in this document. Table 19 presents a similar summary of the production of charmed particles by negative pion beams. Most of the results employ production model I, and have consistent values for the p_T dependence. There is no clear consensus on the x_F dependence. The total $D\bar{D}$ production cross section is around 30 μb for pion beams with about 20 GeV center of momentum energies. Table 11 presents the $D\bar{D}$ production cross section upper limits determined from an analysis of a right-sign $K\pi$ mass plot from the E515 data with several different production models. The 95 percent confidence upper limits vary between 24 and 48 μb per nucleon, which is consistent with the results reported by other similar experiments. Table 15 presents the $D\bar{D}$ production cross sections determined from the charged D^* search, and those values are also consistent with other experiments. In spite of numerous experimental efforts, the results on the hadronic production of charm remain meager and not entirely clear. Future experiments on the hadronic production of heavy flavors are depending more heavily upon the detection of the heavy flavor decay vertices in order to suppress backgrounds.

TABLE 18. Summary of results from several recent fixed target experiments on the production of charmed particles by incident protons. When possible, the last column contains the $D\bar{D}$ production cross section values adjusted to reflect the assumptions employed in this thesis, including branching ratios and symmetry about x_F of zero. All results assume linear A dependence.

Experiment Ref.		p Beam Momentum (Gev/c)	Target Material	n	Production Model	b	Reported Charm σ (μb)	$D\bar{D}$ Cross Section (μb)
NA11 [50]	single e trigger	150	Be		Model I		15	
ACCMOR	Kπ and Kππ			0.8		1.1		7
E595 [46]	density extrapolation	350	Fe		Model I		$8.2\pm0.8\pm1.4$	
CCFRS [47]	for prompt single muons			6.0 ± 0.8		0.75 ± 0.2	$x_F>0$	$12.5\pm1.2\pm2$
NA16 [54]	interaction trigger	360	H		Model I		19^{+13}_{-5}	
LEBC EHS	vertex detection			1.8 ± 0.8		1.1 ± 0.3		
E613 [43]	density extrapolation	400	W	$(1-\lvert x_F\rvert)^n \exp(-bm_T)$			$27\pm 4\pm 5$	
FMOW	for prompt muon neutrinos			4.0 ± 1.0		2.0 ± 0.5		$21\pm 3\pm 4$

TABLE 19. Summary of results from several recent fixed target experiments on the production of charmed particles by incident negative pions. When possible, the last column contains the $D\bar{D}$ production cross section values adjusted to reflect the assumptions employed in this thesis, including branching ratios, spin-weighting, and symmetry about x_F of zero. All results assume linear A dependence.

Experiment Ref.		π^- Beam Momentum (Gev/c)	Target Material	Production Model n	b	Reported Charm σ (μb)	$D\bar{D}$ Cross Section (μb)
E515	prompt μ trigger charged D^*	205	Be	3.0	1.1	$34\pm18^{+14}_{-9}$	$34\pm18^{+14}_{-9}$
E515 [100]	prompt μ trigger opposite sign μe	205	Be	Model III 5	2	18±6	10± 3
NA11 [51] ACCMOR	single e trigger Kπ and Kππ	175/200	Be	Model I 0.8±0.4	1.1±0.5	48±15±24	28± 9±14
NA11 [52] ACCMOR	single e trigger MSD Kπ Kππ Kπππ	200	Be	Model I 2.0±0.5	1.0±0.2	55± 9±25	29± 5±13
E567 [48] Fitch et al.	charged D^*	200	Be	Model II 3	1.1	4.2±1.4 charged D^*	8± 3
E595 [47] CCFRS	density extrapolation for prompt single muons	278	Fe	(24%) 0.9+0.9-0.6 (76%) 5.9+3.2-1.6	Model I 0.7±0.15	20± 4 $x_F>0$	30± 6
NA18 [53] BIBC	interaction trigger vertex detection	340	C_3F_8	$(1-\lvert x_F\rvert)^n \exp(-bp_T)/E$ 0.7+0.9-0.7	2.5	28±11	
NA16 [55] LEBC EHS	interaction trigger vertex detection	360	H	Model I 2.8±0.8	1.1±0.3	40+15-8 $x_F>0$ incl.	23^{+9}_{-5}

The charm search described in this document employs prompt muon triggered data recorded in a two arm spectrometer to study the associated production and decay of charmed states produced by 205 GeV/c π^- beryllium interactions. The $D\bar{D}$ cross sections determined from this data indicate that about 20 percent of the events in the final sample were from charmed sources. Thus, the prompt muon trigger coupled with the filtering analysis was effective in enhancing the charm content of the final data sample. However, the small acceptance of the trigger arm coupled with the inefficiencies and incomplete particle identification in the forward arm resulted in marginal sensitivity to individual charm decay modes. Model dependent upper limits on the total $D\bar{D}$ production cross section are determined from the $K\pi$ mass plots. For the production models presented, the 95 percent confidence upper limits on the $D\bar{D}$ production cross section are less than 48 μb per nucleon. Using the background suppression derived from the kinematics of the charged D^* decay into a neutral D and a charged pion, an enhancement of 30±16 combinations above background is observed in the $K\pi\pi$ final state. Interpreted as a charged D^* signal, this enhancement corresponds to a model dependent inclusive $D\bar{D}$ production cross section of $34\pm18^{+14}_{-9}$ μb per nucleon.

6.5 PROSPECTS

The data from this experiment are not decisive in the study of hadronic production of charm, and the prompt muon trigger, as implemented, was insufficient to isolate many charmed decays cleanly above background. One could imagine making a gain in sensitivity of a factor of 2 by improving the tracking efficiency, and a factor of 1.4 by employing a fast OR from the trigger arm PWC's in the trigger, thereby increasing the detector livetime by triggering only when a charged track is present in the trigger arm PWC's. Another factor of 1.5 could be gained by improving the beam system so that the interaction vertex could be isolated in nearly every event. An additional factor of 2 in running time would not be unreasonable. The background suppression that would be provided by additional particle identification would also be extremely useful. The use of a denser absorber in the initial stages of the trigger arm would be beneficial because it would further suppress muons from the decay of long lived hadrons. It would be reasonable to increase the size of the anti-wall to fully shadow all the trigger arm hodoscopes. The acceptance of the spectrometer was not phenomenal--particularly the trigger arm acceptance. But without restructuring the entire spectrometer, or abandoning the basic philosophy of the target and absorber geometry, an increase in the trigger arm acceptance could probably only be effectively achieved by decreasing the forward arm acceptance or resolution. The improvements described above might result in an order

of magnitude increase in the sensitivity of a prompt muon triggered charm search. Thus, although it is still conceivable that the techniques employed in this particular hadronic production charm search could be fruitfully employed, it seems unlikely that these techniques alone can effectively compete with the high resolution vertex detection techniques being developed and implemented in the next generation of studies of hadronic production of heavy flavors in fixed target experiments.

REFERENCES

[1] M. Gell-Mann, Physics Letters 8, 214 (1964).

[2] N. Cabibbo, Physical Review Letters 10, 531 (1963).

[3] M. Bourquin et al., Zeitschrift für Physik C21, 27 (1983).

[4] B. J. Bjørken and S. L. Glashow, Physics Letters 11, 255 (1964).

[5] S. Weinberg, Physical Review Letters 19, 1264 (1967).

[6] S. L. Glashow, J. Iliopoulos, and L. Maiani, Physical Review D2, 1285 (1970).

[7] F. J. Hasert et al., Physics Letters 46B, 138 (1973).

[8] Mary K. Gaillard, Benjamin W. Lee, and Jonathan L. Rosner, Reviews of Modern Physics 47, 277 (1975).

[9] Chris Quigg, Gauge Theories of the Strong, Weak, and Electromagnetic Interactions, (Bejanmin/Cummings, Reading, Mass. 1983).

[10] James D. Bjorken and Sidney D. Drell, Relativistic Quantum Mechanics, (McGraw-Hill Inc., 1964) pp. 261-264.

[11] G. Altarelli, N. Cabibbo, and L. Maiani, Nuclear Physics B88, 285, (1975).

[12] R. L. Kingsley et al., Physical Review D11, 1919 (1975).

[13] Kiyoshi Niu, Eiko Mikumo, and Yasuko Maeda, Progress of Theoretical Physics 46, 1644 (1971).

[14] T. Ferbel, in Experimental Meson Spectroscopy - 1974, edited by David A. Garelick (American Institute of Physics, 1974) pp. 393-395.

[15] J. J. Aubert et al., Physical Review Letters 33, 1404 (1974).

[16] J.-E. Augustin et al., Physical Review Letters 33, 1406 (1974).

[17] A. De Rújula and S. L. Glashow, Physical Review Letters 34, 46 (1975).

[18] E. G. Cazzoli et al., Physical Review Letters 34, 1125 (1975).

[19] G. Goldhaber et al., Physical Review Letters 37, 255 (1976).

[20] I. Peruzzi et al., Physical Review Letters 37, 569 (1976).

[21] J. G. Branson et al., Physical Review D20, 337 (1979).

[22] K. J. Anderson et al., Physical Review Letters 37, 799 (1976).

[23] Richard P. Feynman, Physical Review Letters 23, 1415 (1969).

[24] C. A. Heusch, "Heavy Flavor Production from Photons and Hadrons," in
Proceedings of Summer Institute on Particle Physics, edited by Anne Mosher, SLAC report No. 245, 195;
F. Halzen, "Production of Heavy Quarks," in
Proceedings of the XXI International Conference on High Energy Physics (Paris, 1982) Journal de Physique C3 381.

[25] D. Drijard et al., Physics Letters 81B, 250 (1979);
K. L. Giboni et al., Physics Letters 85B, 437 (1979);
W. Lockman et al., Physics Letters 85B, 443 (1979);
D. Drijard et al., Physics Letters 85B, 452 (1979);
J. Irion et al., Physics Letters 99B, 495 (1981);
M. Basile et al., Lettre al Nuovo Cimento 30, 487 (1981).

[26] George H. Trilling, Physics Reports 75, 57 (1981).

[27] R. M. Baltrusaitis et al., "A Direct Measurement Of Charmed D^+ and D^0 Semileptonic Branching Ratios," (Mark III Collaboration) SLAC-PUB-3532 (Dec 1984), submitted to Physical Review Letters.

[28] Nigel Lockyer, "Latest Results from the MARK II at PEP," in
Proceedings of the 11th SLAC Summer Institute, edited by Patricia M. McDonough, SLAC report No. 267, 689;
M. Piccolo, "Recent Results from MAC", in
Proceedings of the 11th SLAC Summer Institute, edited by Patricia M. McDonough, SLAC report No. 267, 673.

[29] W. Bacino et al., Physical Review Letters 43, 1073 (1979).

[30] J. J. Aubert et al., Nuclear Physics B213, 31 (1983).

[31] A. Bodek et al., Physics Letters 113B, 82 (1982).

[32] H. Yamamoto et al., Physical Review Letters 54, 522 (1985).

[33] S. Reucroft, "Charm Properties", in Proceedings of the 12th International Winter Meeting on Fundamental Physics (Santander, Spain, 1984).

[34] R. Brandelik et al., Physics Letters 70B, 132 (1977).

[35] A. Chen et al., Physical Review Letters 51, 634 (1983); M. Althoff et al., Physics Letters 136B, 130 (1984); H. Albrecht et al., Physics Letters 146B, 111 (1984).

[36] E. Vella et al., Physical Review Letters 48, 1515 (1983).

[37] C. Baltay et al., Physical Review Letters 42, 1721 (1979); B. Knapp et al., Physical Review Letters 37, 882 (1976).

[38] S. F. Biagi et al., Physics Letters 122B, 455 (1983).

[39] S. F. Biagi et al., Properties of the Charmed Strange A^+ and Evidence for the Charmed Doubly Strange Baryon T^0 at 2.74 GeV/c^2," CERN-EP/84-154, (Nov. 1984), submitted to Zeitschrift für Physik C.

[40] N. W. Reay, "Heavy Quark and Lepton Lifetimes" in Proceedings of the 1983 International Symposium on Lepton and Photon Interactions at High Energies, edited by David G. Cassels and David L. Kreinick (Cornell University, Ithaca, New York, 1983) pp. 244-274.

[41] L. Maiani, "Theoretical Ideas on Heavy Flavor Weak Decays," in Proceedings of the XXI International Conference on High Energy Physics (Paris, 1982) Journal de Physique C3 631; David Hitlin, "D Meson Decay Studies at the ψ''," CALT-68-1230 (California Institute of Technology, Calif., 1985).

[42] A. Kernan and G. VanDalen, Physics Reports 106, 297 (1984); Alois Putzer, "Production of Open Heavy Flavours in Hadronic Interactions" (Institut für Hochenergiephysik der Universität, Heidelberg, Germany, May 1983); C. M. Fisher, "New Experimental Results on the Hadroproduction and Photoproduction of Charmed Particles," in Proceedings of the XXI International Conference on High Energy Physics (Paris, 1982) Journal de Physique C3 146.

[43] R. C. Ball et al., Physical Review Letters 51, 743 (1983).

[44] M. E. Duffy et al., Physical Review Letters 52, 1865 (1984).

[45] Thomas Nash, "Recent Results on D Decays and Lepton, Photon, (and Hadron) Production of Charm," in Proceedings of the 1983 International Symposium on Lepton and Photon Interactions at High Energies, edited by David G. Cassels and David L. Kreinick (Cornell University, Ithaca, New York, 1983) pp. 329-375.

[46] J. L. Ritchie et al., Physics Letters 126B, 499 (1983).

[47] J. L. Ritchie et al., Physics Letters 138B, 213 (1984).

[48] V. L. Fitch et al., Physical Review Letters 46, 761 (1981).

[49] A. D. Montag, Ph.D. thesis, Princeton University, 1982.

[50] R. Bailey et al., Nuclear Physics B239, 15 (1984).

[51] R. Bailey et al., Physics Letters 132B, 230 (1983);
R. Bailey et al., Physics Letters 132B, 237 (1983).

[52] R. Bailey et al., "Measurement of D Meson Production in 200 GeV/c π^--Be Interactions," contributed to the XXII International Conference on High Energy Physics (Leipzig, 1984).

[53] A. Badertscher et al., Physics Letters 123B, 471 (1983).

[54] M. Aguilar-Benitez et al., Physics Letters 123B, 103 (1983).

[55] M. Aguilar-Benitez et al., Physics Letters 123B, 98 (1983);
M. Aguilar-Benitez et al., Physics Letters 135B, 237 (1984).

[56] M. Aguilar-Benitez et al., Physics Letters 146B, 266 (1984).

[57] N. Ushida et al., Proposal for Fermilab E653;
S. Reucroft et al., Proposal for Fermilab E743;
M. Church et al., Proposal for Fermilab E690.

[58] Makoto Kobayashi and Toshihide Maskawa, Progress of Theoretical Physics 49, 652 (1973).

[59] M. L. Perl et al., Physical Review Letters 35, 1489 (1975);
M. L. Perl et al., Physics Letters 63B, 466 (1976).

[60] S. W. Herb et al., Physical Review Letters 39, 252 (1977).

[61] S. Behrends et al., Physical Review Letters 50, 881 (1983).

[62] G. Arnison et al., Physics Letters 122B, 103 (1983).

[63] G. Arnison et al., Physics Letters 126B, 398 (1983).

[64] G. Arnison et al., Physics Letters 147B, 222 (1984).

[65] G. Arnison et al., Physics Letters 147B, 493 (1984); P. Darriulat, "Experimental Summary: Selected Highlights", invited talk presented at XXII International Conference on High Energy Physics (Leipzig, 1984) CERN-EP/84-118.

[66] James R. Sanford, "The Fermi National Accelerator Laboratory," Annual Review of Nuclear Science, Vol. 26, edited by Emilio Segre (Calif., 1976) pp. 151-198.

[67] Stan Eckland, "M1 User's Guide," Fermilab.

[68] W. F. Baker et al., Fermilab 78/79-EXP (1978).

[69] G. Coutrakon et al., "Identification of 200 GeV/c Particles Using a Ring-Imaging Cherenkov Detector", Fermilab Note FN-351, 1981.

[70] Particle Data Group, "Reviews of Particle Properties," Reviews of Modern Physics 56 (1984).

[71] A. S. Carroll et al., Physics Letters 80B, 319 (1979).

[72] Louis Costrell, "Standard Nuclear Instrument Modules," U. S. AEC report TID-20893 (rev. 4), July 1974.

[73] E. J. Barsotti et al., "CAMAC Tutorial Articles," U. S. ERDA report TID-26618, October 1976.

[74] Lucien Marcus Cremaldi, Ph.D. thesis, Northwestern University, 1983.

[75] R. Yamada et al., Nuclear Instruments and Methods 138, 567 (1976).

[76] G. Ginther et al., "40D48 Field Measurements For E515 Using the Fermilab Ziptrack System," 1983 (unpublished).

[77] D. R. Green, Nuclear Instruments and Methods 158, 249 (1979).

[78] W. Sakumoto et al., Nuclear Instruments and Methods in Physics Research A235, 61, (1985).

[79] PDP11 04/34/45/55/60 Processor Handbook, Digital Equipment Corporation, 1978.

[80] J. F. Bartlett et al., IEEE Transactions on Nuclear Science NS-26, 4427 (1979);
L. M. Taff et al., "Fermilab Multi User's Guide," Fermilab PN-97.5, October 1979;
E. K. Quigg et al., "Multi Programming Reference Notes," Fermilab PN-106, March 1980.

[81] Sam C. Bibler, "Getting Started with RT-11 at Fermilab," Fermilab PN-72, May 1977;
RT-11 System User's Guide, Digital Equipment Corporation DEC-11-ORGDA-A-D,DN1, 1978.

[82] "Jorway JY411 Parallel CAMAC Branch Driver," Fermilab HN-25.

[83] A. E. Brenner and R. G. Martin, "Bison Interrupt and Gate Control," Fermilab HN-3.1, 1977.

[84] R. Brun, I. Ivanchenko, and P. Palazzi, "HBOOK User's Guide," CERN Program Library Y250, 1979;
R. Brun and H. Watkins, "HPLOT User's Guide," CERN Program Library Y251, 1982;
F. James and M. Roos, "MINUITS," CERN Program Library D506, 1977.

[85] Stephen Bruce Sontz, Ph.D. thesis, Northwestern University, 1983.

[86] J. M. Bishop, "Momentum Determination in E515," 1980, (unpublished).

[87] Brice Carnahan, Applied Numerical Methods, (Wiley, New York, 1969), p. 361.

[88] C. Lechanoine, M. Martin, and H. Wind, Nuclear Instruments and Methods 69, 122 (1969).

[89] Richard R. Pemper, Ph.D. thesis, University of Notre Dame, 1983.

[90] Leonard Gordon Spiegel, Ph.D. thesis, Carnegie-Mellon University, 1984.

[91] Virgil L. Highland, Nuclear Instruments and Methods 129, 497 (1975).

[92] Bruno Rossi, High Energy Physics (Prentice-Hall, New York, 1952) pp. 66-73.

[93] Dennis Theriot, "Muon dE/dx and Range Tables: Preliminary Results for Shielding Materials", Fermilab TM-229 (1970).

[94] J. Michael McQuade, Ph.D. thesis, Carnegie-Mellon University, 1983.

[95] Willis Kazuo Sakumoto, Ph.D. thesis, Northwestern University, 1984.

[96] Rafe H. Schindler, "New Results on the Hadronic and Semileptonic Decays of Charmed D Mesons Measured in e^+e^- Collisions," MARK III collaboration, presented at XXII International Conference on High Energy Physics, (Leipzig, 1984) CALT-68-1161.

[97] Particle Data Group, "Errata for the 1984 Edition of the 'Reviews of Particle Properties'," 1984.

[98] R. Bailey et al., Zeitschrift für Physik C22, 125 (1984).

[99] J. Badier et al., Zeitschrift für Physik C20, 101 (1983).

[100] R. M. Edelstein et al., Physical Review Letters 53, 1411 (1984).